Study of a Thermo-Responsive Foam Using Interferometry on a Single Draining Bubble

by

Matthew Jackman

A thesis submitted in partial fulfillment of the requirements for the degree of

Master of Science

in

CHEMICAL ENGINEERING

Department of CHEMICAL AND MATERIALS ENGINEERING

University of Alberta

Abstract

Overly-stable froth in mineral flotation columns are sometimes a problem for separation operations. Greater quantities of fine particles in the input slurry can contribute to froth that is too stable and overruns the equipment capacity. Currently, the best ways to deal with this problem are to increase column launderer size, install deaeration tanks, and treat the froth with defoaming agents. These solutions can, however, be cost prohibitive for some operators.

Poly(n-isopropylacrylamide) (PNIPAM), a thermo-responsive polymer, has been investigated for use as a tunable frothing agent. A tunable frothing agent could allow operators to adjust the froth stability in-situ by applying an external stimulus.

In this work, PNIPAM was shown to stabilize tunable aqueous foam. Below its lower critical solution temperature, PNIPAM aqueous solution generates foam well, and foamability increases with increased concentration. Above the lower critical solution temperature, the foam becomes much less stable. Adsorption at the air-water interface, using common equilibrium, and dynamic surface tension measurements, found PNIPAM to be similarly surface active at high and low temperature. The same was found for the bubble interfaces from sparging nitrogen through PNIPAM solution in a column.

The drainage of PNIPAM-stabilized air-in-liquid-film bubbles were studied using a new interferometry technique developed here. The tunable foamability has been attributed to drastic change in thin-film drainage rate. At 40 °C, the drainage rate was measured to be more than two times greater compared to 20 °C.

To evaluate the drainage and rupture of the thin foam films, a new interferometry technique that uses three concentrically aligned light sources was developed. Image analysis code developed here takes-in a video of the lifetime of a single, well-controlled air-in-liquid-film bubble, and measures film thickness directly. The technique makes use of pattern recognition methods to align the interference patterns with the library of patterns of known film thicknesses. Unlike most popular methods, film thicknesses can be measured without achievement of a Newton black film, so it is possible to confidently assess draining films which rupture at thicknesses greater than a few hundred nanometers.

Preface

Part of the work in Chapter 3: has been published as Jackman, M., Xu, Z., Liu, Q., 2016. Tuning Foamability and Foam Stability Using Temperature-Responsive Poly(N-isopropylacrylamide), in: XXVIII International Mineral Processing Congress. I was responsible for data collection, analysis, and manuscript composition. Z. Xu contributed to manuscript edits. Q. Liu was the supervisory author, formed the initial concept, and contributed to manuscript edits.

Acknowledgements

I would like to thank Dr. Qingxia Liu and Dr. Zhenghe Xu for taking me on as a student, and giving me the tools, resources, and support to learn to develop as a researcher. I've gained much from all the members of both research groups - from their formal presentations, conversations, and camaraderie. I learned a lot, and enjoyed all of your company. I owe special thanks to my friends/mentors/colleagues Yuechao Tang and Zhenzhen Lu who were always very generous with their time to train me on the use of new equipment, troubleshoot problems in my research, or teach me about Chinese culture and food.

Many thanks to my friend, Carl Corbett, who gave me more computing power; supported our lab safety committee; and assembled, disassembled, reassembled, and fixed all of our lab equipment. Most of all, I benefitted greatly from Carl's company and conversation over coffee.

Thanks to Adrien Bussonnière for his guidance through the last year of difficult work. He guided me into and out of the abyss of computer code writing and revising (and revising, and revising…), helped me set intermediate goals, and helped me to simplify many of the overwhelming research problems that had paralyzed me. Discussions in the lab or over coffee always left me invigorated and excited to work and learn.

Finally, the biggest of thanks go to my wife, Alex. From her, I have learned to set lofty goals, and put in the daily work to achieve them. Her support has been the keystone to my achievement.

Table of Contents

List of Tables

List of Figures

Acronyms

LCST	lower critical solution temperature
PNIPAM	poly(n-isopropylacrylamide)
SDS	sodium dodecyl sulfate

Chapter 1: Introduction

In 2015, the mining industry (excluding oil and gas) accounted for 25.7B dollars[1] of the total Canadian GDP (1.67T dollars), or 1.5% ("Real gross domestic product, expenditure-based, by province and territory," 2016). Some vital products are made from the raw materials mined in Canada, such as: batteries, electrical circuitry, computer screens, vehicles, and tires (Marshall, 2015). Research and innovation in the mineral processing industry is as important as ever as government policy prioritizes sustainable practices, including: enhancing mine productivity, managing water in the mining cycle, minimizing and managing mine waste, and increasing energy efficiency in mining ("Green Mining Initiative," 2016).

Mineral processing is the over-arching term for many types of processes, techniques, and process flows. The purpose is to separate the valuable minerals from waste gangue, and the basic unit operations to do so are as follows (Fuerstenau and Han, 2009):

1. Size reduction of raw mineral ore.
2. Size separation, or classification. The efficacy of different down-stream processes can be size-sensitive, and so different size or particles may require additional processing in a parallel stream before rejoining the main process flow.
3. Concentration. Particles are separated based on physicochemical properties, such as surface attributes (in froth flotation), density (in gravity concentration), and magnetic/electrical properties (in magnetic and electrostatic concentration).
4. Dewatering. Many preceding separation processes require water, which must be later separated from the mineral.
5. Aqueous dissolution. Leaching is a process where metals are dissolved in water for separation from the gangue, so this processes induces precipitation of those metals for recovery.

[1] Values represent chained (2007) dollars.

In mineral processing, a balance must be struck between maximizing percent recovery (amount of mineral at output of the system compared to amount in the input ore), and meeting a minimum grade (the purity of the output ore) (Fuerstenau and Han, 2009). With this dilemma, it is obvious that there is always opportunity to improve both facets through innovation, which reduces wasted natural resources, and/or energy intensity of processing.

1.1 Column Flotation and Froth

Froth flotation is a mineral separation process whereby the crushed mineral ore is mixed with water, and air bubbles are used to carry the desired mineral upwards and away from the gangue in a column or cell. The air bubbles and mineral will form a froth zone at the top of a cell, and the gangue will form a sludge at the bottom. There are many variations of flotation machines, but the two basic types are flotation cells and flotation columns.

The major difference between flotation columns and flotation cells is the use of an impeller at the bottom of cells to create a turbulent zone for bubble size reduction and to induce bubble-particle collision. Flotation columns are typically taller and more narrow, ranging from 9 to 14 meters in height and less than 2 meters in diameter. The operation of a typical flotation column is illustrated in Figure 1-1.

The ore/water slurry is pumped into a point about two-thirds up the height of the column, and air bubbles are produced by a sparger at the bottom of the column. The air bubbles travel upward, attach to mineral particles and continue onward to the top of the column to join the froth. Froth flows over the top edge of the column, and is collected in the launderer. Unwanted gangue particles flow out the bottom to tailings. The froth height is typically 0.5 to 2 meters high in a column, and a wash water shower is used to inhibit froth growing beyond the desired height, as well as to promote drainage through the network of water channels. The forced drainage is important, as it aids in flushing entrained hydrophilic particles back down to the collection zone, rather than reporting to the launderer with the mineral (Fuerstenau and Somasundaran, 2009).

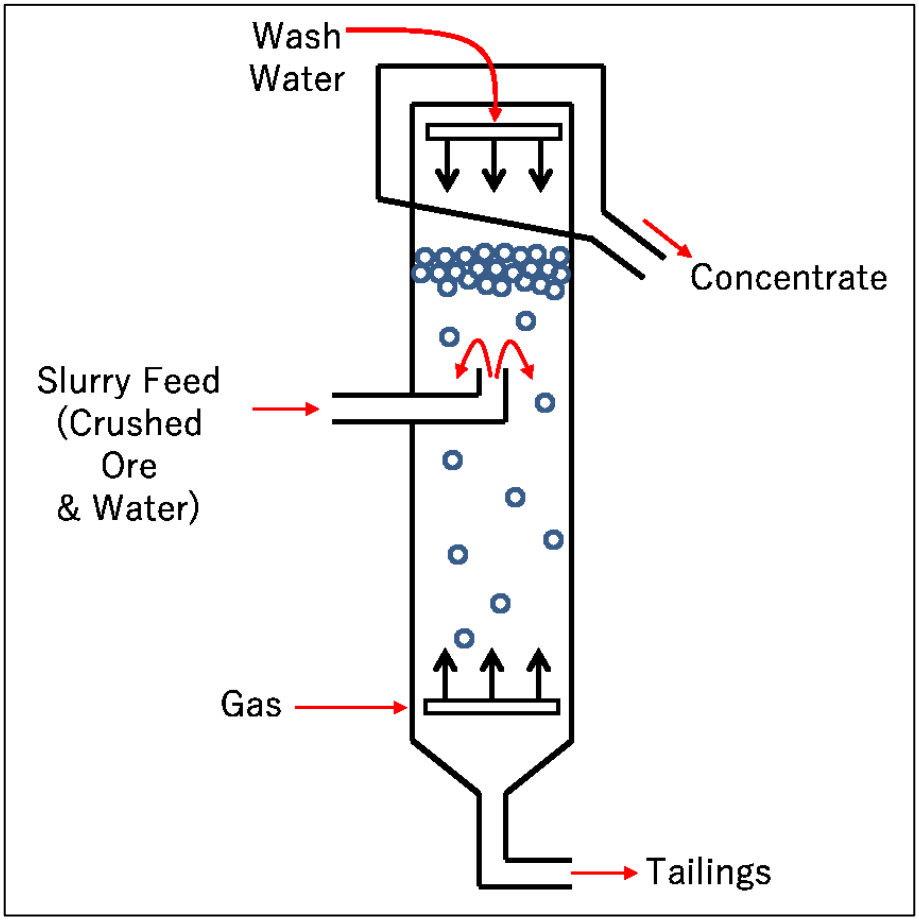

Figure 1-1: Operation of a typical flotation column, after Finch and Dobby,(1990).

Collision success is reliant on the relative size of bubbles and particles, as well as the approach velocities. Attachment success after collision is reliant on the hydrophobicity of the mineral and gangue particles. Particles with a greater hydrophobicity will attach more readily to a rising bubble. Several reagents may be added to the slurry in order to alter the surface properties of desired minerals to increase probability of attachment, and alter the surface properties of the gangue to inhibit attachment (Fuerstenau and Somasundaran, 2009), such as :

1. Collectors: A surfactant that adsorbs selectively on the desired mineral, and imparts hydrophobicity to promote attachment to bubbles.

2. Frothers: A surfactant which stabilizes the froth to promote drainage of entrained particles, and reduces bubble size in the collection zone by adsorption at the air-water interface.
3. Activators: A reagent to activate adsorption of collectors (i.e. oleate cannot adsorb to quartz without calcium ions (Ca^{2+}) at an elevated pH.
4. Depressants: A reagent often used to separate two minerals that would be floated together. The depressant adsorbs to the mineral surface, inhibiting the adsorption of collectors, and then masking the hydrophobic domains of collector that did adsorb so that the mineral will not be floated.
5. Deactivators: Combines with an activator to make a selected mineral surface neutral, so collector will not adsorb and the mineral will not be floated.
6. Dispersants: Chemical added to disperse slime coating of fine particles which mask the true surface properties of the mineral.
7. Flocculants: Polymers that selectively attach to fine mineral particles too small to effectively attach to bubbles. Larger flocs are created which can attach to a bubble and be floated.

In addition to the above reagents, the system pH must also be tightly controlled as it can have a great effect on the surface properties of the system constituents.

1.2 Purpose and Objectives

As stated in Section 1.1, frothers are one of many reagents that may be added to a flotation system to increase efficacy and efficiency of the process. The specific problem addressed here is the case of an overly-stable froth. Ideally, froth height is optimized by the addition of a calculated concentration of frother. Fine particles within the ore slurry, however, can also contribute to stabilizing froth – depending on shape, size, concentration, and hydrophobicity (Horozov, 2008). Fine particles may be so effective that surfactant-absent foams have been generated which are stabilized by micron-scale particles alone (Alargova et al., 2004). Flotation experiments with varied milling times have also shown a strong relationship between particle size and froth stability (Aktas et al., 2008), and froths with long lifetimes can cause problems in the down-stream

processes (Bethell et al., 2012). Common practices are to reduce frother dosages, or select weaker frothers, but the result is often unacceptable recovery (Bethell and Luttrell, 2005). The remaining option is to install larger launderers, store the collected froth in deaeration tanks, and treat it with defoaming agents, which requires both a large capital expense, and plant floor-space for the additional equipment. The objective of this work is to:

1. Evaluate PNIPAM as a tunable foam stabilizing agent.
2. Develop a technique for the study of a simple liquid film drainage system that mimics the drainage of a foam.
3. Elucidate the mechanism(s) by which PNIPAM stabilizes and destabilizes foam, so that tunable frothers may be effectively designed in future work.

There have been some interesting work to use PNIPAM as a responsive collector and flocculant in mineral processing (Burdukova et al., 2010; Franks et al., 2009), but none so far to suggest its use as a froth controller.

Chapter 2: Literature Review

2.1 Foam and Foam Properties

Foam is a system of gas pockets contained by liquid films. The thin liquid films make the walls, and three walls connect at 120° angles to form the Plateau borders. The Plateau borders have negative radii of curvature, by geometrical necessity to connect three lamellae. Capillary pressure of the Plateau borders, due to the negative radii of curvature, withdraws liquid from the films. In a force field, such as the gravitational field of Earth, the liquid drains through the Plateau borders in the direction of the field. Plateau borders meet in groups of four at a vertex to form the interconnected liquid network making the continuous phase of foam (Koehler et al., 2000).

Surfactants are molecules with an affinity for the interface of two immiscible phases. For foam, the phases are gas and liquid, and more specifically, air and water. The presence of surfactant at the air-water interface lowers interfacial energy between the two phases, and increases thermodynamic stability. It is by the presence of surfactants that a

foam can be metastable – meaning it does not collapse immediately, but it will collapse over a period of time.

The methods for generating and evaluating foam are many and varied. Generation methods include: bubbles blown from a sparger into stationary liquid; co-injection of liquid and gas; gas entrained from disrupted free surfaces, as in a plunging jet, the Bartsch test where a vial of gas and liquid is shaken; and phase transitions, as in boiling or cavitation (Drenckhan and Saint-Jalmes, 2015). Generally, foam is studied in free drainage, where gravity and capillary suction pull the liquid down through the foam, while the intervening lamellae become thinner and thinner. Foam may also be studied in forced drainage, where liquid is fed into the top of a foam column at a rate that matches foam production, or in pulsed drainage where a small controlled volume of liquid is periodically injected at the top of the foam. Fluorescent or dyed liquid is often used to trace the path and speed of forced and pulsed drainage studies (Koehler et al., 2000).

There are two central mechanisms which determine foam lifetime (stability) (Langevin, 2002):

1. Coarsening (ripening, disproportionation)
2. Coalescence (film rupture)

These are reviewed in the following two sections.

2.1.1 Coarsening

Coarsening is the disappearance of some bubbles by shrinking due to gas diffusion across the thin film to larger bubbles that grow. Overall, the mean bubble diameter will increase and total number of bubbles will decrease. Diffusion of gas molecules through the liquid films from one bubble to another is driven by the difference in pressure between the neighbouring bubbles. Since smaller bubbles have a higher pressure, from the Laplace Equation (Equation 2-1), where ΔP represents the pressure difference across the interface of one bubble and the bulk liquid, γ is the surface tension, and R_1 and R_2 are the principal radii of the interface. The smaller of two adjacent bubbles will shrink, and the larger will grow as gas is driven from the higher to lower pressure bubble (Saint-

Jalmes, 2006). This process is more rapid for gasses with greater solubility, such as carbon dioxide compared to nitrogen (1.44 g/kg and 0.0173 g/kg at 25 °C, respectively (Yaws, 2003)).

$$\Delta P = \gamma \left(\frac{1}{R_1} + \frac{1}{R_2} \right)$$

(Equation 2-1)

In 1887, Lord Kelvin, using the equilibrium rules of Plateau, proposed that the shape of foam bubbles for optimal packing in an ordered structure would be a tetrakaidekahedron – a fourteen-sided polyhedron (Weaire and Hutzler, 2001). Since then, no other single polyhedron has been found to give a lower surface energy per foam cell, but others have calculated more favourable arrangements with a combination of two types of cells, of twelve and fourteen sides (Weaire et al., 1994). The ideal Kelvin or Weaire-Phelan shapes are rarely encountered in even tightly-controlled experiments (Weaire and Hutzler, 2001). Nevertheless, study of ordered foam involves cells of approximately 12 to 14 sides, and the diffusion is more complicated than that of a single pair of bubbles. Because 3-dimensional foam is more difficult to model, two-dimensional foam is often studied and modeled. For studies on pure coarsening, a "dry-foam" is usually required, which is one with a low liquid fraction, where further drainage of the lamellae has been equilibrated by the disjoining pressures. Foam coarsening is analogous to grain growth in metals, that two-dimensional foams of low liquid fraction can be described by Von Neumann's law for grain growth (Magrabi et al., 1999). Von Neumann's law can be used to predict the coarsening of each bubble-cell by calculating the temporal change in area of the 2D bubble.

$$\frac{dA_m}{dt} = \frac{2\pi}{3} \gamma \kappa (n - 6)$$

(Equation 2-2)

Where,

- A_m is the projected area of one cell in the 2D foam

- γ is surface tension (but in the 2D case, is really a line tension)
- κ is the permeability of the liquid film
- n is the number of sides to the bubble

It appears counterintuitive that the pressure difference is not included in this equation, but one can derive (Equation 2-2) by substituting the law of Laplace (Equation 2-1) and two-dimensional curvature sum rule (Equation 2-3) into (Equation 2-4) which calculates the change in area by the sum of pressure differences at each interface:

$$\sum_i \frac{l_i}{r_i} = 2\pi\left(1 - \frac{n}{6}\right)$$

(Equation 2-3)

$$\frac{dA_m}{dt} = -\kappa \sum_i (p_m - p_i) l_i$$

(Equation 2-4)

Where,

- l_i is the length of film between cell m and each neighbor cell i
- r_i is the radius of curvature of film i
- p_m is the pressure in cell m
- p_i is the pressure in neighbouring cell i

(Equation 2-4 clearly demonstrates that the bubble coarsening is driven by the pressure difference between cells, and regulated by the permeability of the gas phase through the liquid phase.

2.1.2 Coalescence

Coalescence is governed by the process of liquid draining from the lamellae to the Plateau borders, until a critical thickness is reached and rupture occurs. The capillary pressure of the Plateau borders draws the liquid from the lamellae, and gravity draws the liquid down through the network of Plateau borders. In a gravitational field, foam is

considered metastable as the liquid drains along the direction of the field. The liquid lamellae continue to thin, until reaching a critical rupture thickness and two air cells coalesce. The liquid viscosity, density, and surface rheology, imparted by a surfactant slow the drainage process, contributing to the foam stability. Foam formed in microgravity without surfactant, and of high liquid fraction with spherical cells can be stable, but foams containing polyhedral cells are still very unstable, likely due to the capillary suction of Plateau borders with smaller radii of curvature than those of the lamellae (Caps et al., 2014).

Foam is often simplified to a single film, bubble, or hemisphere for the detailed study of thin-film drainage. The most popular option is the Thin-Film Pressure Balance (Scheludko, 1967), where a liquid film is produced in the annulus of a porous ring, and the film pressure is controlled by an attached capillary. Other techniques include an atomic force microscope used to approach a bubble to a solid surface in water (Shi et al., 2015); The Platikanov cell, where a capillary tube, immersed in the intervening liquid, is placed orthogonally to a surface, and an air bubble is forced from the capillary to create a film on the solid surface (Nedyalkov et al., 2007), or orientated upward to create a film with the free surface (Frostad et al., 2016); A rising hemispherical dome meeting the free liquid surface to create a draining film (Bhamla et al., 2014); two droplets approaching, immersed in an immiscible liquid (Chan et al., 2011); gravitational drainage of a single vertical film, drawn-up from a reservoir (Saulnier et al., 2014); gravitational drainage of a hemispherical air bubble, in open atmosphere, sitting at the top of an open liquid reservoir (Sett et al., 2013); and a bubble rising from the bottom of a liquid reservoir, contacting the free surface (Lhuissier and Villermaux, 2012).

2.2 Properties of Thin Films and Interfaces

2.2.1 Surface Tension and Marangoni Effect

Surface tension (or interfacial energy) represents the energy required to increase an interface of two phases by a unit-area. At the molecular level, it is described as the energy to bring a molecule out from its bulk, where it interacts on all sides with like-molecules,

to the surface where it will only be partially surrounded by like molecules with which to interact, and partially by dissimilar molecules or vacuum (Butt et al., 2003).

Where a surface tension gradient is created, an interesting happening will occur – the Marangoni effect. A surface tension gradient will drive the liquid from the low to high surface tension area to equilibrate. This is the cause of "wine tears", where the liquid is driven up the side of its glass until enough has accumulated, and it rolls back down under the force of gravity. The drive upward is caused by a surface tension gradient created when ethanol evaporates from the glass wall due to its vapor pressure lower than that of water. More liquid is driven upward, more ethanol evaporates, and the surface tension gradient still exists (Butt et al., 2003).

2.2.2 Rate of Adsorption

The surface tension of a newly-formed interface will be similar to a solvent without surfactant. In time, surfactant will (1) diffuse from the bulk to the subsurface, and then (2) adsorb at the interface (Eastoe and Dalton, 2000). As surface concentration increases, the surface tension will decrease until the equilibrium surface concentration value is reached. The first mechanism, diffusion from bulk to subsurface, is controlled by Fick's diffusion equation. The second mechanism must consider the surface concentration, and the probability of a surfactant molecule at the subsurface meeting an unoccupied spot at the surface. The Ward and Tordai equation accounts for the resulting back-diffusion from subsurface to bulk (Eastoe and Dalton, 2000).

Rate of adsorption is an important parameter to consider along with equilibrium surface tension when evaluating a surfactant for use in a temporal-based system. If time for adsorption is much greater than the residence time of an interface, such as bubbles in a flotation column, then the surfactant will be less effective than intended.

2.2.3 Surface Rheology

Surface rheology is described by the complex surface shear modulus, G* (Equation 2-5), and the complex surface dilatational modulus, E* (Equation 2-6). For both moduli, the real component. represents the storage of elastic energy from imposed stresses, and the imaginary component represents the viscous dissipation of energy.

$$G^* = G' + iG''$$

(Equation 2-5)

$$E^* = E' + iE''$$

(Equation 2-6)

Dilatational surface elasticity is defined as the ratio of change in surface tension relative to an increase in surface area (Wang et al., 2016), or the energy stored from an imposed dilatational deformation. Dilatational surface elasticity and viscosity are measured by the response from the interfacial surfactant molecules when a periodic dilation of the interface is induced (stress applied in the plane of the local interface). Two common methods to do this are the oscillating drop method (Guillermic, 2011) and the Langmuir Trough with oscillating barriers (Noskov et al., 2004; Yokoi and Kawaguchi, 2014).

Surface shear elasticity and viscosity may be measured using the oscillating needle of the interfacial stress rheometer (Brooks et al., 1999), a frequency-based classical rheometer (Guillermic and Saint-Jalmes, 2013), or by double-wall ring method (Vandebril et al., 2010).

The dilatational and shear moduli are related to Young's Modulus by (Equation 2-7). Sagis (2011) notes that it is actually the Young's Modulus which is measured in the Langmuir Trough experiments, but because $G_s << E_d$ typically, the measurement is taken directly as the dilatational modulus.

$$Y_s = E_d + G_s$$

(Equation 2-7)

Dilatational and shear viscoelasticities have an effect on foam stability, but the extent to which is still foggy (Wang et al., 2016). Furthermore, Langevin (2014) has shown that shear rheological measurements are contradictory, and that is due to the lack of understanding of the properties being examined. More needs to be uncovered about the nature of viscoelasticities before their roles in foam stability can be fully understood.

2.2.4 Marginal Regeneration

Marginal regeneration can be a nuisance in measuring thin films. Marginal regeneration occurs where there is an inversion of the capillarity at a Plateau border. An example is a film generated in a thin wire loop. The point where the liquid meets the wire, and wets it will have a negative radius of curvature, which indicates a negative Laplace pressure. Liquid is then drawn from the rest of the film toward the Plateau border, thinning a local region, become less dense, and more buoyant. The buoyant region may detach and float upward through the film until it equilibrates (Couder et al., 1989). When measuring film thickness by interferometry, marginal regeneration plumes must be removed or avoided in the image analysis step to avoid contaminating data.

2.3 Thermo-Responsive Polymer, PNIPAM

Poly(N-isopropylacrylamide) (PNIPAM) is a macromolecule made of a chain of the NIPAM (or NIPAAM) monomer. PNIPAM is the most popular of a unique class of polymers, called thermo-responsive polymers, with the characteristic of changing conformation in response to a change of solvent temperature. For PNIPAM, this so-called Lower Critical Solution Temperature (LCST), also known as the cloud point, is between thirty and thirty-five degrees Celsius (Schild, 1992). A common mischaracterisation of this change is that of a hydrophilic-to-hydrophobic transition (Pelton, 2010). The specific change is in the way the molecule interacts with the solvent due to the preference in hydrogen-bonding. In water, at temperatures below the LCST, the amide groups of PNIPAM will preferentially hydrogen-bond with surrounding water molecules – the case

often referred to as hydrophilic. At temperatures above the LCST, the PNIPAM molecule curls in on itself so that the isopropyl groups can make contact with other hydrophobic parts of the molecule, and the amide groups will hydrogen-bonds intramolecularly with the other amide groups (Ahmed et al., 2009; Ramon et al., 2001). Because in this case the PNIPAM molecule interacts less with the surrounding water molecules, it is known as the hydrophobic condition. Pelton (2010) has made the point that "PNIPAM is never hydrophobic", because the molecule always contains hydrophilic and hydrophobic domains, but only changes its conformation and interaction with its solvent based on the environmental conditions. To avoid perpetuating use of this perhaps misleading characterisation, within this manuscript, the phases will be referred to as "coil" and "globule" conformations. The coil conformation occurs below the LCST, where the PNIPAM molecule stretches-out and interacts with surrounding water molecules, and the globule conformation occurs above LCST, where the molecule curls back inward on itself, intramolecularly bonding. The two conformations are illustrated in Figure 2-1.

The somewhat ordered water molecules surrounding the PNIPAM induce its conformation. Below the LCST, when the amide groups hydrogen-bond preferentially with water molecules, it is due to the relatively low contribution of the entropy term (ΔS) in the Gibbs free energy equation (Equation 2-8). Here, the enthalpy (ΔH) of the hydrogen bonds dominate. At sufficiently great temperatures, denoted by the LCST, the entropy term dominates, and hydrogen bonds with water molecules are sacrificed to reduce the imposition of ordering water molecules around hydrophobic domains of the PNIPAM molecule (Schild, 1992).

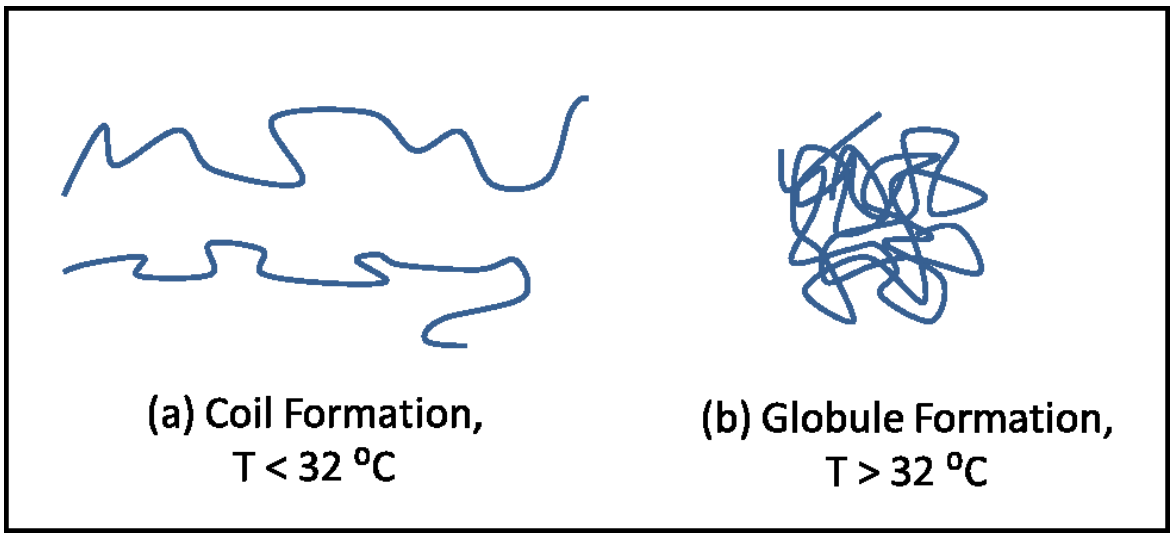

Figure 2-1: Illustration of the coil-to-globule transition of the PNIPAM molecule. The stretched-out coil formation occurs below LCST, where the amide groups hydrogen bond preferentially with the solvent water molecules (a). The curled-in globule formation occurs above LCST where amide groups hydrogen-bond intramolecularly.

$$\Delta G = \Delta H - T\Delta S$$

(Equation 2-8)

PNIPAM is surface-active, in that the molecule shows an affinity for the air-water interface, most easily measured by a reduction in surface tension. As temperature increases above the LCST, the PNIPAM molecule has even greater affinity for the interface, as measured by a decrease in surface tension (Gilcreest et al., 2006; Guillermic, 2011; Lee et al., 1999) and increased mass of adsorbed layer, as measured by neutron reflectivity (Lee et al., 1999).

Guillermic and Saint-Jalmes (2013) conducted a detailed study to evaluate PNIPAM for the purpose of generating thermo-responsive aqueous foams. They concluded: "…the foam stability remains poor and it is impossible to detect significant variations with temperature." PNIPAM was studied as a stabilizer of thermo-responsive foam in five facets:

1. Effect of temperature on surface tension
2. Effect of temperature on surface dilatational rheology

3. Effect of temperature on surface shear rheology
4. Bulk viscosity
5. Foam stability

These are detailed in the following five sections.

2.3.1 Surface Tension

Surface tension measurements were taken continuously of a PNIPAM solution using an optical tensiometer. As temperature increased, surface tension decreased from 44.5 mJ/m^2 until T = 34 °C where surface tension reached a plateau around 37.5 mJ/m^2. A key note is that the process was fully reversible as surface tension increased again when the temperature decreased – indicating the ability of PNIPAM to move to and from the surface as conditions change. Lee et al. (1999) performed surface tension measurement using the Wilhelmy plate method, and achieved similar results of decreasing surface tension with increasing temperature, including a plateau at approximately 37.5 mJ/m^2, which occurred at a temperature of 34 °C.

Gilcreest et al. (2006) studied the dynamic surface tension of PNIPAM at the air-water interface using the pendant drop and pendant bubble methods with optical tensiometer in the manner of Myrvold and Hansen (1998). They found:

1. The rate of adsorption is dependant on both the molecular weight of PNIPAM and the bulk concentration. Lower molecular weight and higher concentrations were associated with more rapid adsorption
2. A relationship between surface tension and adsorption density was obtained experimentally
3. This relationship, inserted into the Ward and Tordai equation allowed for prediction of surface tension as a function of bulk concentration and molecular weight.

2.3.2 Surface Dilatational Rheology

Using the oscillating pendant drop method with optical tensiometer, the same temperature ramp was applied as with equilibrium surface tension measurements. The dilatational modulus was dominant over the viscous (frequency-dependent) portion, so E* ~ E'. The dilatational modulus was immeasurably low below temperatures of 34 °C, and then increased rapidly to values indicating a highly elastic interface compared to the literature.

Yokoi and Kawaguchi (2014) found little change with temperature, but unfortunately only measured within the range of 5-35 ºC, which is just 3 °C above LCST and 1 °C the point at which others observe a transition. Noskov et. al. did not vary temperature, but did comment that "Although the surface activity of PNIPAM is significantly higher than that of other nonionic homopolymers studied so far, the main features of the surface viscoelastic behavior are similar." Those measurements were however taken at room temperature (below LCST).

2.3.3 Surface Shear Rheology

Measurements taken using a biconical rheometer with amplitude sweeps. Similar to the dilatational modulus results, there is a near-zero-measurement below the critical temperature at 33.5 °C. Above the critical temperature, there is a great increase in both the elastic and viscous portion of the modulus – both tracking closely until 39 °C, above which, the elastic term becomes slightly more dominant.

The surface shear modulus has also been measured using the Interfacial Stress Rheometer by Monteux et al. (2006). It was also found in this work that both G' and G" encounter a rapid change at a temperature of 34 °C, and that the G' term dominates the G". The change is described as a transition from a viscous to elastic interface (Monteux et al., 2006), or "solid to fluid" (Guillermic, 2011). Monteux et al. (2006) observed a surface layer that was dense and elastic above LCST which one could confirm by "drawing a thick membrane vertically from the surface using a needle." This was not observed at temperatures below LCST.

2.3.4 Bulk Viscosity

Measurements were taken using a rheometer with a double-gap Couette geometry. Viscosity was found to be largely independent of temperature with a value of 1.2 mPa·s, except a peak of 1.7 mPa·s at temperature of 34 °C. Monteux et al. (2006) also measured the viscosity to be largely unchanged by temperature, except a peak of 6 mPa·s occurring at a temperature of 30 °C. The difference in peaks may be explained by a difference in molecular weight, which differs by as much as an order of magnitude for these studies, and by difference in solution concentration.

2.3.5 Foaming

Foam was produced in a glass column with sparger. Liquid fraction was measured at different heights, but otherwise, the description of foam by (Guillermic and Saint-Jalmes, 2013) is largely qualitative here. The foams are relatively dry, collapse rapidly with large holes forming due to drainage and coalescence. The authors state "…the foam stability remains poor and it is impossible to detect significant variations with temperature." The authors comment that the poor foam stability is surprising, given the successful tuning of PNIPAM film thicknesses in a thin-film pressure balance by Jean et al. (2009). Jean et al. (2009) found very large stable film thicknesses of 110 nm at 24.5 °C and 150 nm at 27 °C with PNIPAM molecular weights of 190 000 g/mol and 90 000 g/mol. They attributed the stability to steric repulsion of long polymer chains dangling in the bulk. They also found the stable thickness increased with temperature – which was attributed to increased adsorption density measured by Lee et al. (1999), using neutron reflectivity.

This study by Guillermic and Saint-Jalmes (2013) has been the only study so far to attempt a thermo-responsive foam using PNIPAM, as Fameau et al., (2015) has also stated in their review of responsive aqueous foams. While the authors selected a polymer sample of low molecular weight, so that it may move easily like a surfactant, it was still 25000 g/mol, or approximately 87 times the size of the popular surfactant sodium dodecyl sulfate (SDS).

Chapter 3: Thermo-Responsive Frother

3.1 Introduction

Frothers serve three important purposes in mineral flotation (Finch and Tan, 2016):

1. To reduce bubble size – increasing total surface area of the system for bubble-particle attachment;
2. To reduce bubble rise velocity – increasing probability of attachment and decreasing probability of detachment; and
3. To enhance froth stability – enhancing secondary cleaning by allowing the entrained gangue particles to flow down the Plateau border channels, instead of reporting to the launderer.

In this section of study, PNIPAM was tested as a tunable frothing agent in mineral flotation columns. Firstly, it is shown that the stability of a PNIPAM foam can be tuned by changing the environmental temperature about the LCST. Secondly, it will be shown that the PNIPAM molecule maintains an affinity for the air-water interface at temperatures both above and below the LCST – causing a reduced bubble size in a sparger column, which also reduces the bubble rise velocity by way of increased surface area to volume ratio (drag forces become more dominant relative to buoyancy forces in (Equation 3-3)) as bubble size reduces.

$$F_b = \frac{4}{3}\pi(\rho_l - \rho_g)R_{bubble}^3$$

(Equation 3-1)

Where,

- F_b is the buoyancy force
- ρ_l is the density of surrounding liquid
- ρ_g is the density of gas bubble

- R_{bubble} is the radius of the gas bubble

$$F_d = 6\pi\mu R_{bubble}\vec{v}_t$$

(Equation 3-2)

Where,

- F_d is the drag force acting on the bubble
- μ is the liquid viscosity
- $\vec{v}_t$ is the terminal velocity of a rising bubble

$$\vec{v}_t = \frac{4(\rho_l - \rho_g)R_{bubble}^2}{18\mu}$$

(Equation 3-3)

The aim here is that a combination of these traits will make for a frothing agent where froth stability (purpose 3) may be tuned depending on the given circumstances of the particular slurry input, while the bubble size reduction (purpose 1) and bubble rise velocity reduction (purpose 2) may remain similarly effective – independently of this tuning.

3.2 Materials & Methods

In these experiments, PNIPAM, with carboxylic termination, LCST of 32 °C, and molecular weight of 7000 Da (product number 724866); and sodium dodecyl sulfate (SDS) were procured from Sigma-Aldrich to prepare test solutions. Water for test solutions was filtered through an EMD Millipore Milli-Q water purification system with Millipak 0. 22 μm filter and product resistivity of 18. 2 MΩ·cm.

3.2.1 Foamability and Foam Stability

To evaluate foamability, a glass column (50 mm x 50 mm cross-section) with a circular, 30 mm diameter sintered-glass sparger (pore size if 70 – 100 μm) was built. Before every trial, the column was rinsed thoroughly with deionized water, and no cleaning agents were used – to avoid the risk of depositing surfactant on the walls of the column. After rinsing, the column was filled with deionized water, and gas was bubbled through the sparger for two minutes to confirm the absence of surfactant. The column was then emptied, and a final rinse was applied with milli-Q water. A schematic of the apparatus is shown in Figure 3-1. Foam height was measured after flowing nitrogen gas through the sparger for 90 s at a rate of 0.5 L/min (superficial velocity of 1. 34 cm/s). Superficial velocity is defined in (Equation 3-4) by $\vec{v}_{super}$, where Q is the gas volumetric flow rate and A_c is the column cross-sectional area. After 90 s, the gas was shut-off, and foam height was measured. The liquid volume in each experiment was 100 mL.

$$\vec{v}_{super} = \frac{\mathrm{Q}}{A_c}$$

(Equation 3-4)

The column temperature was maintained by a recirculating heated bath. The bath was connected to polyethylene tubing which was wrapped around the base of the column, from the bottom to a point 3 cm below the top of the liquid level. Temperature of the liquid was measured manually by thermometer to a tolerance of ± 0.5 °C.

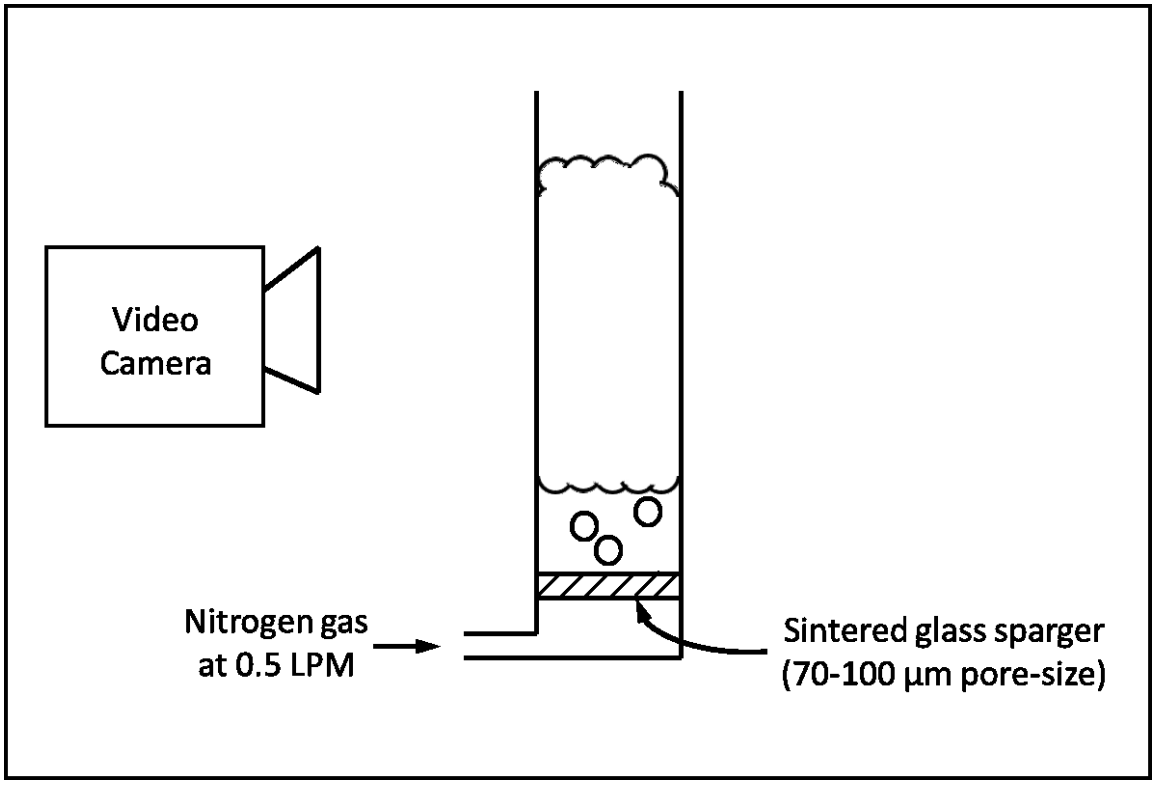

Figure 3-1: Experimental setup for measurement of foam height. A camera captures the entire foam volume, and the height is extracted from video.

For study of foam stability in a dynamic system, and to simulate the effects of in-situ temperature that might be implemented in a flotation column, the same foam volume apparatus shown in Figure 3-1 was used. In this case, after 90 seconds of gas sparging through 100 mL of 20 °C PNIPAM solution, a 100 mL shower was administered while the flow of nitrogen through the sparger continued. 100 mL of milli-Q water was used for the shower. Foam height recorded by video for continuous measurement throughout and after application of the shower. The 100mL wash-water was heated to 50 °C to observe the reaction of a continuously operating system to a change in temperature – simulating the change that would be seen in an active flotation column. The same was done with a 20 °C shower to compare the volume of foam destroyed by physical disruption due only to the falling water droplets, and not the altered temperature.

3.2.2 Swarm Bubble Size Reduction

Bubble coalescence was measured using a laser intensity apparatus similar to that used by Craig, Ninham, & Pashley (1993), and illustrated in Figure 3-2. Scattering of incident laser signal can be used to infer a change in mean bubble size. When gas flowrate is kept constant in the column, a reduction in bubble size will result in more light scattered from the incident path due to greater angle of incidence (and so angle of refraction), as shown in Figure 3-3 and an increased number of bubbles travelling across the beam path.

Seventy milliliters of solution were poured into the column of 26 mm inside diameter, and nitrogen gas was introduced at the bottom of the column through a sparger of 70-100 μm pore-size from Ace Glass at a rate of 0. 2 L/min (superficial velocity of 0. 63 cm/s).

The 150 μW laser signal detected on the opposite side of the column was recorded ten times per second. laser power measurements were normalized by dividing the measured value by the steady-state value obtained for bubbles coalescing under the same conditions in pure water alone. The glass column was heated by wrapping a heating tape (product no.: BWH051020LD, from BriskHeat), 13 mm wide and 600 mm long, around the length of the column, except on the path of the laser. The heating tape was regulated by a temperature controller (product no.: TC4X-2, from BriskHeat) connected to a probe placed between the heating tape and glass column. Temperature tolerance was set to ± 1 °C.

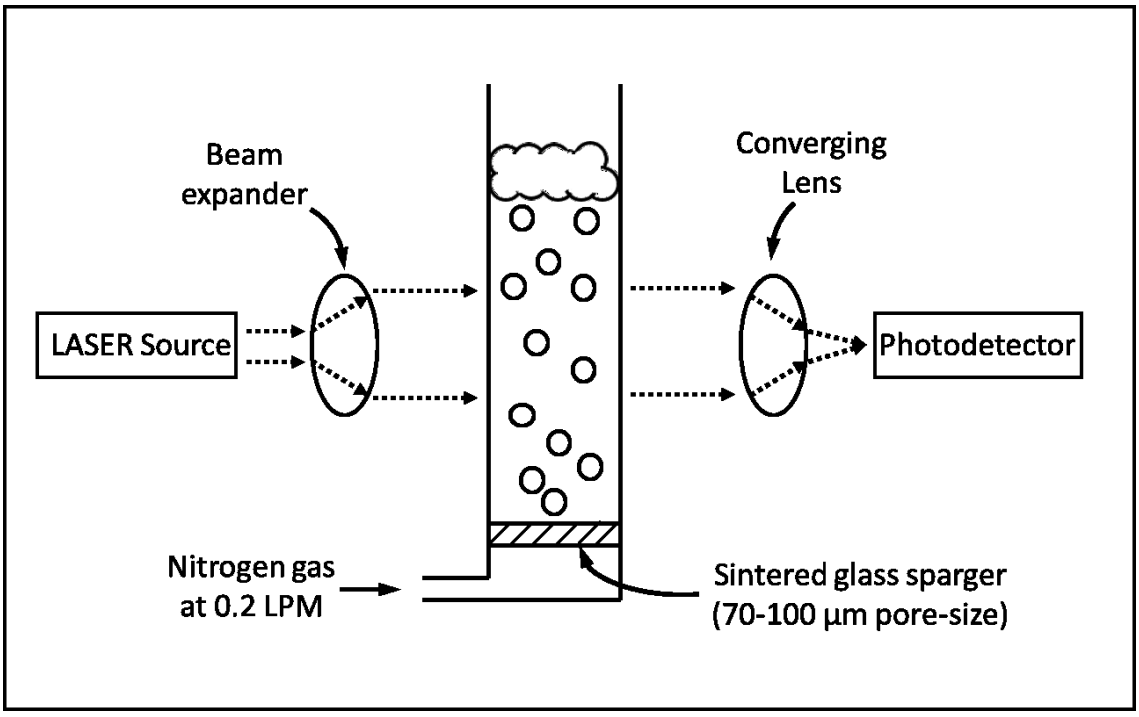

Figure 3-2: Illustration of bubble swarm size apparatus, after Craig et al. (1993)

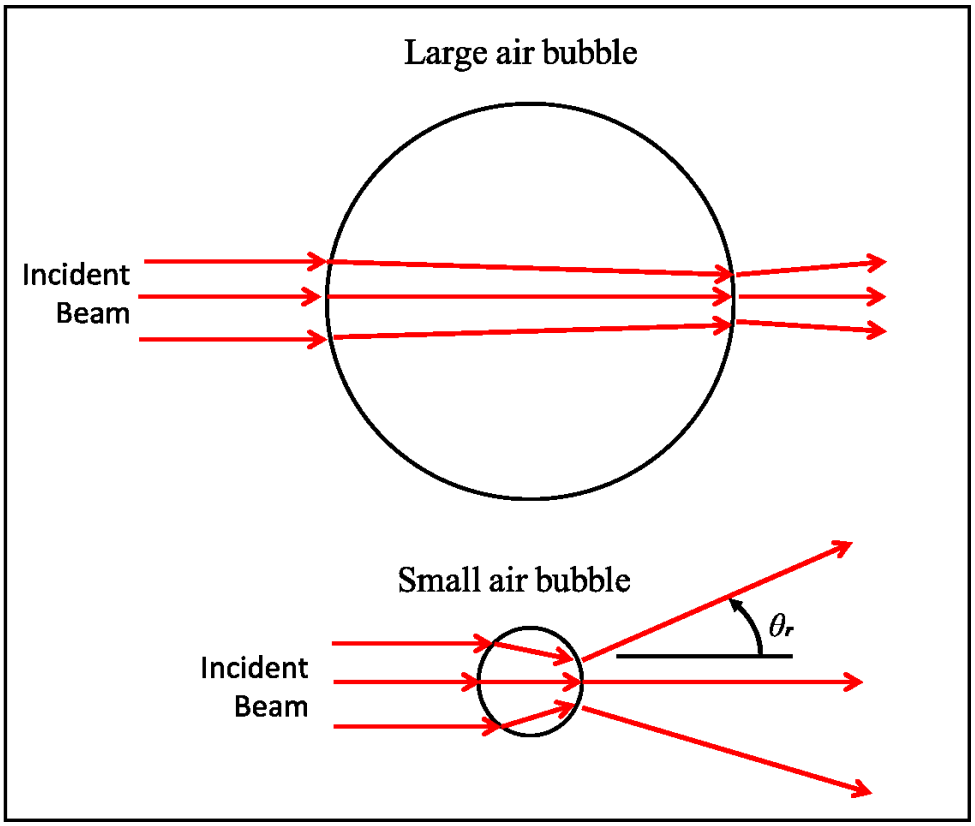

Figure 3-3: Effect of relative bubble size on scattering of light. Smaller bubbles will scatter more light due to the greater portion of the incident signal that meets interfaces with large angles of incidence.

3.2.3 Equilibrium Surface Tension

All equilibrium surface tension measurements were performed using a K12 tensiometer (Kruss), employing the Du Noüy ring method (Kruss, n.d.). In this method, a platinum-iridium ring of fixed circular shape and diameter is lowered to air-water surface. The ring is made of platinum-iridium because of its favourable wettability, and because it is chemically inert – aiding removal of impurities. The liquid adheres to the ring, and the ring is lifted upward. The resistance force from adhesion to the liquid is measured by an internal strain gauge. The surface tension is calculated from the measured force by (Equation 3-5).

$$\gamma = \frac{F}{l \cos \theta_c}$$

(Equation 3-5)

Where,

- F is the force measured
- γ is the surface tension
- θ_c is the contact angle between liquid and the ring
- l is the total contact line between ring and liquid: the inner and outer circumferences, defined in (Equation 3-6).

$$l = 2\pi r_{outer} + 2\pi r_{inner}$$

(Equation 3-6)

Where,

- r_{outer} is the outer diameter of the ring
- r_{inner} is the inner diameter of the ring

Because the ring is made of the platinum-iridium, the contact angle is close to zero, $\cos(\theta) \sim 1$; and because $l >> r_{outer}$, $l \sim 4\pi r_{ring}$, (Equation 3-5) and (Equation 3-6) is simplified to (Equation 3-7):

$$\gamma = \frac{F}{4\pi r_{ring}}$$

(Equation 3-7)

Temperature of the sample was controlled by an external heated water bath connected to the K12. The temperature was monitored by an internal probe on the K12 within a tolerance of ± 0.5 °C.

To prepare the ring for experiment, a flame was applied by a butane torch to remove deposited impurities. Five measurements were taken at each concentration and the mean value was calculated for report here.

3.2.4 Dynamic Surface Tension

Dynamic surface tension measurements were carried-out using the Attension Theta Optical Tensiometer (Biolin Scientific), and the reverse pendant bubble method. An environmental control chamber from Biolin Scientific was used to hold the sample cuvette, and attached to a heated recirculating bath. The sample temperature was monitored by thermometer, and kept within a tolerance of ± 0.5 °C.

The reverse bubble method is similar to the pendant drop method, except that a less dense phase forms the bubble/droplet within a continuous phase of greater density. Because of this reversed difference in density, the bubble/drop is oriented upward rather than down. In the reverse pendant bubble method, a bubble is produced at the end of an upward-facing capillary immersed in a liquid. The optical tensiometer software takes the phase densities as inputs, detects the shape of the bubble, and fits the dimensionless shape variables to the Young-Laplace equation, (Equation 2-1) to determine surface tension (Ravera et al., 2010). Once the drop or bubble has reached mechanical equilibrium, the

competing forces which determine the drop shape or body forces (pulling away from the capillary) and surface tension resisting the applied stress.

Surface tension measurements began once the bubble was detected by the software – soon after production. Measurements were discarded that were collected before the bubble volume variation was shown to be less than 0.4 μL/s. This was done to ensure that the measured changes in surface tension were not linked to initial growth of the bubble in generation. At least three trials were run at each concentration. Measurements were removed that varied by more than 2 mJ/m^2 from the local 15-point mean, as these were more likely caused by changes in the software detection of the bubble, rather than an abrupt change in surface tension.

3.3 Results

3.3.1 Foamability and Foam Stability

The foam produced after 90 s of sparging has been plotted in Figure 3-4. A transition concentration is indicated near 20 mg/L for this PNIPAM molecule at room temperature of 20 °C, where a sudden increase in foam production is seen with increasing polymer solution concentration. At concentrations beyond this point, PNIPAM performs as an effective foaming agent. For trials of PNIPAM solutions at 37 °C, there was no similar transition concentration observed. Under these conditions, PNIPAM appears to be a poor foaming agent.

The same results for a SDS-stabilized foam are plotted in Figure 3-5. SDS is a common surfactant that has been studied extensively (a search on the Thomson Reuters Web of Science Database for only "sodium dodecyl sulfate" in the title field produced more than 4300 results, in January 2017). The transition concentration for SDS is approximately 200 mg/L – one order of magnitude greater than that of PNIPAM under the same conditions. This transition occurs well-below the SDS critical micelle concentration of 8.2 mol/m^3 (Prins, 2015), or 2400 mg/L. The volumes of foam generated by SDS solutions were not affected by temperature – producing similar volumes of foam at both 20 °C and 37 °C.

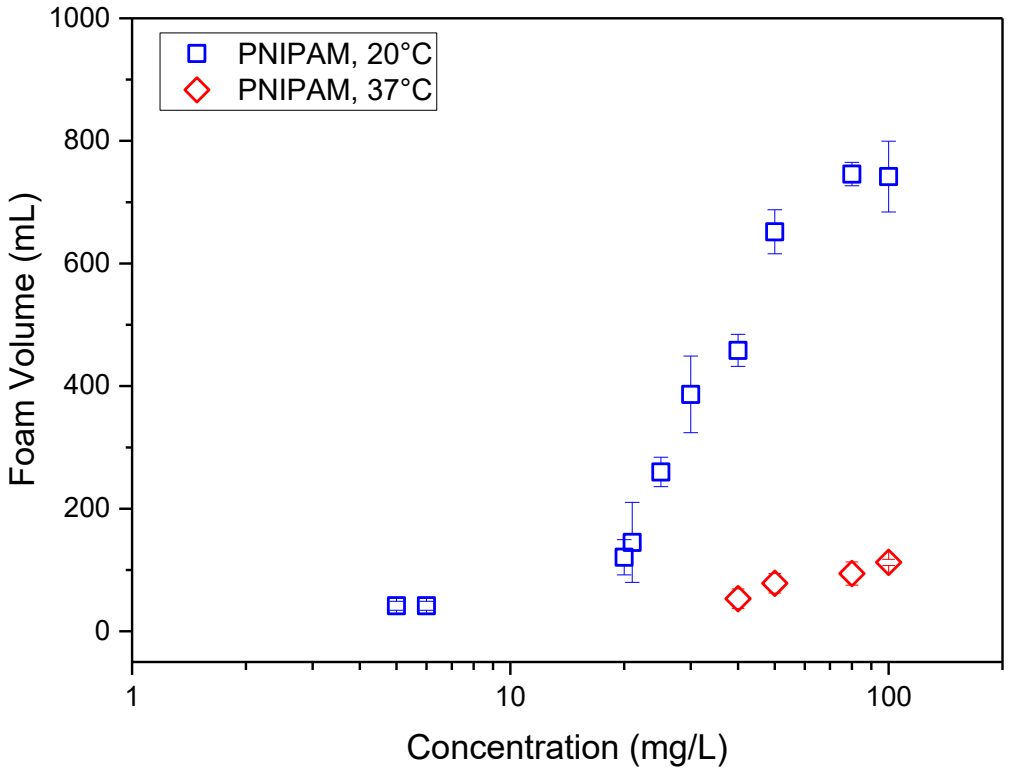

Figure 3-4: Volume of foam generated by 100 mL of PNIPAM aqueous solution after 90 s of sparging at 0.5 L/min. Experiment conducted at solution temperatures of 20 °C (blue squares) and 37 °C (red diamonds).

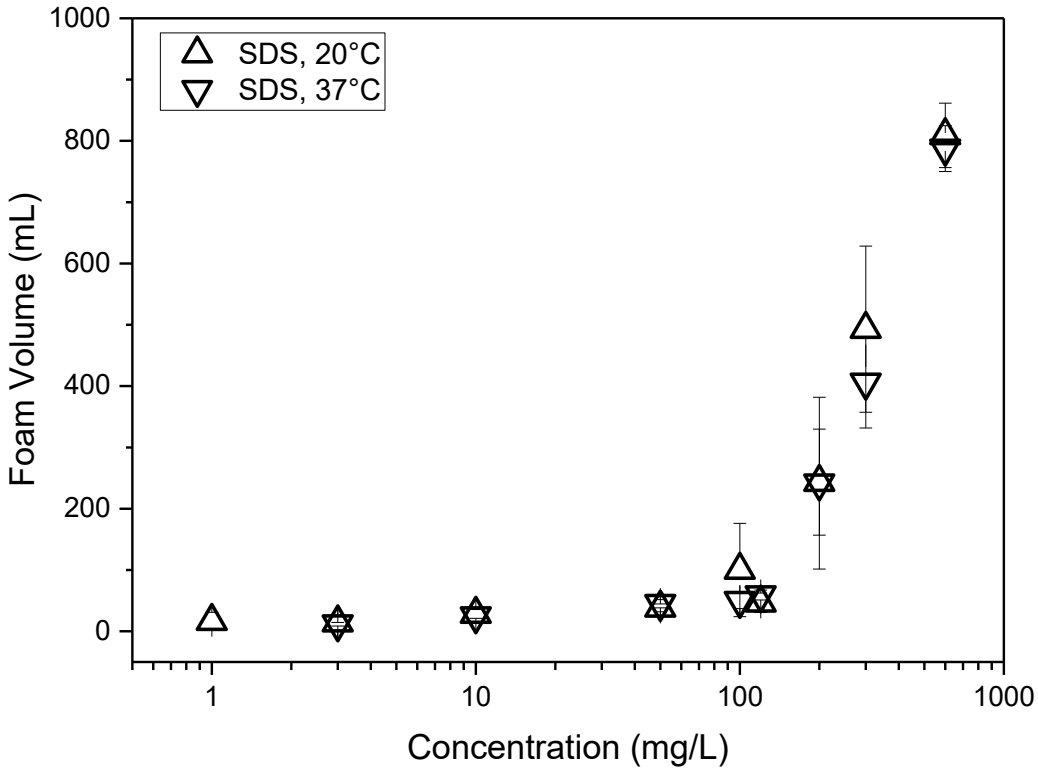

Figure 3-5: Volume of foam generated by 100 mL of SDS aqueous solution after 90 s of sparging at 0.5 L/min. Experiment conducted at solution temperatures of 20 °C (upward triangles) and 37 °C (downward triangles).

The foam volume results of two trials of dynamic testing are plotted together in Figure 3-6, and clearly show the foam can be controlled in-situ by temperature alteration. In administering the 50 ºC shower, the decline in foam volume continued after the shower was complete. The solution reached an equilibrium temperature of 29 ºC, and foam volume decreased to 60 mL from an initial volume of 675 mL. For the trial of a room temperature shower, after the initial foam diminishment due to the falling droplets, the foam volume began to grow again, and returned to its original volume of 663 mL, in a time of approximately 4 s.

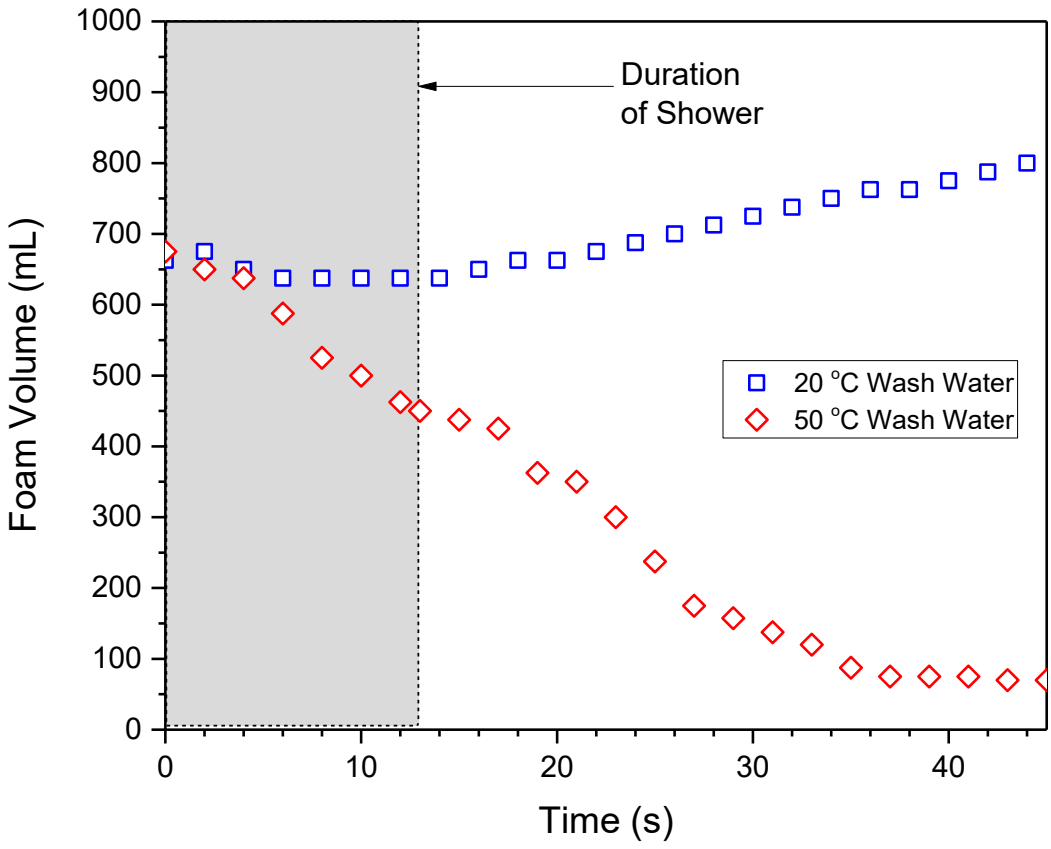

Figure 3-6: Example of two "shower experiments" with similar initial foam volumes. Showers of two different temperatures (20 °C – blue squares, and 50 °C – red diamonds) were administered to foam which had been generated after 90 s of sparging. The shower was administered for a duration of 13 s, in this case (denoted by the gray area of the plot).

Despite the difficulty of controlling the shower duration, results were repeatable for both temperatures of shower. Foam volume decreased an average of 5% during administration of the 20 °C shower, and 43% during the 50 °C shower. Even more importantly, the foam which encountered 20 °C wash water recovered by 8% in the 10 seconds after completion of the shower. The foam encountering 50 °C wash water decreased an additional 44% in the same 10 second interval. The full details are shown in Table 3-1. These results show that a PNIPAM-stabilized foam can be tuned in-situ by

changing the temperature with a shower, as would be required for a tunable frother in an operating flotation column.

Table 3-1: Effect of wash water temperature on foam collapse for a PNIPAM aqueous solution, with concentration of 50 mg/L.

Trial	Shower Temperature	Duration of Shower	Volume Change Through Shower	Volume Change 10 s After Shower
	(°C)	(s)		
1	20	16	-16%	15%
2	20	13	-4%	6%
3	20	13	4%	5%
Mean Value	20	14	-5%	8%
4	50	20	-49%	-51%
5	50	13	-50%	-44%
6	50	12	-31%	-35%
Mean Value	50	15	-43%	-44%

3.3.2 Swarm Bubble Size Reduction

Using the laser intensity apparatus, the relative coalescence of bubbles in the bulk were recorded continuously through ten minutes of nitrogen gas sparging. The initial laser intensity values are plotted in Figure 3-7. For higher concentrations of PNIPAM, and especially at room temperature, there was an immediate increase in the laser signal from

the initial value upon sparging beginning, until an equilibrium value was reached. The equilibrium laser signal values are plotted in Figure 3-8.

The initial laser signal values, as shown in Figure 3-7, are very similar at high and low temperature. This indicates that, at least at the outset of the experiment, the size of bubbles stabilized by PNIPAM are not affected by temperature, but by PNIPAM concentration alone. However, at greater PNIPAM concentrations, there is a pronounced difference in the measured equilibrium signal between the two temperatures studied: a smaller signal at 37 °C, and a greater signal at 20 °C. This indicates that once the system has reached its steady-state, the bubbles generated in a PNIPAM solution at 20 °C are actually larger than those in a 37 °C solution.

To investigate the difference in bubble size at steady-state where there is no apparent difference in the initial values, the bubble size data was reviewed alongside the foam production data of the same trial. Figure 3-9 shows the laser and foam data superimposed for two trials (one high temperature, one low) at a concentration of 10 mg/L. Following the data for 20 °C, there is an initial increase in the laser signal (indicating an increase in the size of bubble passing through the measurement zone), which coincides well with the increase in foam volume produced at the same time. At a point approximately 110 s after the start of sparging, the laser signal reaches a plateau, and the foam volume begins to decrease. There is no such rise in laser signal and/or foam volume for the 37 °C case. A plausible explanation for the rising laser signal (indicating larger bubbles) in the outset of the 20 °C experiment, is that as foam is produced at the top of the column, the bulk concentration of PNIPAM is also being depleted. In that case, the steady-state signal is not indicative of the bubbles produced at the original concentration of the solution, but some lower value. It is possible that the same rapid change in signal is not observed at 37 °C because the low foam volume allows PNIPAM to recirculate back into the bulk more readily.

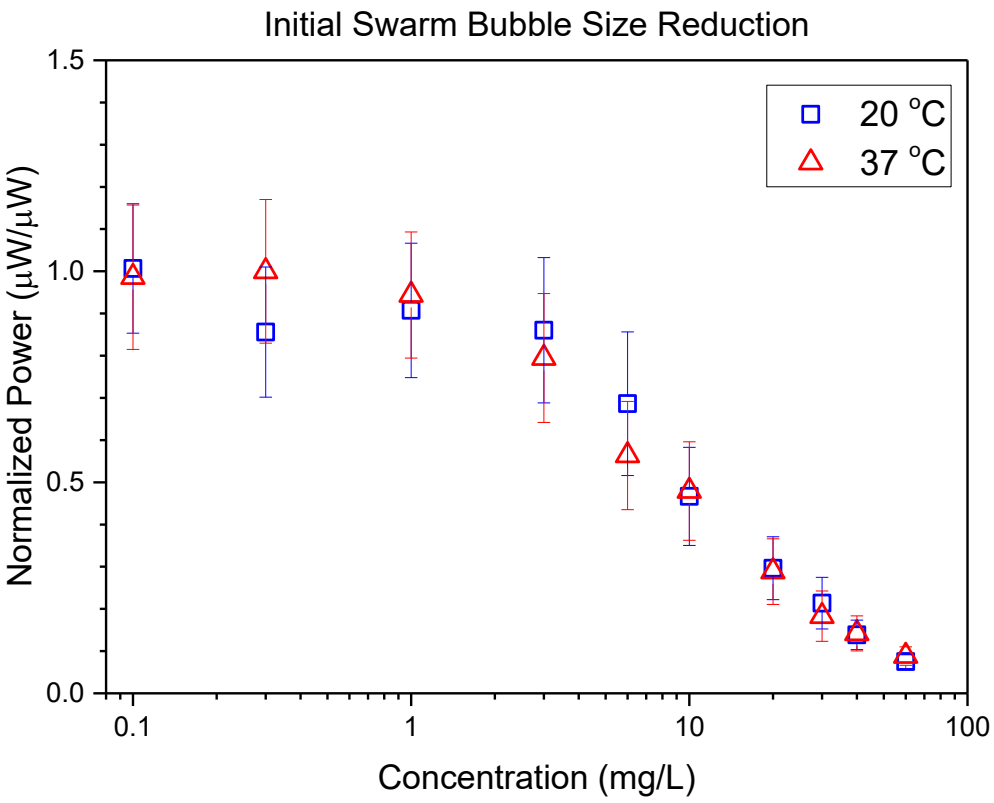

Figure 3-7: Initial laser power detection in the swarm bubble size experiment for PNIPAM aqueous solution of 20 °C (blue squares) and 37 °C (red triangles).

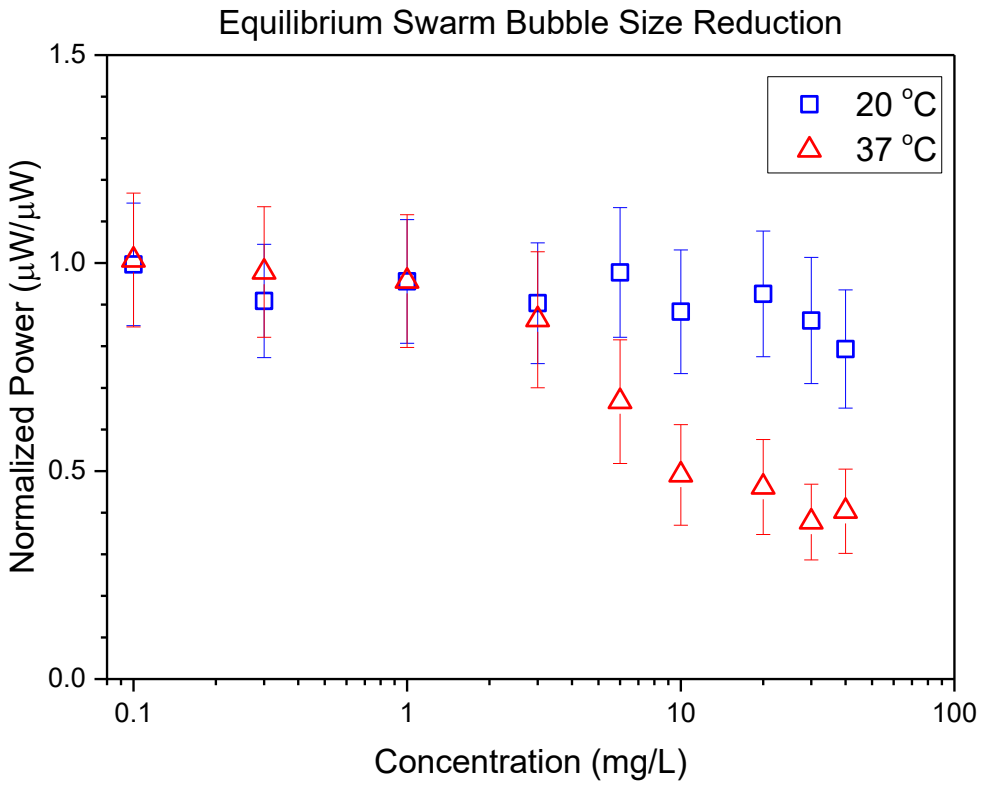

Figure 3-8: Equilibrium laser power detection in the swarm bubble size experiment for PNIPAM aqueous solution of 20 °C (blue squares) and 37 °C (red triangles).

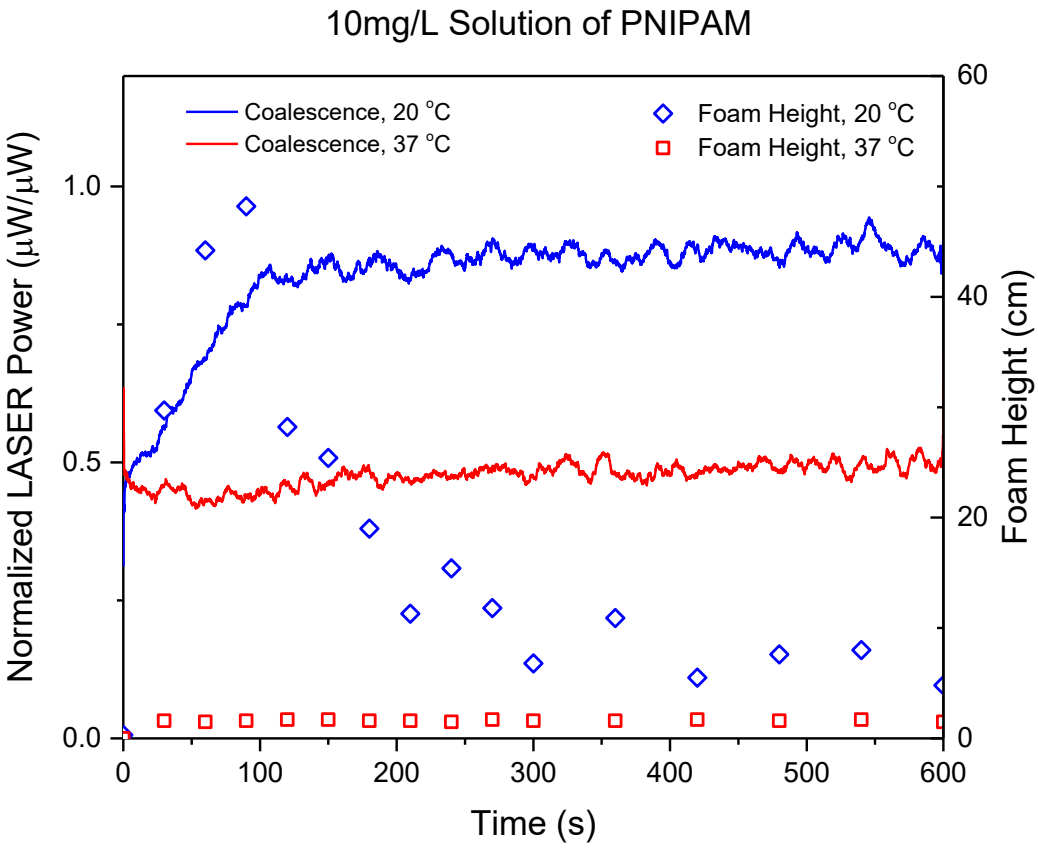

Figure 3-9: Example of temporal laser data for two trials of PNIPAM aqueous solution, superimposed on plot of foam height for the same trial.

3.3.3 Equilibrium Surface Tension

Surface tension measurements (Figure 3-10) were found to be consistent with previous studies of PNIPAM (Lee et al., 1999). The surface tension at concentrations above surface saturation are approximately 44 mJ/m^2 at 20 °C and 41 mJ/m^2 at 37 °C. The measurements above LCST are consistently lower than those below LCST. This can mostly be accounted for by the decrease in surface tension with increasing temperature for pure water. According to the values obtained by Floriano and Angell (1990), surface tension of pure water is approximately 2.7 mJ/m^2 lower at 37 °C compared to 20 °C.

Additionally, Lee et al. (1999) showed that adsorption density increases with temperature for aqueous PNIPAM solutions.

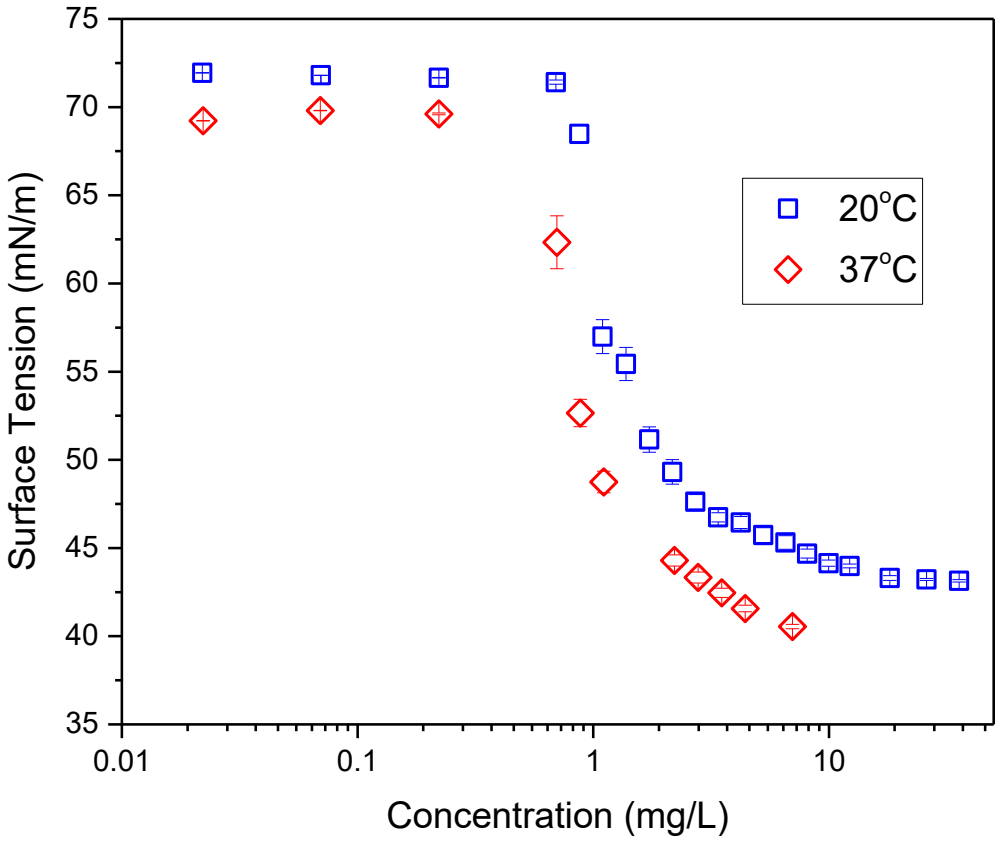

Figure 3-10: Equilibrium surface tension of PNIPAM aqueous solution at 20 °C (blue squares) and 37 °C (red diamonds). Measurements conducted by the Du Noüy ring method using a Kruss12 tensiometer.

3.3.4 Dynamic Surface Tension

Dynamic surface tension measurements were made to elucidate a difference in rate of adsorption for trials above and below LCST. Figure 3-11 illustrates, as a typical example, two trials of 30 mg/L PNIPAM at 20 °C and 37 °C, respectively. The initial slope of the case above LCST is less steep than the case below the LCST, but the high temperature

trial does approach a lower equilibrium value, which is consistent with the results in 3.3.3.

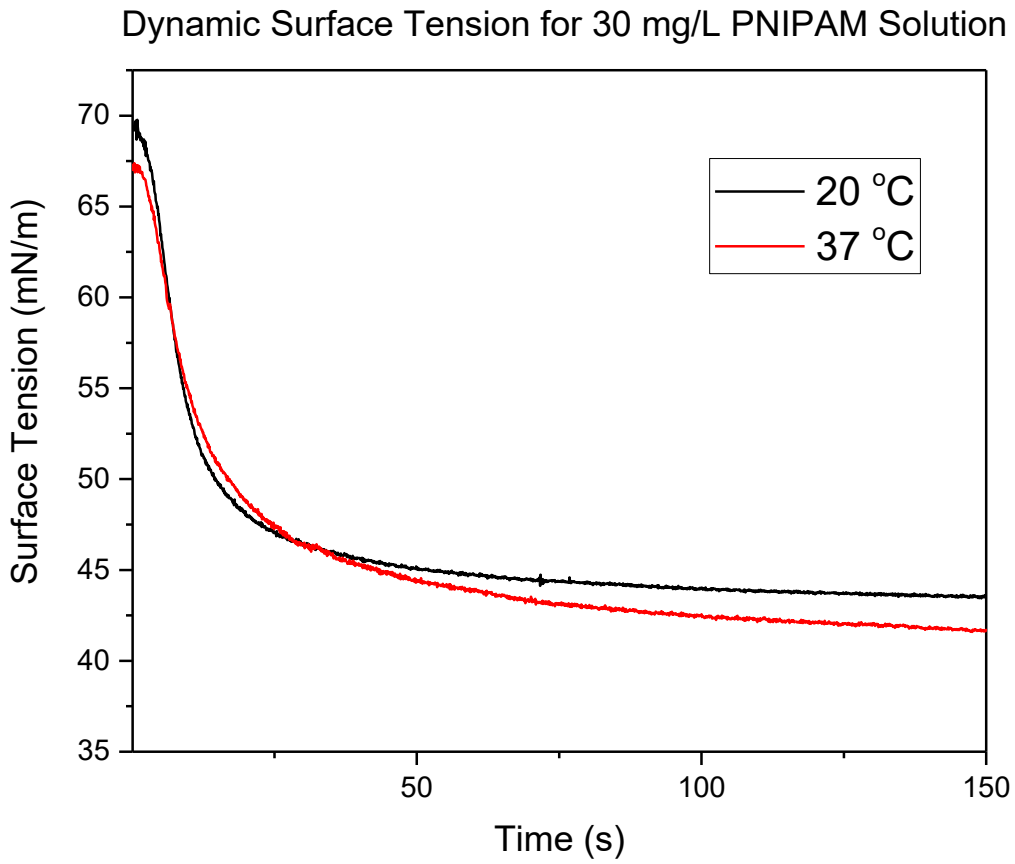

Figure 3-11: Dynamic surface tension of 30 mg/L PNIPAM aqueous solution at 20 °C (black) and 37 °C (red). Measurements taken using pendant bubble method with optical tensiometer.

The initial slopes have been calculated for all trials, and the mean of calculated values at each concentration, are plotted in Figure 3-12. At least three trials were used for each calculation, and in the case of trials of 100 mg/L, at least ten trials were used because of the difficulty of capturing repeatable data due to the immediate rapid change in surface tension upon bubble generation. It is shown in Figure 3-12 that the rate of adsorption is slightly greater for the trials below LCST. LCST is commonly called the "cloud-point" due to the turbidity observed from precipitating and aggregating PNIPAM molecules as temperature is increased above this point (Schild, 1992), and was first noted

by Scarpa et al. (1967). This aggregation may reduce the mobility of PNIPAM, and hinder its travel to the interface, resulting in the slightly more rapid adsorption rate below LCST, as in Figure 3-12.

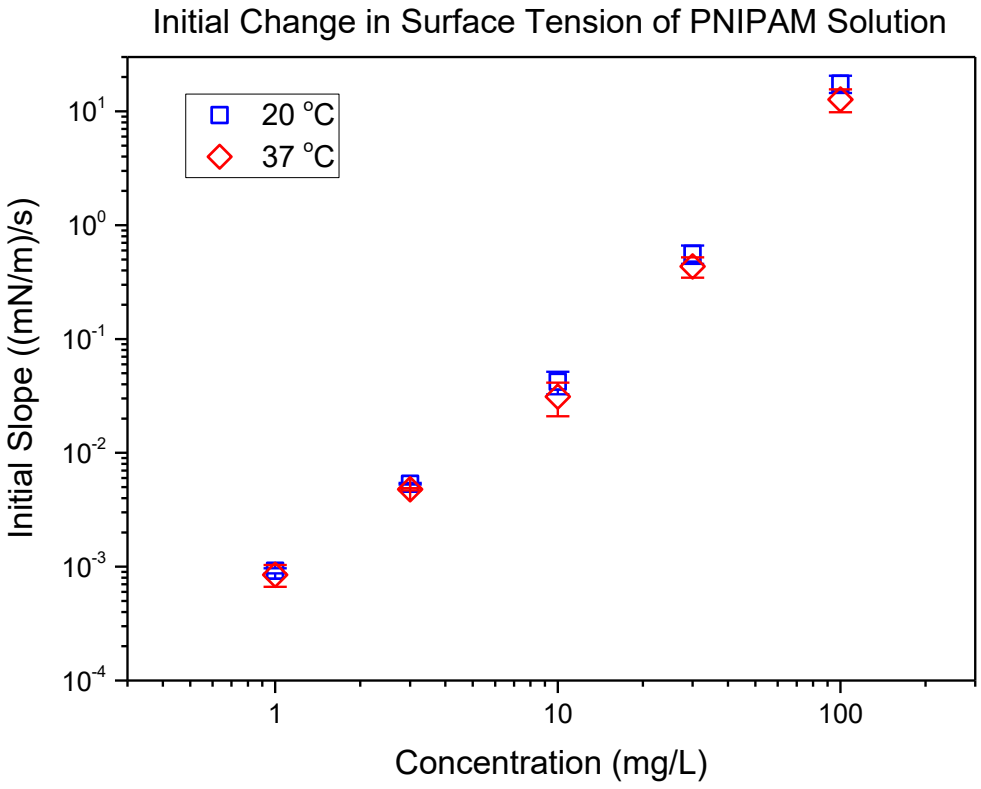

Figure 3-12: Initial change in slope of dynamic surface tension measurements for PNIPAM aqueous solutions at 20 °C (blue squares) and 37 °C (red diamonds).

3.4 Discussion

The conventional methods to describe foam is by the foamability and foam stability. Foamability quantifies the foam generated while gas is introduced into a liquid system from a method, such as sparging, agitation, cavity nucleation, etc. The lifetime of a foam, or rate of decay after foam generation is stopped, describes the foam stability (Bikerman, 1973). In this work, the volume of PNIPAM-stabilized foam generated in a given time (90 seconds) was studied. By conventional descriptions, this might be viewed as a study of foamability, but the effects of foam stability in foam accumulation in this procedure

cannot be ignored. In other words, a more stable foam will contribute to greater foam accumulation during generation. For this reason, the term foamability has been used here to characterize the accumulation of foam at the top of the liquid phase through sparging. This measured accumulation may be due to more rigorously defined foam stability or foamability; or a combination of both. Due to the nature of this experiment, the two properties cannot be delineated here.

The key finding is a tunable foam-stabilizing agent in PNIPAM. This is in direct contrast of the conclusions by Guillermic and Saint-Jalmes (2013) who determined the foamability of PNIPAM to be equally weak above and below the LCST. A difference between this work and that is the measurement of a peak foam volume here, and measurement of liquid volume fraction in their work. In search of the same evaluation, the properties measured are obviously different. Additionally, the Guillermic and Saint-Jalmes (2013) work studied a polymer with molecular weight of 25000 g/mol, which is approximately 3.6 times the size of polymer studied here. They also used dosages of 1 g/L and 10 g/L, which amounts to 10 to 100 times the dosage here, or 2.9 to 29 times the molar concentration.

The difference in foam volume after sparging, observed above and below the LCST, indicates a capability to "switch" or "tune" the foamability characteristic. As shown in Figure 3-6, the volume of foam at the top of the column can be adjusted as quickly as the environmental temperature can be changed. This property, along with the behaviour of bubble size reduction in the bulk, meets the three main criteria set-out for a frother in Section 3.1 (the third criterion – slowed bubble rise velocity – is affected by bubble size reduction).

Equilibrium and dynamic surface tensions were studied to determine whether adsorption may play a significant role in the different foamability behaviour observed. The PNIPAM molecule seemed to behave similarly both above and below the LCST in these experiments, as well as the bubble size reduction experiments – another indication that similar adsorption occurs on the bubbles before joining the foam. Considering similar

adsorption of PNIPAM on swarm bubbles at temperatures above and below LCST, it is not a likely mechanism for the tunable foam observed in Section 3.3.1.

While the mechanism for tunable foam was not found here, the key finding is that PNIPAM gives the operator two "levers" to adjust in flotation column optimization. The first lever, PNIPAM concentration, can be set to effectively reduce bubble size in the slurry bulk. The second lever, temperature, can be adjusted in-situ to achieve the appropriate froth stability without reducing efficacy of the first lever.

Here, only a two-phase system (foam) with no other reagents present was studied. To determine the feasibility of PNIPAM as a coal flotation frother, future work should include study of the interactions in a system containing fine coal particles, as well as other reagents commonly employed in column flotation. Additionally, the mechanism(s) for changing foamability must still be uncovered so that a stimuli-responsive polymer may be designed to suit the specific application of column flotation.

Chapter 4: Foam Coarsening and Drainage

4.1 Introduction

In this chapter, an analysis is provided of the structure of a PNIPAM-stabilized foam to determine the extent of which foam stability of this system is dominated by coarsening or coalescence. After it is shown that the time scale of coarsening is much greater than the lifetime of a foam cell in this system, the mechanisms leading to coalescence are explored by an interferometry technique on a single draining air bubble (air enclosed by a liquid film in the atmosphere).

For all the thin-film measurement techniques discussed in Section 2.1.2, the liquid film thickness was measured using the interference pattern created by light transmitted through, or reflected by the film. In most cases, a single monochromatic light source is used. For measurements using monochromatic light, a Newton Black Film must be

reached before rupture occurs to calculate the film thicknesses denoted by preceding interference fringes (Exerowa and Kruglyakov, 1998). The Newton Black Film, in interferometry of reflected light, represents the zeroth order minima fringe, where the normalized phase shift of interfering light beams approaches π, due to the difference in optical path of the two beams approaching zero, and the inversion of the initial beam – reflected at the first air-water interface. Without achievement of a Newton Black Film, the order of fringes cannot be known, and so this method cannot be used for films that may rupture at greater thicknesses.

Interferometry of a white light source removes the need for a Newton Black Film, as the overlapping interferometric patterns of all wavelengths within the visible spectrum combine to produce a single visible colour (Afanasyev et al., 2011), or from which, the red, green, and blue components may be extracted digitally to produce three unique, comparable interference patterns (Sett et al., 2013). The main drawback of a white light source is that interference patterns for the entire spectrum will be created, and when detected by a 3-channel (RGB) CCD camera, will produce spectra of overlapping interference patterns on each channel – giving a "fuzzy" image that becomes less reliable at greater film thicknesses.

In this work, three light sources were used, each of different wavelengths, to produce the interference patterns measured on a draining bubble. By using three wavelengths, the drawback of white light has been mitigated, while maintaining the ability to determine the film thickness without achieving a Newton Black Film, as required by a single monochromatic light source method.

4.2 Materials & Methods

In these experiments, PNIPAM, with carboxylic termination, LCST of 32 °C, and molecular weight of 7000 Da; and sodium dodecyl sulfate (SDS) were procured from Sigma-Aldrich to prepare test solutions. Water for test solutions was filtered through an EMD Millipore Milli-Q water purification system with Millipak 0. 22 μm filter and product resistivity of 18. 2 MΩ·cm.

4.2.1 Growth of a Foam Cell

In a 40 °C PNIPAM (concentration of 50 mg/L) foaming column (described in Section 3.2.1), the growth of a single foam cell was monitored from joining the foam at its bottom to finally coalescing with the atmosphere at the top of the column. A cell that was quite large before coalescing with the atmosphere was selected for this analysis. The video was reviewed in reverse to determine all the bubbles which would contribute – through coalescence – to the growth of the studied bubble. Review and analysis of the video was conducted using ImageJ. ImageJ is an image processing software based in Java, is open source, and has been cited in more than twenty thousand scientific publications (Schneider et al., 2012). The projected area of the studied bubble, and all contributing bubbles were measured by manual tracing of a polygon on each cell at each video frame using the "polygon selection tool". The measured areas were then converted to diameters for circles of equivalent area.

4.2.2 Calculation of film thickness from interference pattern: Theory

In the simple case of interferometry using a single monochromatic light source transmitted through an orthogonal liquid film plane, the reflected beam will travel twice the thickness of the film before realigning with the incident beam, as in Figure 4-1. The exact phase shift, $\Delta\varphi$ in (Equation 4-1), of the reflected beam relative to the incident beam depends on the difference in optical path, Δd, and the wavelength of the beam, λ. The optical path, calculated in (Equation 4-2) is a function of both the refractive index of the liquid, n_l, and the film thickness, h.

$$\Delta\varphi = \frac{2\pi}{\lambda}\Delta d$$

(Equation 4-1)

$$\Delta d = n_l 2h$$

(Equation 4-2)

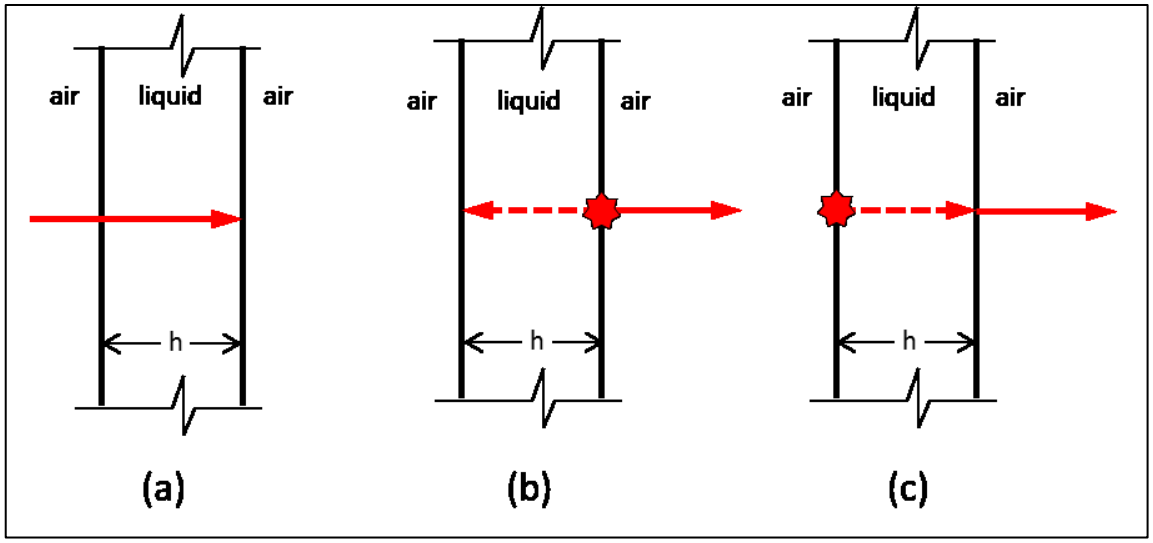

Figure 4-1: Path of single light beam in interferometric technique. Incident light travels through liquid (a); a portion of incident beam passes through, and a portion is reflected (b); some of the reflected beam is reflected again on the first interface, realigning with the incident beam, but having traveled and additional optical distance of $2hn_l$. The additional optical distance travelled determines the phase shift of the second beam compared to first, and thus the interference (constructive or destructive, and to what degree).

For the case of interferometry of a spherical bubble, there is only one point at the center ($r = 0$), where the angle of incidence, θ is orthogonal to the film surface. At all other locations, the non-orthogonal angle of incidence will give a light path that is shifted radially outward on the projected circle, as described in Figure 4-3. This gives a calculation of the difference in optical path, and thus, film thickness, which must be based on the radial location of the beam, r.

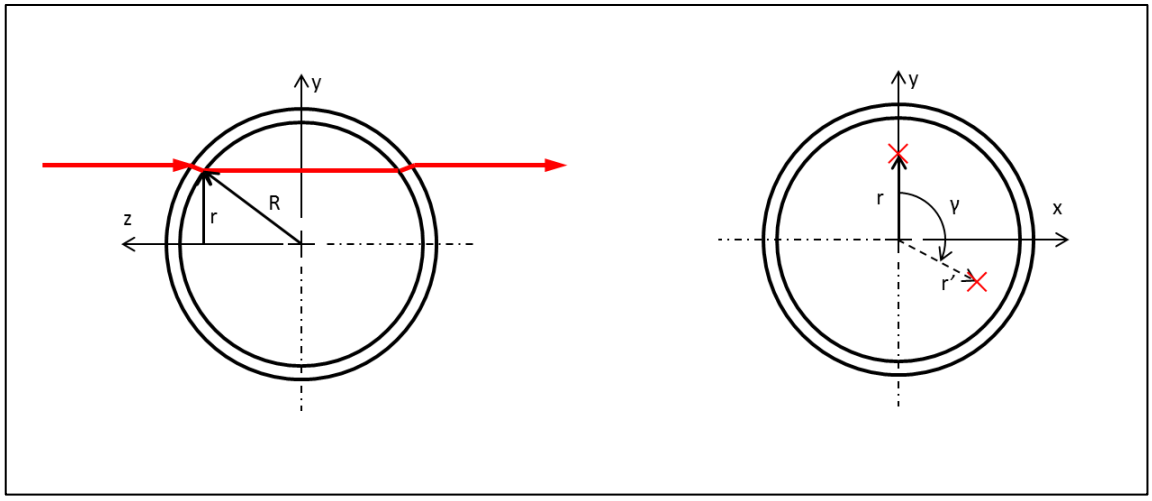

Figure 4-2: Path of a light beam encountering the bubble at a location of projected radius, r.

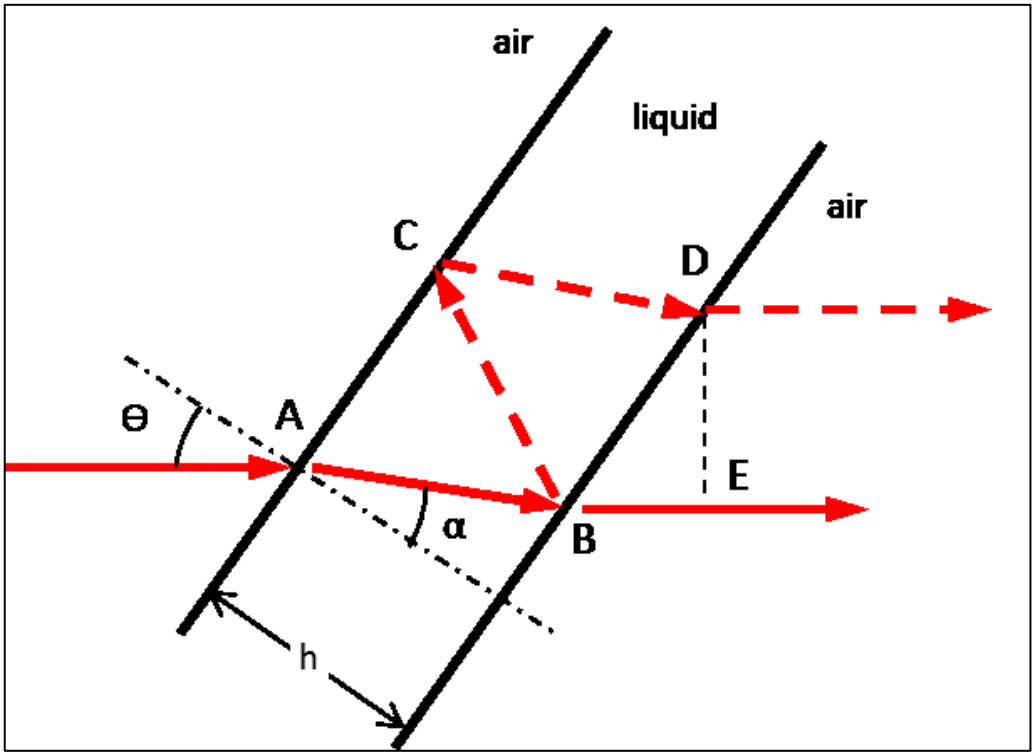

Figure 4-3: Paths of incident and reflected light beams on a non-normal film plane

The difference in optical path, between incident beam and reflected (interfering) beam, Δd:

$$\Delta d = n_l(\overline{BC} + \overline{CD}) - n_a\overline{BE}$$

$$= 2n_l \frac{h}{\cos\alpha} - n_a\overline{BA}\sin\theta$$

$$= 2h\left(n_l \frac{1}{\cos\alpha} - n_a \tan\alpha \sin\theta\right)$$

$$= 2hn_l\left(\frac{1}{\cos\alpha} - \frac{\sin^2\alpha}{\cos\alpha}\right)$$

$$= 2hn_l \cos\alpha$$

(Equation 4-3)

This calculation of difference in optical path accounts for the changing angle of incidence at each point, r (defined in Figure 4-3), but neglects the local change in curvature between entry of the incident beam (point A), and exit of the reflected beam (point D), as the radial shift, $\overline{DE}$, is sufficiently small.

Definition of the angle of incidence, using polar coordinate system:

$$\cos\theta = \frac{z}{R} = \sqrt{1 - \frac{x^2 + y^2}{R^2}} = \sqrt{1 - \frac{r^2}{R^2}}$$

(Equation 4-4)

Definition of the difference in phase, $\Delta\varphi$, at a given point γ,r:

$$\Delta\varphi = \frac{2\pi}{\lambda}\Delta d$$

$$= \frac{4\pi h}{\lambda} n_l \cos\left(\sin^{-1}\left(\frac{n_a}{n_l}\sin\left(\cos^{-1}\sqrt{1-\frac{r^2}{R^2}}\right)\right)\right)$$

$$= \frac{4\pi h}{\lambda} n_l \sqrt{1-\frac{{n_a}^2 r^2}{{n_l}^2 R^2}}$$

(Equation 4-5)

Since this method identifies the locations of the interference fringes, the difference in phase is extracted only at maxima and minima, so:

$$h = \frac{m\lambda}{4 n_l f_{curv}} \quad , \text{ m} = 0,1,2,3,\ldots$$

(Equation 4-6)

Where, $$f_{curv} = \sqrt{1-\frac{n_a^2 r^2}{n_w^2 R^2}}$$

(Equation 4-7)

4.2.3 Generation of Single Draining Bubble

Glass capillary tubes were purchased from Fisher Scientific (product no.: 22-362574, from Fisherbrand), with inside diameter of 1.1 - 1.2 mm, and outside diameter of 1.5 – 1.6 mm. The capillaries were given a hydrophobic treatment using hydrolysis with dichloromethylsilane to increase contact angle – preventing the bubble from wetting, and being drawn down the outside of the capillary. The capillary tips were submerged to 2 cm in a vial of dichloromethylsilane for ten minutes. The capillaries were then rinsed with milli-Q water, dried by flowing nitrogen, and then placed in an oven for 18 hours at 60 °C.

The untreated end of the capillary was attached to polyethylene tubing, oriented pointing upward, and fixed by a mount on an optical breadboard. A micropipette was used to place 1.2 μL of the liquid solution over the top of the capillary. When a new capillary was used, water was placed in the top of the capillary and left overnight. This was done to increase the hydrophilicity of the annulus and enhance pinning of the generated bubble. A syringe pump connected to the capillary tubing was used to drive the air for bubble generation. A volume of 0.5 mL of air was driven into the bubble at a rate of 0.15 mL/s.

For high temperature experiments of 40 °C, a box was built, lined with 25 mm thick rigid foam insulation (Owens Corning Foamular 150) with R-value of 5, and all joints were caulked to limit air flow. The box covered the entire apparatus, including: capillary, camera, and light source assembly. The computer, syringe pump, oscilloscope, and LED controller were kept outside the box, with small channels made to route cords and tubing. The box has a 125 mm x 125 mm square opening with cover immediately above the capillary location, for access to liquid addition with a micropipette. A 5 mm diameter hole was cut in the top for placement of a thermometer. The inside of the box was heated by coils of flexible copper tubing (0.25 inch nominal diameter) which were run back-and-forth under the optical breadboard, recirculating water from a heated bath setup outside the box. A small fan, removed from a children's toy for blowing bubbles was used to circulate the air inside the box during heating – ensuring a uniform temperature distribution throughout. The fan was shut-off during experiment so as not to affect premature rupture of the bubble. After liquid was added to the capillary, and the cover replaced, the fan was run for approximately 5 s to circulate the air, and the temperature was checked on the thermometer for confirmation before a bubble was produced. To ensure the temperature of the liquid solution added to the capillary top would be 40 °C, the bulk solution, from which it was taken, was heated to 40 °C in a beaker on a hot plate and monitored with another thermometer.

4.2.4 Selection of Light Sources and Wavelength Approximations

In the single-bubble interferometry setup, three different LED light sources were used (Mightex LCS-0420-03-22, LCS-0625-03-22, and LCS-0810-02-22) with mean wavelengths of approximately 420 nm, 623 nm, and 805 nm. These three light sources were chosen based on the following criteria:

- Each light source has an emitted wavelength spectrum which overlaps well with only one of the detection spectrums of a single RGB channel for the chosen camera. Each light would be detected using the three RGB channels of a CCD (charge-coupled device) camera so that at every time-step, three images would be produced – one for each light source.
- The spectrum of wavelengths be as narrow as available (as close as possible to monochromatic). This is to prevent detection of light sources except the one intended for that channel.

The three light sources were shone through the thinning bubble and recorded with the three RGB channels of a CCD camera (Basler ace acA2000-165uc), as shown in Figure 4-4.

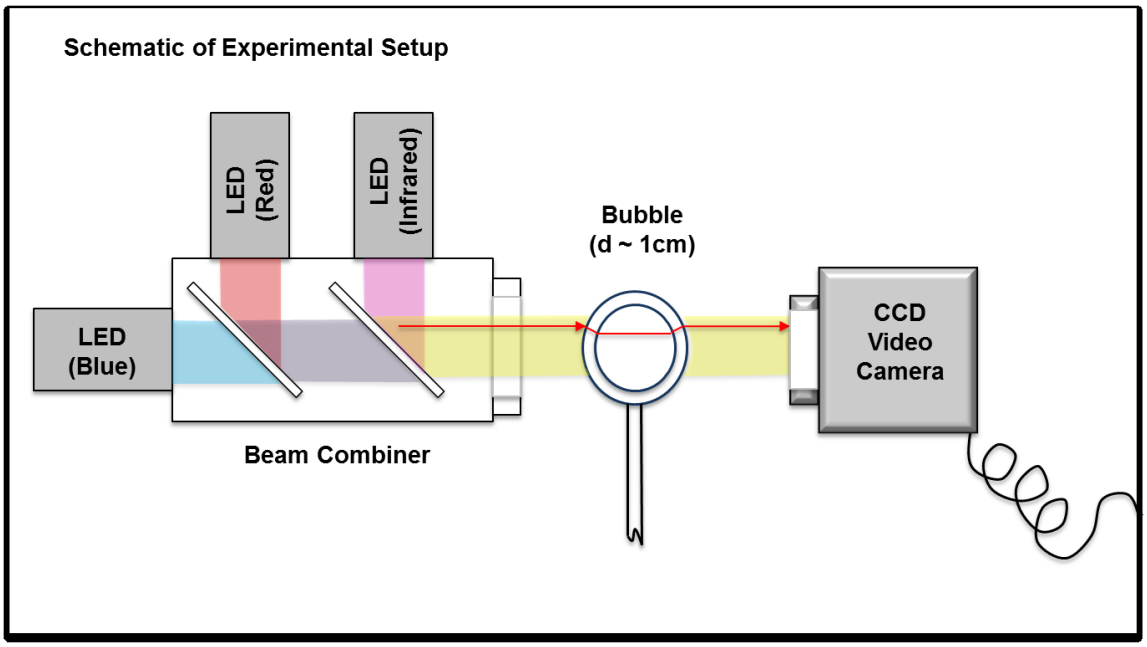

Figure 4-4: Schematic of single bubble three-LED interferometry experimental setup.

The light sources could not be shone on the camera at the same time, as all three camera channels are sensitive to infrared light. While the green channel would detect the infrared signal and a negligible signal of the other two wavelengths, the blue and red channels would detect infrared as well as their respective intended wavelengths, resulting in the superposition of the infrared interference pattern on the red and blue patterns. To remedy this, the camera and light controller (SLC-SA04-US, Mightex) were synchronized using an external trigger signal from an oscilloscope. The oscilloscope was set to a square wave with frequency of 5 Hz, and both software controls were set to trigger on the leading edge of each wave. The camera was set to take a burst of three images after each trigger at a rate of 50 Hz with exposure time of 4000 μs. The blue light was set to trigger immediately, for a duration of 50 μs, while the red and infrared lights engaged 0.02 s and 0.04 s after the trigger for exposure times of 50 μs and 3500 μs, respectively. The exposure times were selected to be as low as possible to increase the sharpness of each image. A limitation of the infrared light was that, even at maximum intensity of 800 mA, a minimum exposure time of 3500 μs was required for a sufficiently bright image to be recorded by the camera. This is due to the relatively low sensitivity of the camera to infrared light, compared to wavelengths on the visible spectrum. The blue and red LED

intensities were set well below the maximum intensity of 1000 mA, at 5 mA and 15 mA, respectively.

4.2.5 Extraction of interference pattern

This section describes the functions of the MATLAB script "a3_ExtractExtrema.m", located in Appendix A along with applicable non-built-in functions called from within the script. Figure 4-5 shows an example of the three images used as inputs for this section of analysis, and the plots of light intensity with extrema marked, which are the output of this step. At each time step, the interference pattern is extracted from the outside edge of each image by a script written in MATLAB, and the locations of fringe pattern maxima and minima are identified. The fringe pattern moves from top to bottom of the bubble, and is taken on both sides. With information taken from two locations on the bubble, the script can later decide which dataset is more reliable (e.g. if a speck of dust or plume of low density film region floats through the data collection zone on one side due to marginal regeneration).

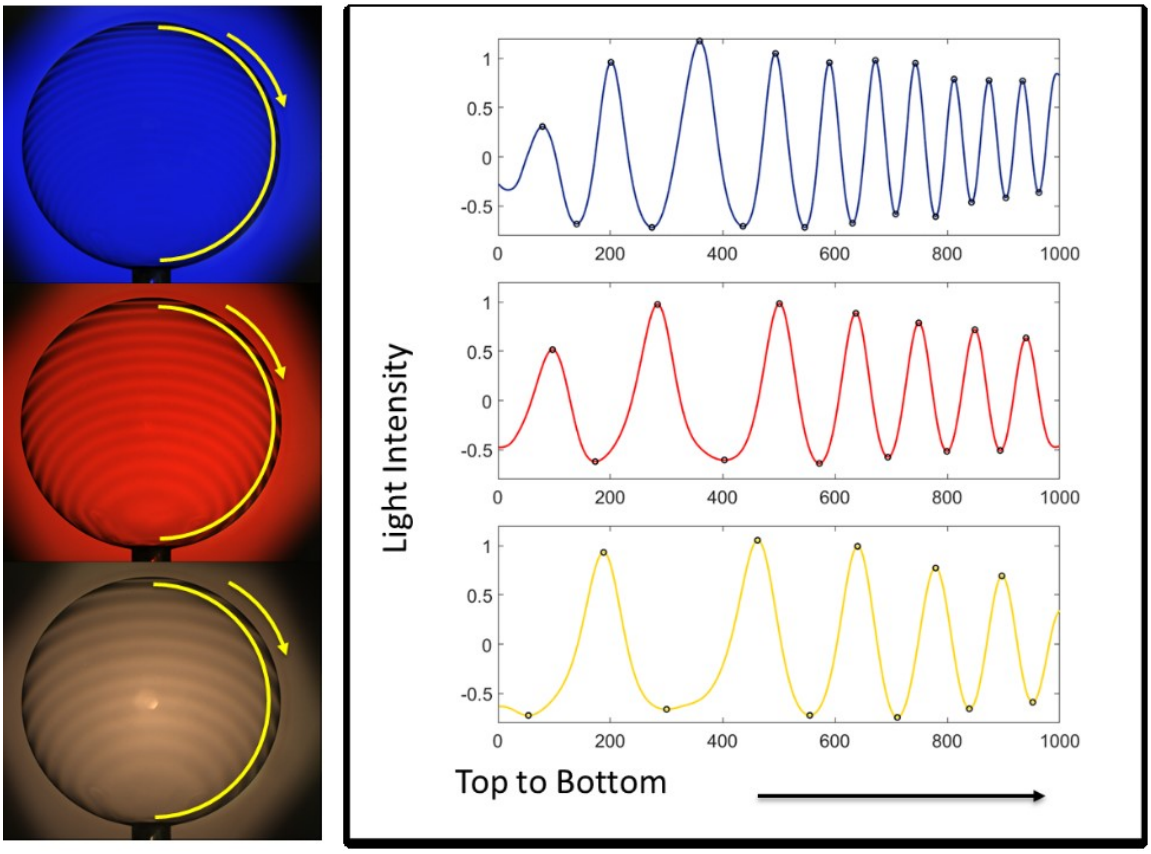

Figure 4-5: Example of three images produced at a single time-step during bubble drainage (top-left: blue, middle-left: red, bottom-left: infrared) and the corresponding interference patterns extracted by the computer script (right).

The steps are as follows:

i. Import the treated images from the results in script "a2_ImagePretreat.m".

ii. The light intensity value is extracted from every point along the circumference of the bubble from the top ($\omega = 0$) down on both the left and right sides ($\omega = \pm 3\pi/4$), as illustrated in Figure 4-6. The bottom portion of the bubble was not used, as it may have liquid pooling which will give false data.

iii. The signal is smoothed by way of a low-pass filter, and then the smoothed signal is input to the FindPeaksx.m function which extracts the locations of all the interference fringes (both maxima and minima). The low-pass filter works most reliably when the desired signal maintains a fairly consistent frequency. The signal frequency directly from the image is often not nearly uniform enough for this function – especially nearing the end of bubble lifetime when the upper part

of the bubble film has become very thin. The light intensity plots in Figure 4-5 illustrate well how the top of the bubble (left-side of the plot) can display a much lower frequency than the lower part of the bubble (right-side of the plot). To remedy this problem, a transformation is performed on the signal to "stretch" the section of the signal which is of higher frequency until it is similar to the low frequency section. To do this:

- A fast-Fourier transform is performed separately on the top third of the signal and the bottom third of the signal. The dominant frequency is extracted at both locations.
- The ratio of the two frequencies is used to multiply the domain as a function of location, as in (Equation 4-8). With the transformed domain, the signal is more readily smoothed to represent to the true signal.

$$x_{trans} = \left(\frac{b_f}{N}\right) x^2 + x$$

(Equation 4-8)

FindPeaksx is then used to locate all the extrema in the smoothed signal, and the locations are transformed back to the original signal domain.

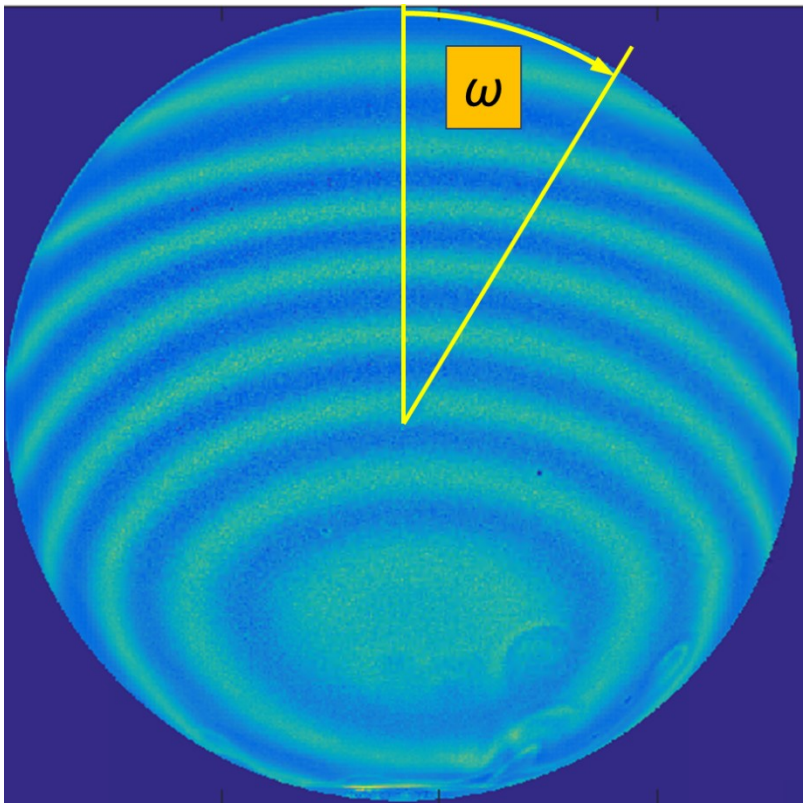

Figure 4-6: Locations of extracted light intensity from a treated image.

4.2.6 Calculation of film thickness: Application

This section describes the functions of the MATLAB scripts "a4_Extrema2String.m" and "a5_ThicknessProfileCalc.m", located in Appendix A along with applicable non-built-in functions called from within the scripts.

After extraction of the interference extrema, the three extrema patterns at each time-step were combined and converted to a character string, where a different ASCII character represents each light source maximum or minimum. The strings for each time-step were compared to that of the subsequent time-step by a pattern recognition technique called edit distance. The edit distance represents the minimum number of changes required to change one string into another, and more detail can be found in (Theodoridis, 2010). The edit distance was calculated at each location of the comparing string to determine the string component change from each time-step and whether any shift was

required to reflect that change. These cumulative shifts are illustrated in Figure 4-7 for time-steps 1 (at rupture) through 25.

```
 1                    RBIrbBiRbrIBbRiBrbIBRbirBbRIBrbiBRbIrBbiRBrbI
 2                    RIBrbiBRbrIBbRiBrbIBRbirBbRIBrbiBRbIrBibRBrIb
 3                     IBrbiBRbrIBbRiBrbIBRbirBbRIBrbiBRbIrBibRBrIb
 4                     IBrbiBRbrIBbRiBrbIBRbirBbRIBrbiBRbIrBibRBrIbB
 5                     IBrbiBRbrIBbRiBrbIBRbirBbRIBrbiBRbIrBibRBrIbBR
 6                     IBrbiBRbrIBbRiBrbIBRbirBbRIBrbiBRbIrBibRBrIbBR
 7                       rbiBRbrIBbRiBrbIBRbirBbRIBrbiBRbIrBibRBrIbBR
 8                       rbiBRbrIBbRiBrbIBRbirBbRIBrbiBRIbrBibRBrIbBR
 9                       rbiBRbIrBbRiBrbIBRbirBbRIBrbiBRIbrBibRBrIbBRi
10                       rbiBRbrIBbRiBrbIBRbirBbRIBrbiBRIbrBibRBrIbBRi
11                        biBRbIrBbRiBrbIBRbirBbRIBrbiBRIbrBibRBrIbBRib
12                        biBRbrIBbRiBrbIBRbirBbRIBrbiBRIbrBibRBrIbBRib
13                         iBRbrIBbRiBrbIBRbirBbRIBrbiBRIbrBibRBrIbBRib
14                         iBRbrIBbRiBrbIBRbirBbRIBrbiBRbIrBibRBrIbBRib
15                         iBRbrIBbRiBrbIBRbirBbRIBrbiBRbIrBbiRBrIbBRibr
16                          BRbrIBbRiBrbIBRbirBbRIBrbiBRIbrBibRBrIbBRibr
17                           RbrIBbRiBrbIBRbirBbRIBrbiBRbIrBibRBrIbBRibrB
18                           RbrIBbRiBrbIBRbirBbRIBribBRIbrBibRBrIbBRibrB
19                            brIBbRiBrbIBRbirBbRIBrbiBRbIrBibRBrIbBRibrB
20                            brIBbRiBrbIBRbirBbRIBrbiBRbIrBibRBrIbBRibrBI
21                            brIBbRiBrbIBRbirBbRIBrbiBRIbrBibRBrIbBRibrBI
22                            brIBRbiBrbIBRbirBbRIBrbiBRbIrBibRBrIbBRibrBI
23                             rIBbRiBrbIBRbirBbRIBrbiBRbIrBibRBrIbBRibrBIb
24                             rIBbRiBrbIBRbirBbRIBrbiBRIbrBibRBrIbBRibrBIbR
25                             IrBbRiBrbIBRbirBbRIBrbiBRIbrBibRBrIbBRibrBIbR
```

Figure 4-7: Example of the ASCII strings created in twenty-five time-steps to represent each light source fringe and be used in pattern recognition for identifying fringe orders.

Overlaying all strings from each time-step, a master string was produced from the mode of the characters in each column (Figure 4-8a & b). The master string is then compared by edit distance to a library string of known fringe orders (Figure 4-8c), to determine the location of best fit within the library, and thus, the order of the interference fringes. Finally, to ensure the removal of erroneous data points, the extrema type was compared to the library at every time-step, and any points which disagree with the library are removed (Figure 4-8d). A third array is created to mirror the input arrays, containing the film thickness at each non-deleted data point. The film thicknesses are extracted from the library.

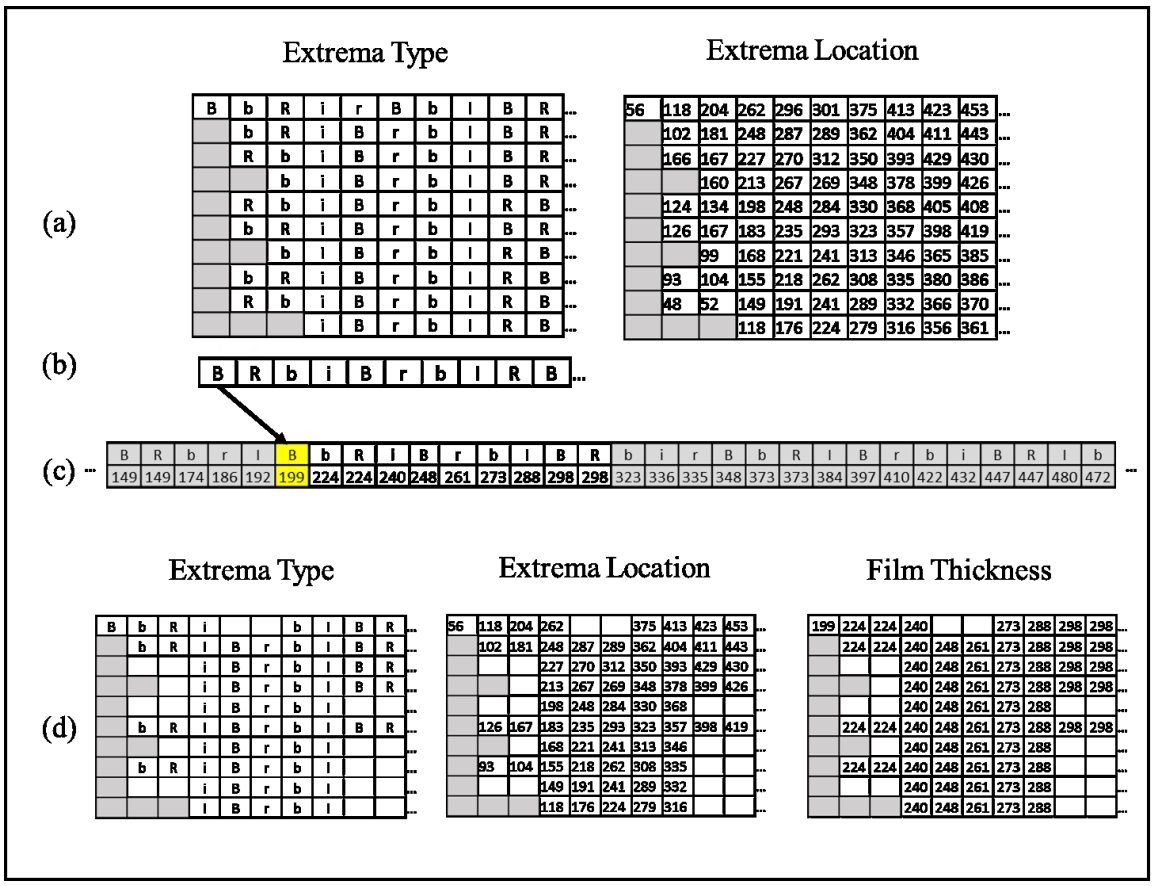

Figure 4-8: Determination of fringe order by pattern recognition, using partial matrices as example. Two arrays are input, containing: the ASCII characters to represent wavelength and type (maximum or minimum) of fringe, and the location of the fringe in 0.0005π radians from top of bubble (a). Master string is created from the mode of characters in each column (b). Master string is compared to library of known extrema to fringe orders (c). Extrema in original matrix which do not match the library string are removed, and a new array is created containing film thicknesses at all know extrema (d).

In eliminating extrema, which are not in agreement with the pattern of the library string, the risk is also run of eliminating extrema which display a twiddle circumstance. Twiddles may easily occur where two extrema calculate a similar thickness, so the pattern may sometimes show “Rb” or “bR”. This is not a concerning error, because by nature of the error, very similar film thicknesses would be calculated at each location. The manner in which the MATLAB script looks-up thickness values from the library does not easily accommodate these twiddles, and so they are deleted with any possibly erroneous data points. Valid data points may also be deleted by this method if they appear at the very top

of the bubble. An example of this occurrence is where a blue maximum, and then a red maximum are expected in the pattern, but the red maximum is not detected by the script. The blue maximum will then be shifted within the pattern at that time-step, appearing at the incorrect position, and be lost when the final extrema array is compared to the library. The MATLAB code could be improved here so that those extrema which are correct, but deleted due to the rigidity of this code would be kept. To quantify the loss of extrema, the ratio is taken of the data points after deletions and before. Plotted in Figure 4-9 are the frequency of ratios calculated for all the data reported in this manuscript. Much of the data produces a ratio close to 0.9, and 96% of all the data show a ratio greater than 0.8.

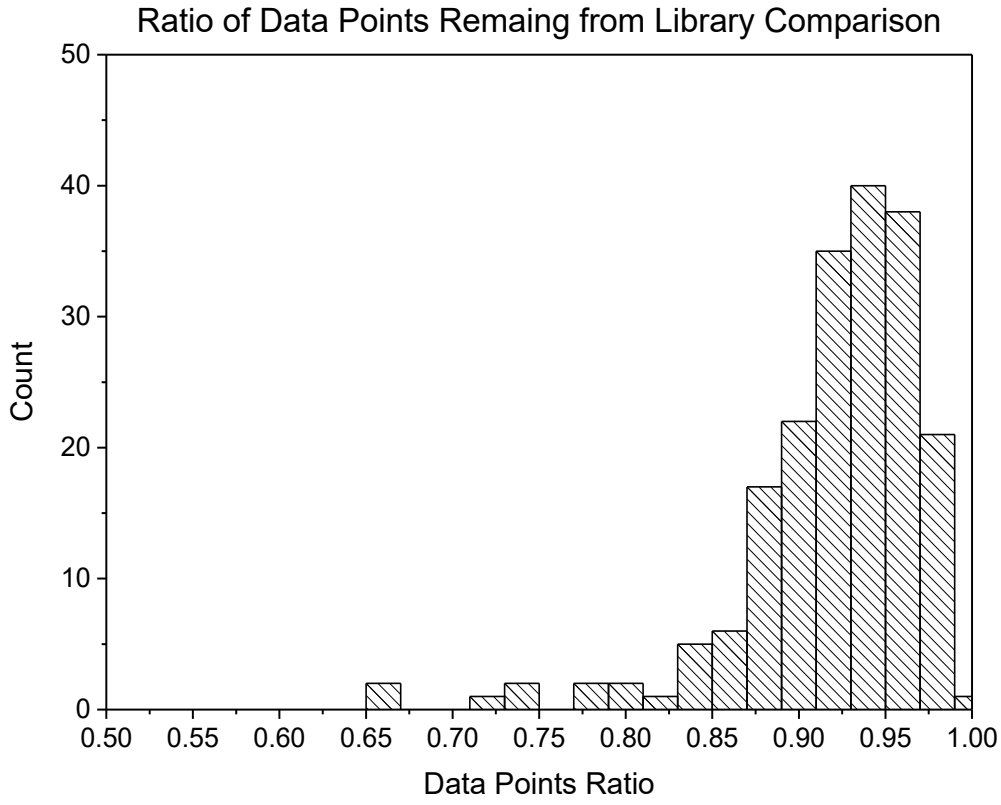

Figure 4-9: Distribution of the ratios of data point remaining after comparison to library for all trials studied.

This ratio, taken on both sides of the bubble is also used to determine the side from which data will be reported as results for the particular trial. In the case of marginal regeneration, or a speck of dust floating through the right side of the bubble, a very low ratio close to zero will be calculated, and a relatively high ratio should still be attained for the left side if it did not experience any physical impedances. In this case, the left side data would be used, as it obviously presents the clearest image.

The library string was generated by the same process as above, from trials which were observed to have achieved a Newton Back Film. Additional trials which produced very clear interference fringe patterns, did not reach a Newton Black Film, but did overlap significantly with the library data, were used to further extend the library.

4.3 Results & Discussion

4.3.1 Growth of a Foam Cell

To enlighten the extent to which coarsening plays a role in the different foam heights observed in Section 3.3.1, the growth of a single foam cell was followed through its lifetime. Figure 4-10 depicts seven frames from this video with the traced cell highlighted in yellow. It can be seen at the end of lifetime, it is the largest cell in frame.

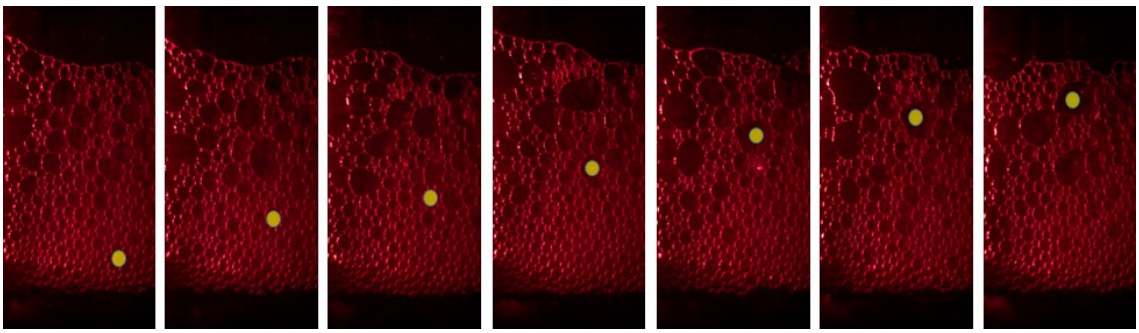

Figure 4-10: Growth of a foam cell as it rises upward in PNIPAM experiment at 40 °C.

To see how the cell grows, its projected area was measured at every frame of the video, the results of which are plotted in Figure 4-11. The times at which this cell coalesced with another are highlighted in red. The lifetime of this foam cell from joining the bottom of the foam phase to coalescence with the atmosphere was less than 8 s. All

major increases in cell size coincide with a coalescence event – indicating that coalescence, and not coarsening, is the dominant mechanism at play in determining the foam stability of this system.

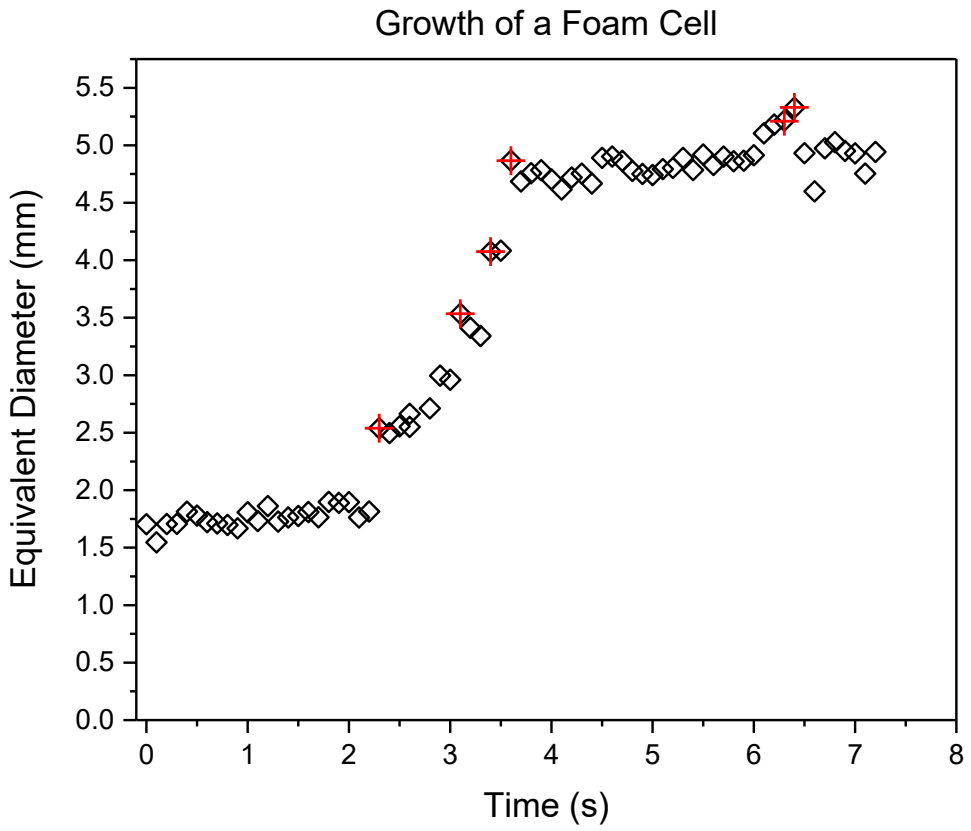

Figure 4-11: Size of a single foam cell through its lifetime. The cell studied is the same one shown in Figure 4-10. Coalescence events are marked with a red cross.

4.3.2 Fitting the Drainage Profile Surface

With the film thicknesses known at the valid extrema positions on the bubble, and at every time-step, a polynomial surface was fit in MATLAB to determine the change in film thickness at every position, and through the entire lifetime of the bubble. Goodness of fit was evaluated using the sum of squares due to error, R-square, and root mean square error; along with visual inspection of the surface (example shown in Figure 4-12) and residual plots (example shown in Figure 4-13).

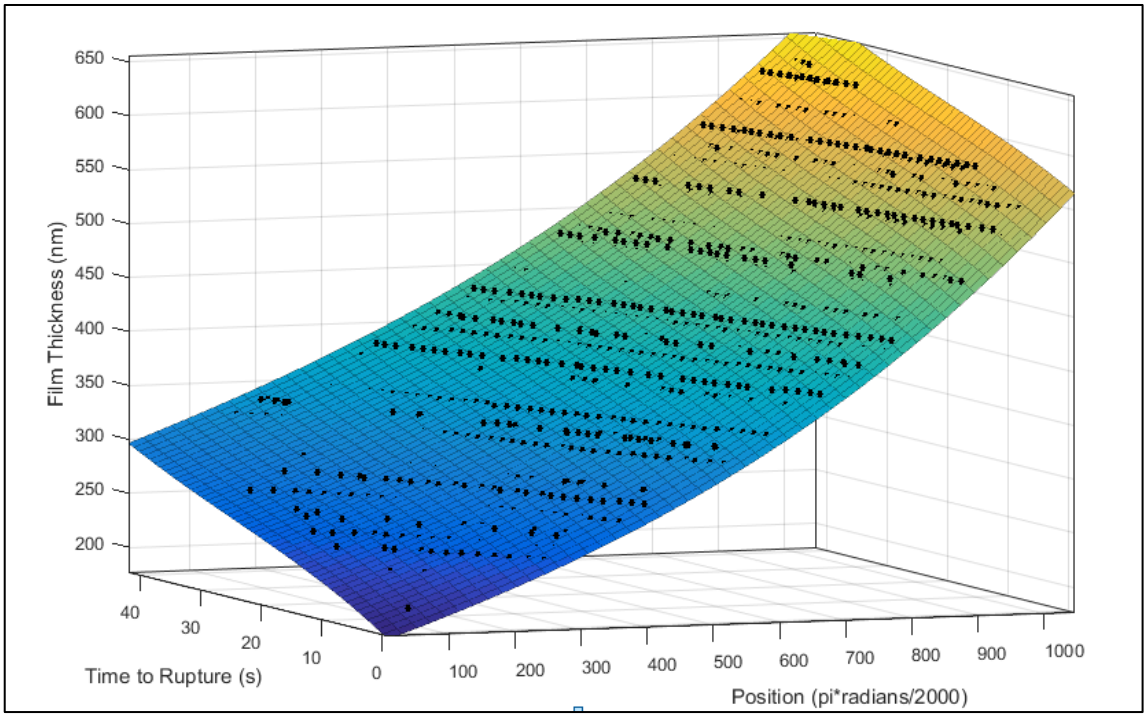

Figure 4-12: Surface plot of a draining bubble. The z-axis denotes the film thickness at any given location on the bubble (x-axis) and time (y-axis).

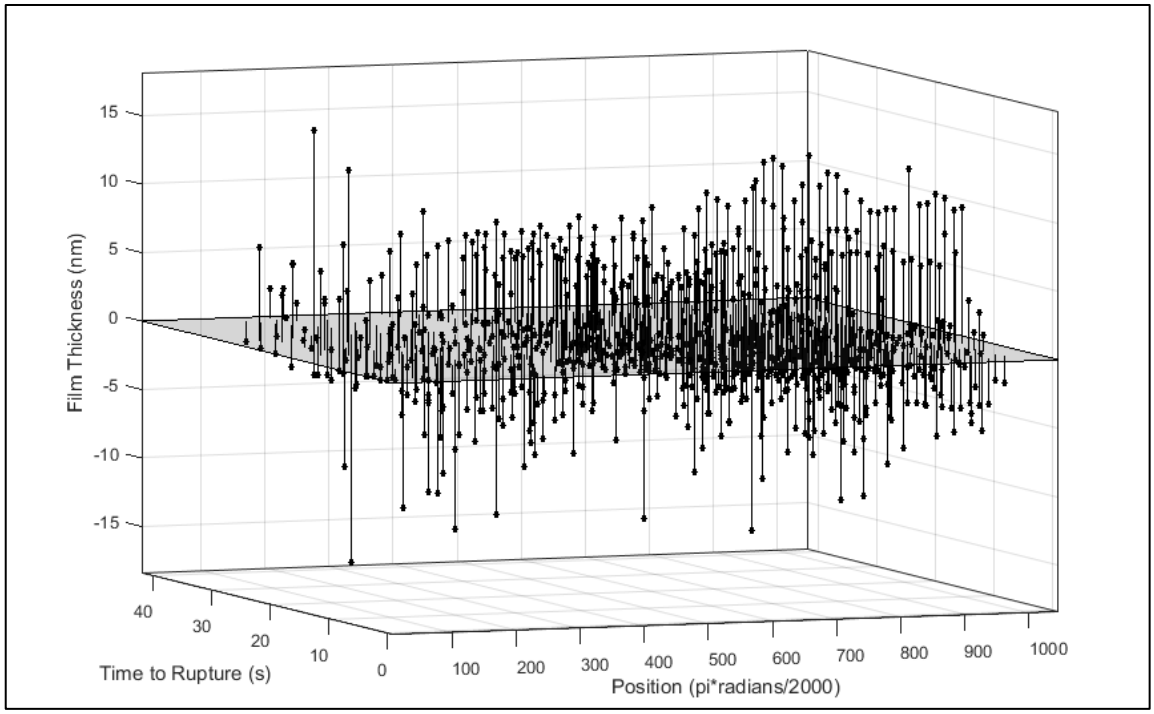

Figure 4-13: Plot of residuals from fitting the surface shown in Figure 4-12: Surface plot of a draining bubble. The z-axis denotes the film thickness at any given location on the bubble (x-axis) and time (y-axis).

Overall, a first-degree polynomial fit was chosen for the time axis, and a third-degree polynomial fit was chosen in the spatial axis. Comparing Table 4-1, representing the entire lifetime of a bubble, and Table 4-2, representing only the last 8 seconds of bubble lifetime, the R-squared value is not greatly improved by making this change. Visually, the residual plots for a first-degree polynomial appear to represent a more random error though, rather than a systematically patterned error which is indicative of inappropriate fitting parameters, so the first-degree polynomial fit was selected over higher degrees.

Table 4-1: Goodness of fit statistics for the drainage profile surface of a PNIPAM bubble, lasting 46.6 seconds. The rows and columns represent the degree of polynomial used to fit in each axis (time and position).

		R-Squared			Sum of Squares Due to Error			Root Mean Square Error		
		Time			Time			Time		
		1	2	3	1	2	3	1	2	3
Position	1	0.9941	0.9958	0.9959	1.46E+06	1.03E+06	1.01E+06	16.19	13.60	13.46
	2	0.9967	0.9983	0.9985	8.13E+05	4.17E+05	3.78E+05	12.08	8.65	8.24
	3	0.9968	0.9984	0.9985	7.86E+05	3.89E+05	3.63E+05	11.88	8.36	8.08

Table 4-2: Goodness of fit statistics for the drainage profile surface taken from the final 8 seconds only of a PNIPAM bubble (the same bubble trial as Table 4-1). The rows and columns represent the degree of polynomial used to fit in each axis (time and position).

		R-Squared			Sum of Squares Due to Error			Root Mean Square Error		
		Time			Time			Time		
		1	2	3	1	2	3	1	2	3
Position	1	0.9841	0.9841	0.9845	1.51E+05	1.50E+05	1.47E+05	13.18	13.17	13.04
	2	0.9980	0.9980	0.9981	1.86E+04	1.86E+04	1.77E+04	4.64	4.64	4.53
	3	0.9982	0.9982	0.9983	1.73E+04	1.72E+04	1.64E+04	4.48	4.46	4.37

From the surface generated here, the thickness and rate of change can be extracted for any time and location on the top hemisphere of the bubble.

4.3.3 Drainage of PNIPAM-stabilized bubble

With the fitted surface to describe the bubble film thickness, rate of change can be extracted directly from the slope in the time axis at any desired point on the bubble. Since the time axis was fitted with a first order polynomial, the rate of film thinning is equal at all locations studied (top hemisphere of the bubble). Figure 4-14 plots the measured change in thickness as a function of PNIPAM concentration. There is a very clear distinction between the low temperature and high temperature experiments, where the 40 °C trials drain at a rate approximately 2.2 times more rapidly than the 20 °C trials. This is in agreement with the foamability experiments described in Section 3.3.1. It also follows

the assertion in Section 4.3.1 that the tuning of PNIPAM foam is due to a change in the film drainage and rupture – not foam coarsening.

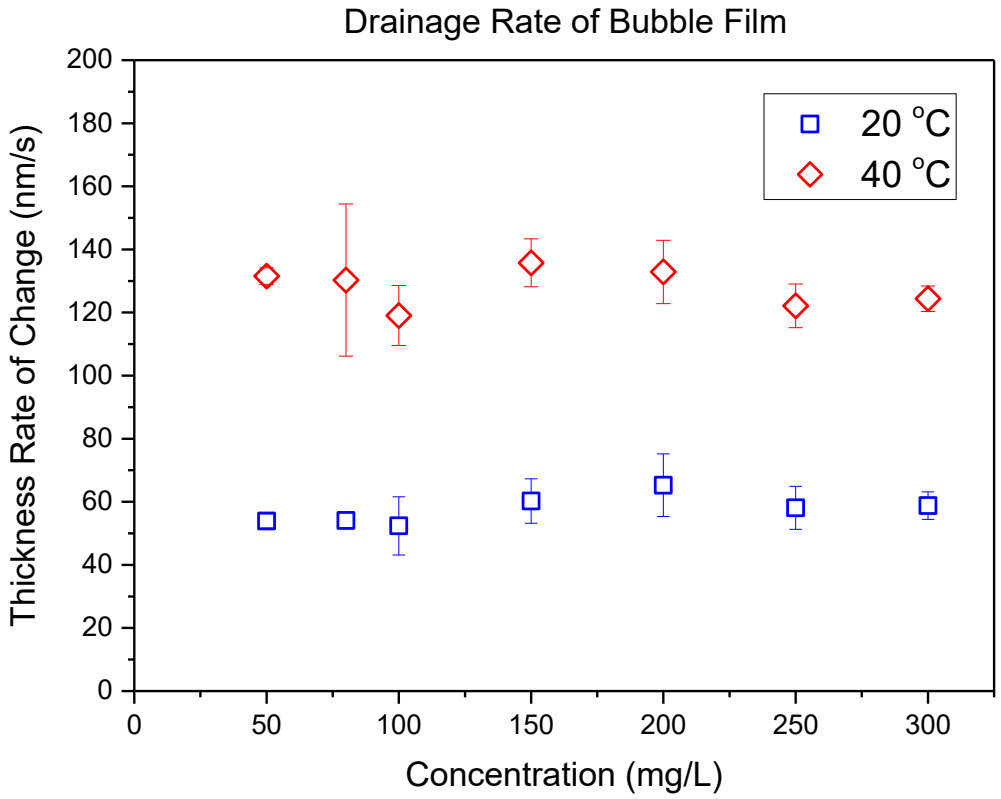

Figure 4-14: Rate of change in film thickness of a PNIPAM-stabilized bubble at 20 °C (blue squares) and 40 °C (red diamonds).

While there is still debate of the proportional contributions of surface rheological properties to thin-film drainage, many models for the drainage of thin liquid film make an account for surface elasticity or viscosity to form the boundary conditions at the interfaces (Champougny et al., 2015; Seiwert et al., 2013; Van Nierop et al., 2008). It is unlikely that the shear rheology is the dominant property in changing the flow, as the shear modulus has been shown to measure much lower than the surface modulus.

While a conclusion on the boundary condition cannot be drawn from this work, it is generally agreed that the no-slip condition of Poiseuille flow is inappropriate for

surfactant-stabilized films (Weaire and Hutzler, 2001), and all other properties used to describe the interface have not presented a transition about the LCST.

4.3.4 Determination of Rupture Thickness

Determination of the rupture thickness was done by extrapolation from the surfaces fit in Section 4.3.2. Three methods were compared to determine the most reliable and accurate method:

1. The value at the top of the bubble ($\omega \sim 0$), and time of rupture ($t \sim 0$) is extracted directly from the fitted surface.
2. The rupture thickness is approximated as the thickness denoted by the closest known point at the time of rupture. This corresponds to the interference fringe closest to $\omega=0$ at time of rupture.
3. The last two points (two fringes closest to top of bubble) at the time of rupture are used to extrapolate the film thickness.

The three methods are compared in Figure 4-15. In each of the cases studied (maximum value in dataset, minimum value, and average value), methods 1 and 2 give similar results. Method 3 shows the most deviation from the other two. For example, in Figure 4-15a, at concentration of 80 mg/L and temperature of 40 °C, method 3 deviates by nearly 1000 nm. Intuitively, this method would be the least reliable, as it relies on extrapolation by only two points. Furthermore, these two points may be far from the surface origin compared to other points.

Methods 1 and 2 are quite similar, where method 2 is the conservative value, because it represents a known data point. These data points fall near the top of the bubble, but the exact location varies – due to the elimination step discussed in Section 4.2.6, which makes it more difficult to compare entire datasets, as there is variability introduced that is difficult to predict. Method 1 is the ideal method, as it makes use of the surface which was fit to the entire data set, leading to a more reliable extrapolation – provided the fit is correct. Noting that methods 1 and 2 fall close in all cases, and method 1 consistently

gives a slightly lower value than method 2, it is concluded that the extrapolation of method 1 is most appropriate, and has been used for report the film thicknesses here.

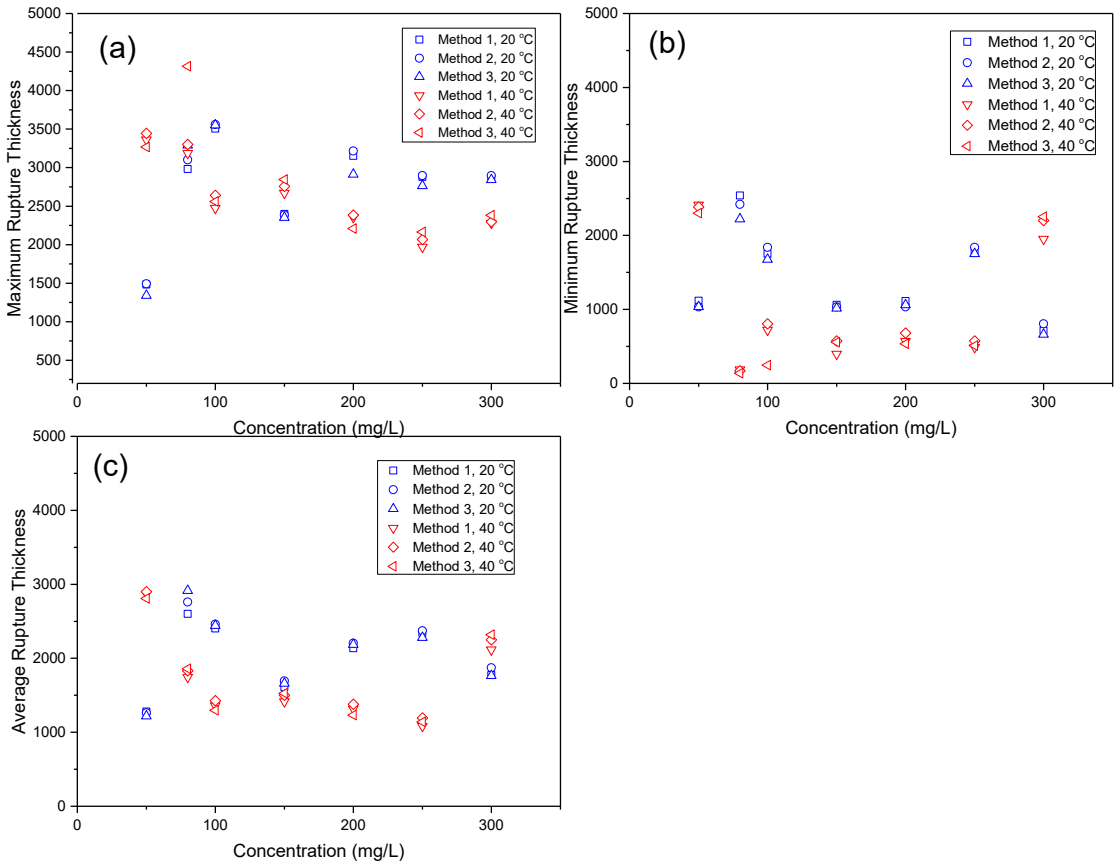

Figure 4-15: Comparison of methods for determination of film thickness at rupture, using maximum value (a), minimum value (b), and average value (c).

The rupture thickness results in Figure 4-16 do not seem to show a discernable trend that is specific to the different temperatures. These experiments have also given relatively wide standards of deviation. While a very pronounced effect of temperature has been observed for the drainage of PNIPAM-stabilized bubbles, the same cannot be said for rupture thickness. While precautions were taken to limit air-flow in the vicinity of experimental bubbles and keep the area clean, it is possible that air movement and impurities on some samples may have contributed to this wide and delineated distribution of rupture thicknesses.

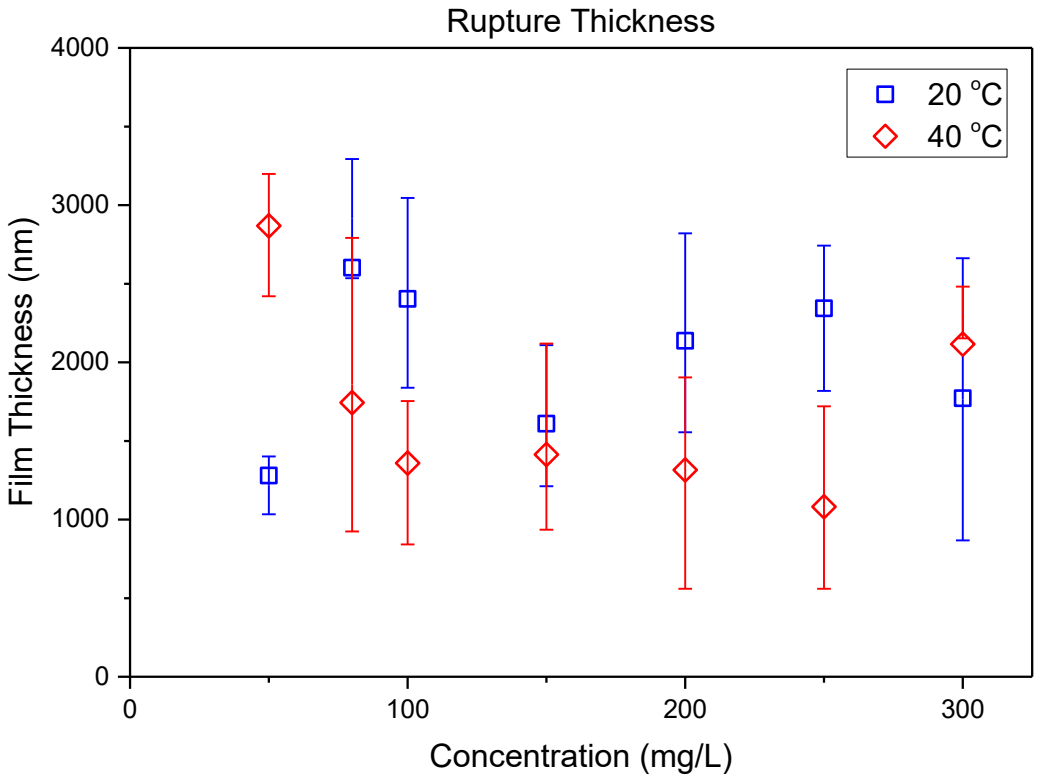

Figure 4-16: Film thickness at time of rupture for PNIPAM-stabilized bubble at 20 °C (blue squares) and 40 °C (red diamonds).

In general, rupture thicknesses here were much greater than the thickness of stable films measured by Jean et al. (2009). The previously discussed possibility for premature rupture aside, some major differences exist. Jean et al. (2009) attributes the large stable film thicknesses to steric repulsion of the polymer chains at each interface. The molecular weights of polymers in that study were one and two orders of magnitude larger than in this work. Secondly, using the thin film pressure balance in their study, also allowed control of the drainage, whereas this study focused on gravity-driven drainage. Thirdly, their study covered a range of temperatures from 24 °C to 27°C, which are still well below the LCST, and this study focused only on one temperature below LCST (20 °C), and one above (37 °C in some experiments, and 40 °C in others). With those points made, these two works do not disagree, as the work presented here does not give any evidence for the behaviour of PNIPAM aqueous films between the temperatures studied.

Chapter 5: Conclusions

In this work, PNIPAM has been shown to stabilize tunable aqueous foam. Below LCST, PNIPAM aqueous solution generates foam well. Above LCST, the foam is far less stable, barely producing a layer of bubbles at most concentrations studied hear (3 – 100 mg/L). This tuning characteristic shows promise for PNIPAM, or a similar stimuli-responsive polymer to be used as a tunable frother in mineral flotation, where fine particles can contribute to overly-stable froths that many operations are not equipped to deal with.

To uncover the property responsible for the characteristic of tunable foam, the adsorption and adsorption rate in a bubbling column as well as dynamic tensiometer were investigated. Both above and below LCST, PNIPAM adsorbed readily, and there appeared no significant difference with temperature.

Knowing there were similar quantities of surfactant present at the interface in both cases, the mechanisms for foam collapse were reviewed. It was determined that coarsening was not the responsible mechanism, but coalescence was.

To investigate coalescence in decreasing foam stability, a new interferometry technique was developed which made use of three wavelengths of light so that absolute film thickness could be determined with the requirement of the film thinning to near-Newton black film thicknesses. The code for image analysis of three-wavelength images was written in MATLAB. A special programming method used here was the pattern recognition to determine the absolute thickness profile by comparing character strings generated by the image analysis for each trial to a database string of characters associated with known film thicknesses.

In the study of PNIPAM aqueous foams with this new technique, a significant and repeatable increase in drainage rate was found at 40 °C compared to 20 °C. The change in drainage rate must be the mechanism for decreased foam stability observed above LCST. A possible cause is a changing boundary condition for the flow of liquid within the thin film due to changing surface rheology about the LCST; however, there is still much

debate around the definitions of surface rheology and the role(s) played in thin film drainage regulation.

5.1 Contributions to Original Knowledge

Recently, others have produced many stimuli-responsive foams, as outlined by Fameau et al. (2015). Here, it is the first time PNIPAM has been shown as a tool for tuning foam. Investigation of the thin-film free drainage has elucidated the change in drainage rate about the LCST, which contributes to the tunable foam stability.

A new interferometry technique was developed, using three light sources of different wavelengths. This method removes the disadvantage of a single light source, where a Newton black film must be achieved to certainly determine the order of interference fringes detected. This method also provides a clarity of interference patterns with only three narrow spectrums to study, rather than competition of the entire visible spectrum to be detected by a standard RGB CCD camera, as in white light interferometry.

5.2 Future Work

Future work might include development of a drainage model to explain the results found here for a PNIPAM-stabilized bubble. When an appropriate model is constructed, then the surface rheological parameters might be extracted from the experimental data collected here. This single draining bubble film measurement tool could then be used to measure surface rheological properties, as has been done by Sett et al. (2013).

For PNIPAM as a thermo-responsive frother, trials should be done with solids introduced to the system to evaluate the combined effect on froth stability; and further on, PNIPAM could be tested in a laboratory-scale flotation column with genuine ore and typical reagents to evaluate compatibility. Given that PNIPAM interacts more readily with water molecules below its LCST, a possible drawback of PNIPAM as a frother is that it may deter hydrophobic mineral particles from the air-water interface of bubbles – reducing recovery overall. Additionally, the promotion of froth stability by fine particles that partially-wet, and prevent the coalescence of froth cells may be too great to be

overcome by PNIPAM. Possible impedances are: competition for the air-water interface between PNIPAM molecules and the mineral particles; or the size of mineral particles being too great compared to the films stabilized in this work (less than 5 μm), that the PNIPAM cannot alter the drainage of a thin film that is maintained by particles in the range of 10 μm. There are numerous possible interactions between PNIPAM, thin liquid films, and mineral particles.

It should be noted that only PNIPAM was studied here for the purpose of a responsive frother. There may be a more suitable responsive polymer, or a fit-for-purpose polymer may be designed for frothing. This area will benefit from the increased understanding of the role of surface viscoelasticities in stabilizing foam and froth. Linking the changes of PNIPAM at the molecular level to the changes in foam stability will pave the way for identification of the optimal polymer for controlling a stimuli-responsive froth.

References

Afanasyev, Y.D., Andrews, G.T., Deacon, C.G., 2011. Measuring soap bubble thickness with color matching. Am. J. Phys. 79, 1079.

Ahmed, Z., Gooding, E. a, Pimenov, K. V, Wang, L., Asher, S. a, 2009. UV resonance Raman determination of molecular mechanism of poly(N-isopropylacrylamide) volume phase transition. J. Phys. Chem. B 113, 4248–56.

Aktas, Z., Cilliers, J.J., Banford, A.W., 2008. Dynamic froth stability: Particle size, airflow rate and conditioning time effects. Int. J. Miner. Process. 87, 65–71.

Alargova, R.G., Warhadpande, D.S., Paunov, V.N., Velev, O.D., 2004. Foam superstabilization by polymer microrods. Langmuir 20, 10371–10374.

Bethell, P.J., Arnold, B.J., Klima, M.S., 2012. Challenges in Fine Coal Processing, Dewatering, and Disposal. SME.

Bethell, P.J., Luttrell, G.H., 2005. Effects of Ultrafine Desliming on Coal Flotation Circuits, in: Proceedings, Centenary of Flotation Symposium. Brisbane, Australia, pp. 719–728.

Bhamla, M.S., Giacomin, C.E., Balemans, C., Fuller, G.G., 2014. Influence of interfacial rheology on drainage from curved surfaces. Soft Matter 10.

Bikerman, J.J., 1973. Foams, Applied physics and engineering: 10. New York, Springer, 1973.

Brooks, C.F., Fuller, G.G., Frank, C.W., Robertson, C.R., 1999. An Interfacial Stress Rheometer to Study Rheological Transitions in Monolayers at the Air - Water Interface. Langmuir 15, 2450–2459.

Burdukova, E., Li, H., Bradshaw, D.J., Franks, G. V, 2010. Poly (N-isopropylacrylamide) (PNIPAM) as a flotation collector : Effect of temperature and molecular weight. Miner. Eng. 23, 921–927.

Butt, H.-J., Graf, K., Kappl, M., 2003. Physics and Chemistry of Interfaces, Wiley-VCH GmbH & Co. KGaA. WILEY-VCH GmbH & Co. KGaA, Weinheim.

Caps, H., Delon, G., Vandewalle, N., Guillermic, R.M., Pitois, O., Biance, A.L., Saulnier, L., Yazhgur, P., Rio, E., Salonen, A., Langevin, D., 2014. Does water foam exist in microgravity? Europhys. News 45, 22–25.

Champougny, L., Scheid, B., Restagno, F., Vermant, J., Rio, E., 2015. Surfactant-induced rigidity of interfaces: a unified approach to free and dip-coated films. Soft Matter 11, 2758–2770.

Chan, D.Y.C., Klaseboer, E., Manica, R., 2011. Theory of non-equilibrium force measurements involving deformable drops and bubbles. Adv. Colloid Interface Sci. 165, 70–90.

Couder, Y., Chomaz, J.M., Rabaud, M., 1989. On the Hydrodynamics of Soap Films. Phys. D 37, 384–405.

Craig, V.S.J., Ninham, B.W., Pashley, R.M., 1993. The effect of electrolytes on bubble coalescence in water. J. Phys. Chem. 97, 10192–10197.

Drenckhan, W., Saint-Jalmes, A., 2015. The science of foaming. Adv. Colloid Interface Sci. 222, 228–259.

Eastoe, J., Dalton, J.S., 2000. Dynamic surface tension and adsorption mechanisms of surfactants at the air-water interface. Adv. Colloid Interface Sci. 85, 103–144.

Exerowa, D., Kruglyakov, P.M., 1998. Foam and Foam Films: Theory, Experiment, Application. Elsevier Science, Amsterdam.

Fameau, A.-L., Carl, A., Saint-Jalmes, A., von Klitzing, R., 2015. Responsive Aqueous Foams. ChemPhysChem 16, 66–75.

Finch, J.A., Dobby, G.S., 1990. Column Flotation. Pergamon Press, Oxford, England.

Finch, J., Tan, Y.H., 2016. What Have We Learned About Frothers?, in: XXVIII

International Mineral Processing Congress. Quebec City, Canada.

Floriano, M.A., Angell, C.A., 1990. Surface Tension and Molar Surface Free Energy and Entropy of Water to -27.2 °C. J. Phys. Chem. 94, 4199–4202.

Franks, G. V., Li, H., O'Shea, J.P., Qiao, G.G., 2009. Temperature responsive polymers as multiple function reagents in mineral processing. Adv. Powder Technol. 20, 273–279.

Frostad, J.M., Tammaro, D., Santollani, L., Bochner de Araujo, S., Fuller, G.G., 2016. Dynamic fluid-film interferometry as a predictor of bulk foam properties. Soft Matter 12, 9266–9279.

Fuerstenau, M.C., Han, K.N., 2009. Introduction, in: Fuerstenau, M.C., Han, K.N. (Eds.), Principles of Mineral Processing. Society for Mining, Metallurgy, and Exploration, Inc., Littleton, CO, USA, pp. 1–8.

Fuerstenau, M.C., Somasundaran, P., 2009. Flotation, in: Fuerstenau, M.C., Han, K.N. (Eds.), Principles of Mineral Processing. Society for Mining, Metallurgy, and Exploration, Inc., Littleton, CO, USA, pp. 245–306.

Gilcreest, V.P., Dawson, K.A., Gorelov, A. V., 2006. Adsorption kinetics of NIPAM-based polymers at the air-water interface as studied by pendant drop and bubble tensiometry. J. Phys. Chem. B 110, 21903–21910.

Green Mining Initiative, 2016. . Nat. Resour. Canada. URL http://www.nrcan.gc.ca/mining-materials/green-mining/8178 (accessed 1.7.17).

Guillermic, R., 2011. Propriétés physico-chimiques des mousses: études approfondies sur des mousses modèles at études exploratoires sur de nouvelles mousses. Université Rennes.

Guillermic, R.-M., Saint-Jalmes, A., 2013. Dynamics of poly-nipam chains in competition with surfactants at liquid interfaces: from thermoresponsive interfacial rheology to foams. Soft Matter 9, 1344–1353.

Horozov, T.S., 2008. Foams and foam films stabilised by solid particles. Curr. Opin. Colloid Interface Sci. 13, 134–140.

Jean, B., Lee, L.T., Cabane, B., Bergeron, V., Andreatta, G., Lee, L.T., Lee, F.K., Benattar, J.J., Breward, C.J.W., Howell, P.D., 2009. Foam films from thermosensitive PNIPAM and SDS solutions. Langmuir 25, 3966–3971.

Koehler, S.A., Hilgenfeldt, S., Stone, H.A., 2000. Generalized view of foam drainage: Experiment and theory. Langmuir 16, 6327–6341.

Kruss, n.d. Du Noüy ring method. URL https://www.kruss.de/services/education-theory/glossary/du-nouey-ring-method/ (accessed 1.1.17).

Langevin, D., 2014. Surface shear rheology of monolayers at the surface of water. Adv. Colloid Interface Sci. 207, 121–130.

Langevin, D., 2002. Foams, Foam Films, and Monolayers, in: Shah, D.O., Mittal, K.L. (Eds.), Adsorption and Aggregation of Surfactants in Solution. CRC Press, pp. 453–464.

Lee, L.T., Jean, B., Menelle, A., 1999. Effect of Temperature on the Adsorption of Poly(N -isopropylacrylamide) at the Air−Solution Interface. Langmuir 15, 3267–3272.

Lhuissier, H., Villermaux, E., 2012. Bursting bubble aerosols. J. Fluid Mech. 696, 5–44.

Magrabi, S.A., Dlugogorski, B.Z., Jameson, G.J., 1999. Bubble size distribution and coarsening of aqueous foams. Chem. Eng. Sci. 54, 4007–4022.

Marshall, B., 2015. Facts and figures of the Canadian mining industry: F&F 2015, Mining Association of Canada. Ottawa.

Monteux, C., Mangeret, R., Laibe, G., Freyssingeas, E., Bergeron, V., Fuller, G., 2006. Shear surface rheology of poly(N-isopropylacrylamide) adsorbed layers at the air-water interface. Macromolecules 39, 3408–3414.

Myrvold, R., Hansen, F., 1998. Surface Elasticity and Viscosity from Oscillating Bubbles

Measured by Automatic Axisymmetric Drop Shape Analysis. J. Colloid Interface Sci. 207, 97–105.

Nedyalkov, M., Alexandrova, L., Platikanov, D., Levecke, B., Tadros, T., 2007. Wetting films on a hydrophilic silica surface obtained from aqueous solutions of hydrophobically modified inulin polymeric surfactant. Colloid Polym. Sci. 285, 1713–1717.

Noskov, B.A., Akentiev, A. V, Bilibin, A.Y., Grigoriev, D.O., Loglio, G., Zorin, I.M., Miller, R., 2004. Dynamic Surface Properties of Poly (N -isopropylacrylamide) Solutions. Langmuir 20, 9669–9676.

Pelton, R., 2010. Poly (N-isopropylacrylamide) (PNIPAM) is never hydrophobic. J. Colloid Interface Sci. 348, 673–674.

Prins, A., 2015. Foaming Behavior of Liquids: Surface Forces' Role, in: Encyclopedia of Surface and Colloid Science, Third Edition. CRC Press, pp. 2826–2836.

Ramon, O.R.Y., Kesselman, E., Berkovici, R., Cohen, Y., Paz, Y., 2001. Attenuated Total Reflectance / Fourier Transform Infrared Studies on the Phase-Separation Process of Aqueous Solutions of Poly (N-isopropylacrylamide). J. Polym. Sci. Part B - Polym. Phys. 39, 1665–1677.

Ravera, F., Loglio, G., Kovalchuk, V.I., 2010. Interfacial dilational rheology by oscillating bubble / drop methods. Curr. Opin. Colloid Interface Sci. 15, 217–228.

Real gross domestic product, expenditure-based, by province and territory, 2016. . Stat. Canada. URL http://www.statcan.gc.ca/tables-tableaux/sum-som/l01/cst01/econ50-eng.htm (accessed 1.7.17).

Sagis, L.M.C., 2011. Dynamic properties of interfaces in soft matter: Experiments and theory. Rev. Mod. Phys. 83, 1367–1403.

Saint-Jalmes, A., 2006. Physical chemistry in foam drainage and coarsening. Soft Matter 2, 836.

Saulnier, L., Boos, J., Stubenrauch, C., Rio, E., 2014. Soft Matter single vertical films – single and mixed surfactant. Soft Matter 10, 5280–5288.

Scarpa, J.S., Mueller, D.D., Klotz, I.M., 1967. Slow hydrogen-deuterium exchange in a non-.alpha.-helical polyamide. J. Am. Chem. Soc. 89, 6024–6030.

Scheludko, a., 1967. Thin Liquid Films. Adv. Colloid Interface Sci. 450, 391–464.

Schild, H.G., 1992. Poly (N-Isopropylacrylamide): Experiment , Theory and Application. Prog. Polym. Sci. 17, 163–249.

Schneider, C. a, Rasband, W.S., Eliceiri, K.W., 2012. NIH Image to ImageJ: 25 years of image analysis. Nat. Methods 9, 671–675.

Seiwert, J., Dollet, B., Cantat, I., 2013. Theoretical study of the generation of soap films: role of interfacial visco-elasticity. J. Fluid Mech. 739, 124–142.

Sett, S., Sinha-Ray, S., Yarin, A.L., 2013. Gravitational drainage of foam films. Langmuir 29, 4934–4947.

Shi, C., Cui, X., Xie, L., Liu, Q., Chan, D.Y.C., Israelachvili, J.N., Zeng, H., 2015. Measuring forces and spatiotemporal evolution of thin water films between an air bubble and solid surfaces of different hydrophobicity. ACS Nano 9, 95–104.

Theodoridis, S., 2010. Template Matching, in: Introduction to Pattern Recognition: A Matlab Approach. Elsevier, Amsterdam, pp. 481–519.

Van Nierop, E. a., Scheid, B., Stone, H. a., 2008. On the thickness of soap films: an alternative to Frankel's law. J. Fluid Mech. 602, 1–9.

Vandebril, S., Franck, A., Fuller, G.G., Moldenaers, P., Vermant, J., 2010. A double wall-ring geometry for interfacial shear rheometry. Rheol. Acta 49, 131–144.

Wang, J., Nguyen, A. V., Farrokhpay, S., 2016. A critical review of the growth, drainage and collapse of foams. Adv. Colloid Interface Sci. 228, 55–70.

Weaire, D., Hutzler, S., 2001. The Physics of Foams. Oxford University Press, Oxford.

Weaire, D., Phelan, R., Gabbrielli, R., 1994. A counter-example to Kelvin's conjecture on minimal surfaces. Philos. Mag. Lett. 89, 483–491.

Yaws, C.L., 2003. Yaws' Handbook of Thermodynamic and Physical Properties of Chemical Compounds : Physical, Thermodynamic and Transport Properties for 5,000 Organic Chemical Compounds. Knovel, Norwich, NY.

Yokoi, K., Kawaguchi, M., 2014. Effect of temperature on surface pressure-area isotherms and surface dilational moduli of poly(N-isopropyl acrylamide) monolayers spread at air-water interface. Colloids Surfaces A Physicochem. Eng. Asp. 457, 469–475.

Appendices

Appendix A: Image analysis code (MATLAB)

A1 ExtractExtrema.m

```
%%%% a3_ExtractExtrema.m
%%%% Extraction of interference fringes from treated images of bubbles
%%%% INPUT: IMAGES FROM VIDEO, TREATED IN STEP A2
%%%%    1. LOOP TO EXTRACT INTENSITY CURVES AT EACH TIME-STEP
%%%%    2. TRANSFORM TIME DOMAIN OF FRINGES AND DETECT EXTREMA
%%%%        a. FAST-FOURIER TRANSFORM TO DETERMINE DOMINANT FREQUENCIES
%%%%        b. RATIO OF FREQUENCIES AT TOP AND BOTTOM USED TO TRANSFORM
%%%%        SIGNAL (I.E. LENGTHEN HIGH FREQUENCY END OF SIGNAL
%%%%        c. TRANSFORMED SIGNAL IS MORE EFFECTIVELY SMOOTHED BY
%%%%        BUTTERWORTH FILTER
%%%%        d. MAX AND MIN (PEAKS AND VALLEYS) OF TRANSFORMED SIGNAL ARE
%%%%        IDENTIFIED
%%%%        e. MAX AND MIN TRANSFORMED BACK TO DOMAIN OF ORIGINAL
%%%%        SIGNAL
%%%%    3. PLOT INTENSITY PROFILES AND SAVE TO VIDEO
%%%% OUTPUT: LOCATION, INTENSITY, AND ASCII CHAR VECTOR FOR EACH COLOUR AT
%%%%         EACH TIME-STEP

%%-------------------------------------------------------------------------
        clear
        close all
        filename = '160606-001'; %Filename of trial
        load(sprintf('..\\a2_PRETREAT\\%s_PRETREAT',filename)); %Load treated images


%% 0. PREALLOCATION AND DEFINING PROPERTIES
%%%%PROPERTIES OF THE ANALYSIS CODE
```

```
%%%% INPUT VARIABLES
B = a2_results.B; %Image from Blue Light
R = a2_results.R; %Image from Red Light
IR = a2_results.IR; %Image from Infrared Light
R0_b = a2_results.R0_b; %Radii of bubble in B
R0_r = a2_results.R0_r; %Radii of bubble in R
R0_ir = a2_results.R0_ir; %Radii of bubble in IR
Origin = a2_results.Origin; %Coordinates of Bubble Center
a2_results.Nb_im; %Number of images

%%%% PROPERTIES OF THE ANALYSIS CODE
Nb_lin = anlys_props.Nb_lin;        % number of pathlines to be studied
phi_max = anlys_props.phi_max;      % Pathline limit (in radians)
Nb_phi = anlys_props.Nb_phi;        % Number of points in pathline
a = anlys_props.a;                  % number of pixels subtracted from R0
sq = anlys_props.sq;                % Size of blurring matrix
order_lo = anlys_props.order_lo;    % Order of Butterworth filter

%%%% PARAMETERS OF COORDINATES OF PATHLINES
theta=linspace(-pi/2,pi/2,Nb_lin);
phi=linspace(0,phi_max,Nb_phi);     %Pathline
psi1=atan(repmat(tan(phi),Nb_lin,1)./repmat(sin(theta)',1,Nb_phi)); %Phase only between -pi/2 and pi/2
phase_corr = [zeros(2,1000),[-pi*ones(1,500);pi*ones(1,500)]]; %Correction for phase
psi = psi1+phase_corr;
R_b = R0_b-a;
R_r = R0_r-a;
R_ir = R0_ir-a;

%%%% PREALLOCATION
I_blue = zeros(Nb_lin,Nb_phi,Nb_im);
I_red = zeros(Nb_lin,Nb_phi,Nb_im);
I_ir = zeros(Nb_lin,Nb_phi,Nb_im);

Freq_top = zeros(Nb_im,Nb_lin);
Freq_bot = zeros(Nb_im,Nb_lin);
```

```
%% 1. LOOP TO EXTRACT INTENSITY CURVES AT EACH TIME-STEP, tt
    %%%% FIRST POINT IS AT TOP OF THE BUBBLE
    %%%% LAST POINT IS AT phi_max (ANGLE FROM TOP)

for tt = 1:Nb_im

    %%%% ESTABLISH COORDINATES OF LONGITUDINAL PATHLINES
    yc_b = R_b(tt)*cos(psi);
    r_b = yc_b./repmat(cos(phi),Nb_lin,1);
    xc_b = R_b(tt)*sin(psi).*repmat(sin(theta)',1,Nb_phi).*repmat([1;-1],1,Nb_phi);
    y_b = uint16(-yc_b+Origin);
    x_b = uint16(xc_b+Origin);

    yc_r = R_r(tt)*cos(psi);
    r_r = yc_r./repmat(cos(phi),Nb_lin,1);
    xc_r = R_r(tt)*sin(psi).*repmat(sin(theta)',1,Nb_phi).*repmat([1;-1],1,Nb_phi);
    y_r = uint16(-yc_r+Origin);
    x_r = uint16(xc_r+Origin);

    yc_ir = R_ir(tt)*cos(psi);
    r_ir = yc_ir./repmat(cos(phi),Nb_lin,1);
    xc_ir = R_ir(tt)*sin(psi).*repmat(sin(theta)',1,Nb_phi).*repmat([1;-1],1,Nb_phi);
    y_ir = uint16(-yc_ir+Origin);
    x_ir = uint16(xc_ir+Origin);

    %%%% APPLY FILTER TO ENTIRE IMAGE
    filt = ones(sq,sq)/sq^2; % blurs the image and dampens some noise
    B(:,:,tt) = imfilter(B(:,:,tt),filt);
    R(:,:,tt) = imfilter(R(:,:,tt),filt);
    IR(:,:,tt) = imfilter(IR(:,:,tt),filt);

    %%%% EXTRACT LIGHT INTENSITY ALONG LONGITUDINAL LINE
    %    ii = 1;
    for ii = 1:Nb_lin
```

```
        for jj = 1:Nb_phi
            I_blue(ii,jj,tt) = B(y_b(ii,jj),x_b(ii,jj),tt);%Retrieves BLUE of each pixel
            I_red(ii,jj,tt) = R(y_r(ii,jj),x_r(ii,jj),tt);% Retrieves RED of each pixel
            I_ir(ii,jj,tt) = IR(y_ir(ii,jj),x_ir(ii,jj),tt); %Retrieves IR of each pixel
        end

        %%%% FOURIER TRANSFORM ON SECTION AT TOP OF BUBBLE TO DETERMINE
        %%%% FREQUENCY
        Fs_top = 500;            % Sampling frequency
        T_top = 1/Fs_top;             % Sampling period
        L_top = 500;             % Length of signal
        t_top = (0:L_top-1)*T_top;        % Time vector

        intensity_top = I_red(ii,1:L_top,tt);
        intensity_fft_top = fft(intensity_top,L_top);
        mode_top = abs(intensity_fft_top(2:L_top/2+1)/L_top);
        f_top = Fs_top*(1:(L_top/2))/L_top;

        Freq_top(tt,ii) = sum(mode_top(1:20).*f_top(1:20))/sum(mode_top(1:20)); % Pondération

        %%%% FOURIER TRANSFORM ON SECTION AT BOTTOM OF BUBBLE TO DETERMINE
        %%%% FREQUENCY
        Fs_bot = 500;            % Sampling frequency
        T_bot = 1/Fs_bot;             % Sampling period
        L_bot = 500;             % Length of signal
        t_bot = (Nb_phi-L_bot+1:Nb_phi)*T_bot;      % Time vector

        intensity_bot = I_red(ii,Nb_phi-L_bot+1:Nb_phi,tt);
        intensity_fft_bot = fft(intensity_bot,L_bot);
        mode_bot = abs(intensity_fft_bot(2:L_bot/2+1)/L_bot);
        f_bot = Fs_bot*(1:(L_bot/2))/L_bot;

        Freq_bot(tt,ii) = sum(mode_bot(1:20).*f_bot(1:20))/sum(mode_bot(1:20)); % Pondération
    end
end
```

```
%% 2. TRANSFORM TIME DOMAIN OF FRINGES AND DETECT EXTREMA.
%%%% USE RATIO OF TWO FREQUENCIES TO TRANSFORM THE DOMAIN SO THAT
%%%% FREQUENCY IS CLOSER TO UNIFORM ACROSS LENGTH OF SIGNAL. THIS
%%%% RESULTS IN MORE CONSISTENT APPLICATION OF LOW-PASS BUTTERWORTH
%%%% FILTER AND MORE RELIABLE EXTRACTION OF EXTREMA

%%%% FIT LINE TO FREQUENCY EVOLVING THROUGH TIME
Fit_top1 = fit([1:Nb_im]',Freq_top(:,1),'poly1');
Fit_top2 = fit([1:Nb_im]',Freq_top(:,2),'poly1');
Fit_bot1 = fit([1:Nb_im]',Freq_bot(:,1),'poly1');
Fit_bot2 = fit([1:Nb_im]',Freq_bot(:,2),'poly1');

%%%% CALCULATE A FREQENCY RATIO AT EVERY TIME-STEP FROM FIT LINE
freq_ratio(:,1) = Fit_bot1(1:Nb_im)./Fit_top1(1:Nb_im);
freq_ratio(:,2) = Fit_bot2(1:Nb_im)./Fit_top2(1:Nb_im);

%%%% APPLY FREQUENCY TRANSFORMATION USING FREQUENCY RATIO AT EACH tt
for tt = 1:Nb_im
    for ii = 1:Nb_lin
        if freq_ratio(tt,ii) > 1
            vv1 = @(x) (freq_ratio(tt,ii)/Nb_phi)*x.^2+x;
            phi_trans = vv1(1:Nb_phi);
            phi_trans(2,:) = 1:Nb_phi;
            phi_trans_long = interp1(phi_trans(1,:),phi_trans(2,:),1:phi_trans(1,end));

        elseif freq_ratio(tt,ii) < Freq_top(tt,ii)
            vv1 = @(x) (1/(freq_ratio(tt,ii)*Nb_phi))*(Nb_phi-x).^2+(Nb_phi-x);
            phi_trans1 = vv1(1:Nb_phi); % Transform domain
            phi_trans2 = -phi_trans1; % Reflect about the x-axis
            phi_trans = phi_trans2+phi_trans1(1); % Translate upward
            phi_trans(2,:) = 1:Nb_phi;
            phi_trans_long = interp1(phi_trans(1,:),phi_trans(2,:),1:phi_trans(1,end));

        else
            phi_trans = [1:Nb_phi;1:Nb_phi];
```

```
            phi_trans_long = phi_trans(1,:);
        end

        %%%% INTERPOLATE INTENSITY VALUES FOR POINTS IN TRANSFORMED TIME
        %%%% DOMAIN
        I_blue_trans = interp1([1,phi_trans(1,2:end)],I_blue(ii,:,tt),1:phi_trans(1,end),'spline');
%Transformed Intensity Vector
        I_red_trans = interp1([1,phi_trans(1,2:end)],I_red(ii,:,tt),1:phi_trans(1,end),'spline'); %Transformed
Intensity Vector
        I_ir_trans = interp1([1,phi_trans(1,2:end)],I_ir(ii,:,tt),1:phi_trans(1,end),'spline'); %Transformed
Intensity Vector

        %%%% LOW-PASS FILTER
        Nb_pts = length(I_blue_trans);
        fe = Nb_pts/(2*pi); % sampling frequency
        fn = fc_lo/(fe/2); % normalized cut-off frequency
        [b_r,a_r] = butter(order_lo(1),fn(1),'low');
        [b_ir,a_ir] = butter(order_lo(2),fn(2),'low');
        [b_b,a_b] = butter(order_lo(3),fn(3),'low');
        I_red_s = filtfilt(b_r,a_r,I_red_trans')';
        I_ir_s = filtfilt(b_ir,a_ir,I_ir_trans')';
        I_blue_s = filtfilt(b_b,a_b,I_blue_trans')';

        %%%% PROPERTIES OF FINDPEAKSX FUNCTION
        SlopeThreshold = 0;
        AmpThreshold = -5;
        smoothwidth = length(I_blue_s)/100;
        peakgroup = 10;
        smoothtype = 2;

        %%%% FIND LOCATIONS OF EXTREMA
        %%%% EXTRACT BLUE EXTREMA
        Ib1=findpeaksx(1:Nb_pts,I_blue_s,SlopeThreshold,AmpThreshold,smoothwidth,peakgroup,smoothtype);
        Ib2=findpeaksx(1:Nb_pts,-I_blue_s,SlopeThreshold,AmpThreshold,smoothwidth,peakgroup,smoothtype);
        Ib2(:,3) = -Ib2(:,3);
        [ss1,~]=size(Ib1);
```

```
[ss2,~]=size(Ib2);
Extr_trans_b = sortrows([[Ib1(:,2:3)';66*ones(1,ss1)],[Ib2(:,2:3)';98*ones(1,ss2)]]')';
Extr_trans_b(:,Extr_trans_b(1,:)==0)=[];
Extr_b = Extr_trans_b;
Extr_b(1,:) = phi_trans_long(Extr_trans_b(1,:));

%%%% EXTRACT RED EXTREMA
Ir1=findpeaksx(1:Nb_pts,I_red_s,SlopeThreshold,AmpThreshold,smoothwidth,peakgroup,smoothtype);
Ir2=findpeaksx(1:Nb_pts,-I_red_s,SlopeThreshold,AmpThreshold,smoothwidth,peakgroup,smoothtype);
Ir2(:,3) = -Ir2(:,3);
[ss1,~]=size(Ir1);
[ss2,~]=size(Ir2);
Extr_trans_r = sortrows([[Ir1(:,2:3)';82*ones(1,ss1)],[Ir2(:,2:3)';114*ones(1,ss2)]]')';
Extr_trans_r(:,Extr_trans_r(1,:)==0)=[];
Extr_r = Extr_trans_r;
Extr_r(1,:) = phi_trans_long(Extr_trans_r(1,:));

%%%% EXTRACT INFRARED EXTREMA
Iir1=findpeaksx(1:Nb_pts,I_ir_s,SlopeThreshold,AmpThreshold,smoothwidth,peakgroup,smoothtype);
Iir2=findpeaksx(1:Nb_pts,-I_ir_s,SlopeThreshold,AmpThreshold,smoothwidth,peakgroup,smoothtype);
Iir2(:,3) = -Iir2(:,3);
[ss1,~]=size(Iir1);
[ss2,~]=size(Iir2);
Extr_trans_ir = sortrows([[Iir1(:,2:3)';73*ones(1,ss1)],[Iir2(:,2:3)';105*ones(1,ss2)]]')';
Extr_trans_ir(:,Extr_trans_ir(1,:)==0)=[];
Extr_ir = Extr_trans_ir;
Extr_ir(1,:) = phi_trans_long(Extr_trans_ir(1,:));

%%%% REMOVE PTS AT TOP AND BOTTOM 20 PIXELS
B_low = (Extr_b(1,:)>20) & (Extr_b(1,:)<(Nb_phi-20));
E_b{tt,ii} = Extr_b.*repmat(B_low,3,1);

R_low = (Extr_r(1,:)>20) & (Extr_r(1,:)<(Nb_phi-20));
E_r{tt,ii} = Extr_r.*repmat(R_low,3,1);

IR_low = (Extr_ir(1,:)>20) & (Extr_ir(1,:)<(Nb_phi-20));
```

```
        E_ir{tt,ii} = Extr_ir.*repmat(IR_low,3,1);

        %%%% ALLOCATING FOR FUNCTION RESULTS
        I_trans.blue{tt,ii} = [I_blue_trans;I_blue_s];
        I_trans.red{tt,ii} = [I_red_trans;I_red_s];
        I_trans.ir{tt,ii} = [I_ir_trans;I_ir_s];

        E_trans.blue{tt,ii} = Extr_trans_b;
        E_trans.red{tt,ii} = Extr_trans_r;
        E_trans.ir{tt,ii} = Extr_trans_ir;

    end
end


%% 4. OUTPUT VARIABLES
a3_results.E_b = E_b;
a3_results.E_r = E_r;
a3_results.E_ir = E_ir;
a3_results.E_b2 = E_b;
a3_results.E_r2 = E_r;
a3_results.E_ir2 = E_ir;
a3_results.Nb_im = Nb_im;
a3_results.R_b = R_b;
a3_results.R_r = R_r;
a3_results.R_ir = R_ir;
a3_results.Freq_top = Freq_top;
a3_results.Freq_bot = Freq_bot;
a3_results.Fit_top1 = Fit_top1;
a3_results.Fit_top2 = Fit_top2;
a3_results.Fit_bot1 = Fit_bot1;
a3_results.Fit_bot2 = Fit_bot2;
a3_results.I_trans = I_trans;
a3_results.E_trans = E_trans;

save(sprintf('..\\a3_EXTREMA\\%s_EXTREMA',filename),'a3_results');
```

A2 Extrema2String.m

```
%%%% a4_Extrema2String.m
%%%% CREATE A 3-D MATRIX OF ALL EXTREMA IN TIME AND SPACE
%%%% INPUT: LOCATION, INTENSITY, AND ASCII CHAR VECTOR FOR EACH COLOUR AT
%%%%         EACH TIME-STEP
%%%%    1. THE VECTORS FROM (3) ARE INPUT, AND THE "BBRRII" ARE COMBINED TO
%%%%    A STRING AT EACH TIME-STEP
%%%%    2. EACH STRING IS COMPARED (USING THE EDIT DISTANCE) TO THE
%%%%    PREVIOUS STRING AND THEN SHIFTED TO ALIGN WITH IT. THE LOCATION
%%%%    INFORMATION ALSO SHIFTS WITH THE ASCII CHARS
%%%% OUTPUT: 3D MATRIX OF EXTREMA IN TIME AND SPACE, WITH LOCATION AND
%%%% COLOUR TYPE

%%-------------------------------------------------------------------------
    clear
    close all
    filename = '160617-042'; %Filename of trial
    load(sprintf('..\\a3_EXTREMA\\%s_EXTREMA',filename)); %Load info of extrema


%% 0. PREALLOCATION AND DEFINING PROPERTIES
%%%% INPUT VARIABLES
E_b = a3_results.E_b;
E_r = a3_results.E_r;
E_ir = a3_results.E_ir;
E_b2 = a3_results.E_b2;
E_r2 = a3_results.E_r2;
E_ir2 = a3_results.E_ir2;
Nb_im = a3_results.Nb_im;
Nb_lin = a3_results.Nb_lin;

%%%% PARAMETERS OF PATTERN RECOGNITION LOOP
```

```
Nb_im_new = 40; %Number of images can be reduced if signal is not clear enough in previous step
max_phi = 1000;
Nb_guesses = 7;
E_b3 = E_b2;
E_r3 = E_r2;
E_ir3 = E_ir2;
if ~isnan(Nb_im_new)
    Nb_im = Nb_im_new;
end

%% 1. MAIN BODY
%%%% PREALLOCATION
pat_length = zeros(Nb_im,Nb_lin);
pattern_all = cell(Nb_im,Nb_lin);
transl = zeros(Nb_im,Nb_lin);
ind = zeros(Nb_im,Nb_lin);
V = cell(Nb_im,Nb_guesses,Nb_lin);

%%%% ADJUST RANGE OF PHI THAT IS USED FOR COMPARISON
for ii = 1:Nb_lin
    for tt = 1:Nb_im
        E_b3{tt,ii}(:,E_b2{tt,ii}(1,:)>max_phi)=[];
        [s_r,~] = size(E_b3{tt,ii});
        if s_r == 1
            E_b3{tt,ii} = reshape(E_b3{tt,ii},[3,length(E_b3{tt,ii})/3]);
        end

        E_r3{tt,ii}(:,E_r2{tt,ii}(1,:)>max_phi)=[];
        [s_r,~] = size(E_r3{tt,ii});
        if s_r == 1
            E_r3{tt,ii} = reshape(E_r3{tt,ii},[3,length(E_r3{tt,ii})/3]);
        end

        E_ir3{tt,ii}(:,E_ir2{tt,ii}(1,:)>max_phi)=[];
        [s_r,~] = size(E_ir3{tt,ii});
        if s_r == 1
```

```
            E_ir3{tt,ii} = reshape(E_ir3{tt,ii},[3,length(E_ir3{tt,ii})/3]);
        end
    end
end

%%%% EXTRACT THE EXTREMA PATTERNS OF EACH WAVELENGTH AND COMBINE AT EACH
%%%% TIMESTEP
for ii = 1:Nb_lin
    %%%% Convert to a string for each timestep
    for tt = 1:Nb_im
        pattern = [E_b3{tt,ii},E_r3{tt,ii},E_ir3{tt,ii}];
        pattern(:,all(~any(pattern),1)) = [];
        pattern = sortrows(pattern')';
        pat_length(tt,ii)=length(pattern);
        pattern_all{tt,ii}=pattern;
        pattern_char{tt,ii} = char(squeeze(pattern(3,:)));

    end

    %%%% Compare each timestep to the previous one, and determine the shortest edit
    %%%% distance
    for tt = 2:Nb_im
        editCost_tt = 0;
        PatComp1 = pattern_char{tt-1,ii};
        PatComp2 = pattern_char{tt,ii};
        lengther(tt,ii) = min([length(PatComp1),length(PatComp2)]);

        if lengther(tt,ii) > 14

            for jj = 1:Nb_guesses

                [editCost_tt1(jj),Vttjj]=EditDistance(PatComp1(jj:jj+lengther(tt,ii)-
10),PatComp2(4:lengther(tt,ii)-6));
                V1{tt,jj}=Vttjj;
                [editCost_tt2(jj),Vttjj]=EditDistance(PatComp1(jj+1:jj+lengther(tt,ii)-10-
1),PatComp2(4+1:lengther(tt,ii)-6-1));
```

```
                V2{tt,jj}=Vttjj;
                [editCost_tt3(jj),Vttjj]=EditDistance(PatComp1(jj+2:jj+lengther(tt,ii)-10-
2),PatComp2(4+2:lengther(tt,ii)-6-2));
                V3{tt,jj}=Vttjj;
                [editCost_tt4(jj),Vttjj]=EditDistance(PatComp1(jj+3:jj+lengther(tt,ii)-10-
3),PatComp2(4+3:lengther(tt,ii)-6-3));
                V4{tt,jj}=Vttjj;

                editCost_tt = editCost_tt1 + editCost_tt2 + editCost_tt3 + editCost_tt4;
            end

            [minVal_tt,ind_tt] = min(editCost_tt);
            min_count = sum(editCost_tt == minVal_tt);
            kk = 1;
            EC = 0;

            while min_count > 1 && kk < 5
                for jj = 1:Nb_guesses
                    EC(kk,jj) = EditDistance(PatComp1(jj+kk-1:jj+kk+5),PatComp2(kk+2:kk+8));
                end

                [minVal_tt,ind_tt] = min(EC(kk,:));
                min_count = sum(EC(kk,:) == minVal_tt);
                trouble(tt,ii) = kk;
                kk = kk + 1;
                ind_tt = ind_tt+1;
            end

            editCost2{tt,ii} = EC;
            editCost{tt,ii} = editCost_tt;
            ind(tt,ii) = ind_tt;
            transl(tt,ii) = transl(tt-1,ii)-4+ind(tt,ii);

        else
            for jj = 1:lengther(tt,ii)-5
```

```
[editCost_tt(jj),Vttjj]=EditDistance(PatComp1(jj:lengther(tt,ii)),PatComp2(1:lengther(tt,ii)-jj+1));
                V{tt,jj,ii}=Vttjj;
                editCost_tt(jj) = editCost_tt(jj);
            end

            [minVal_tt,ind_tt] = min(editCost_tt);
            min_count = sum(editCost_tt == minVal_tt);

            editCost{tt,ii} = editCost_tt;
            ind(tt,ii) = ind_tt;
            transl(tt,ii) = transl(tt-1,ii)-1+ind(tt,ii);

        end
    end
    End_sol{ii} = zeros(5,200,Nb_im);
    End_sol{ii}(1:3,21:pat_length(1,ii)+20,1) = pattern_all{1,ii};

    for tt = 2:Nb_im
        End_sol{ii}(1:3,21+transl(tt,ii):pat_length(tt,ii)+transl(tt,ii)+20,tt)=pattern_all{tt,ii};
    end

    End_sol{ii} = permute(End_sol{ii},[3 2 1]);
    End_sol_char{ii} = char(squeeze(End_sol{ii}(:,:,3))); %Shows all the strings with appropriate
translation
    LineNumber = num2str((1:Nb_im)');
    End_sol_char{ii} = [LineNumber End_sol_char{ii}];
end

%%%% OUTPUT VARIABLES
a4_results.E_b3 = E_b3;
a4_results.E_r3 = E_r3;
a4_results.E_ir3 = E_ir3;
a4_results.End_sol = End_sol;
a4_results.End_sol_char = End_sol_char;
a4_results.Nb_im = Nb_im;
```

```
save(sprintf('..\\a4_PATTERN\\%s_PATTERN',filename),'a4_results');
```

A3 ThicknessProfCalc.m

```
%%%% a5_ThicknessProfileCalc
%%%% DETERMINE THICKNESS AT EACH EXTREMUM,AND FIT A SURFACE (IN TIME AND
%%%% SPACE)
%%%% INPUT: 3D MATRIX OF EXTREMA IN TIME AND SPACE, WITH LOCATION AND
%%%%        COLOUR TYPE
%%%%    1. THE MODE OF ASCII CHARS FOR EACH COLUMN IS FOUND. THIS CREATES
%%%%    THE "MASTER" STRING OF THE EXPERIMENT
%%%%    2. THE MASTER IS THEN COMPARED TO OUR LIBRARY (CALIBRATED) STRING
%%%%    USING THE EDIT DISTANCE TO FIND THE SECTION WHERE IT MATCHES MOST
%%%%    CLOSELY. ONCE THE MASTER IS MATCHED, THEN THE ORDER OF EVERY EXTREMA
%%%%    IN THE 3D MATRIX IS KNOWN.
%%%%    3. THE THICKNESS FROM THE LIBRARY FOR EACH CORRESPONDING EXTREMUM IS
%%%%    THEN RECORDED AS ANOTHER LAYER IN THE 3D MATRIX. IF THE CHARACTER IN
%%%%    THE 3D MATRIX DOES NOT MATCH THE LIBRARY AT ANY PARTICULAR POINT,
%%%%    THEN THAT LOCATION IS ASSIGNED "NAN"
%%%%    4. THE LAYER OF THICKNESS DATA IN THE 3D MATRIX, ALONG WITH THE TIME
%%%%    AND LOCATION, ARE USED TO FIT THE THICKNESS PROFILE SURFACE
%%%%    5. THE SURFACE SLOPE IN TIME IS TAKEN FOR DRAINAGE RATE (DH/DT), AND
%%%%    THE EXTRAPOLATED THICKNESS VALUE AT POINT (1,1) IS TAKEN FOR RUPTURE
%%%%    THICKNESS (H_R)
%%%% OUTPUT: THICKNESS PROFILE SURFACE(TIME AND SPACE), DH/DT, AND H_R

%% ------------------------------------------------------------------------
clear
close all
filename = '160517-022';
load(sprintf('..\\a2_PRETREAT\\%s_PRETREAT',filename));
```

```
load(sprintf('..\\a3_EXTREMA\\%s_EXTREMA',filename));
load(sprintf('..\\a4_PATTERN\\%s_PATTERN',filename));

%% 0. PREALLOCATION AND DEFINING PROPERTIES
%%%%PROPERTIES OF THE SYSTEM
sys_props.n_a = 1.00;           %Refractive index of air
sys_props.n_w = 1.333;          %Refractive index of water
sys_props.lambda_b = 420;       %Wavelength of blue light
sys_props.lambda_r = 623;       %Wavelength of red light
sys_props.lambda_ir = 805;      %Wavelength of infrared light

%%%% INPUT VARIABLES
load('library');

R0_b = a2_results.R0_b;
R0_r = a2_results.R0_r;
R0_ir = a2_results.R0_ir;

R_b = a3_results.R_b;
R_r = a3_results.R_r;
R_ir = a3_results.R_ir;
E_b = a3_results.E_b;
E_r = a3_results.E_r;
E_ir = a3_results.E_ir;
Nb_lin = 2; %a3_results.Nb_lin;

Nb_im = a4_results.Nb_im;
if Nb_im >40
    Nb_im = 40;
end
E_b3 = a4_results.E_b3;
E_r3 = a4_results.E_r3;
E_ir3 = a4_results.E_ir3;
End_sol{1} = a4_results.End_sol{1}(1:Nb_im,:,:);
End_sol{2} = a4_results.End_sol{2}(1:Nb_im,:,:);
```

```
%%%% PROPERTIES OF THE SYSTEM
n_a = sys_props.n_a;
n_w = sys_props.n_w;
lambda_b = sys_props.lambda_b;
lambda_r = sys_props.lambda_r;
lambda_ir = sys_props.lambda_ir;
Nb_phi = anlys_props.Nb_phi;

%%%% 1. BODY
%%%%PREALLOCATION
mm = zeros(1,2);
ratio_extrema = zeros(1,2);
h_rupture = zeros(1,2);
h_rupture2 = zeros(1,2);
h_rupture3 = zeros(1,2);
h_SurfFit = cell(1,2);
f_t = cell(1,2);
drainage_rate = zeros(1,2);
Profile_rupture = cell(1,2);

%%%% COMPARE THE BUBBLE LIFETIME STRING TO LIBRARY STRING
for ii = 1:Nb_lin
    End_sol{ii} = End_sol{ii}.*repmat(End_sol{ii}(:,:,1)<1001,1,1,5); % End_sol represents only 0-pi/2
    End_sol{ii}(End_sol{ii}==0) = NaN;
    FullString{ii} = mode(End_sol{ii}(:,:,3),1);
    FullString{ii}(isnan(FullString{ii})) = [];
    FullString{ii} = char(FullString{ii});
    lib_str = char(lib(1,:));

    FS_length(ii) = length(FullString{ii});
    lib_length = length(lib);
    FullString_sample = FullString{ii}(1:20);

    for jj = 1:lib_length-20
        lib_sample = lib_str(jj:jj+19);
        [EC_full(ii,jj),~] = EditDistance(lib_sample,FullString_sample);
```

```
end

[~,mm(ii)] = min(EC_full(ii,:));
%--------------------------------------------------------------------------
vlib1 = repmat([zeros(1,20),lib(1,mm(ii):end)],Nb_im,1);
vlib2 = repmat([zeros(1,20),lib(4,mm(ii):end)],Nb_im,1);

vlib1(vlib1==0) = NaN;
vlib2(vlib1==0) = NaN;

profile_location{ii} = End_sol{ii}(:,1:20+length(lib)-mm(ii)+1,1); %Location (phi)
profile_char{ii} = End_sol{ii}(:,1:20+length(lib)-mm(ii)+1,3); %Chars

profile_thick1{ii} = zeros(Nb_im,20+length(lib)-mm(ii)+1); %Thicknesses w/o exclusion
profile_thick1{ii}(profile_char{ii} > 0) = vlib2(profile_char{ii} > 0);
profile_thick1{ii}(profile_thick1{ii}==0) = NaN;

profile_thick2{ii} = zeros(Nb_im,20+length(lib)-mm(ii)+1); %Thicknesses w/ exclusion
profile_thick2{ii}(profile_char{ii} == vlib1) = vlib2(profile_char{ii} == vlib1);
profile_thick2{ii}(profile_thick2{ii}==0) = NaN;


Count_1(ii) = sum(sum(profile_thick1{ii}(:,:) > 0));
Count_2(ii) = sum(sum(profile_thick2{ii}(:,:) > 0));

ratio_extrema(ii) = Count_2(ii)/Count_1(ii);

[row,~] = find(~isnan(profile_thick2{ii}));
profile_vect{ii} = zeros(length(row),3);
time_vect{ii} = row; % Time Vector

position_vect{ii} = ~isnan(profile_thick2{ii}).*profile_location{ii};
position_vect{ii}(position_vect{ii} == 0) = NaN;
position_vect{ii} = reshape(position_vect{ii},[],1);
position_vect{ii}(isnan(position_vect{ii}))=[]; % Position Vector
```

```
    h_vect{ii} = reshape(profile_thick2{ii},[],1);
    h_vect{ii}(isnan(h_vect{ii}))=[];

    if ratio_extrema(ii) > 0.1
        %%%%%SURFACE FIT TO ABOVE THREE VECTORS
        h_SurfFit{ii} = fit([time_vect{ii},position_vect{ii}],h_vect{ii},'poly13');
        h_rupture(ii) = h_SurfFit{ii}(1,1);
        [f_t{ii},~] = differentiate(h_SurfFit{ii},[[1:Nb_im]',ones(Nb_im,1)]);
        drainage_rate(ii) = f_t{ii}(1)*5;

        %%%% ALTERNATIVE H_RUPTURE METHODS
        Profile_rupture{ii} = [End_sol{ii}(1,1:length(profile_thick2{ii}(1,:)),1);profile_thick2{ii}(1,:)];
        Profile_rupture{ii}(:,isnan(Profile_rupture{ii}(2,:))) = [];
        [~,ss] = size(Profile_rupture{ii});
        if ss > 1
            h_rupture2(ii) = Profile_rupture{ii}(2,1);
            RuptureFit{ii} = fit([Profile_rupture{ii}(1,1:2)]',[Profile_rupture{ii}(2,1:2)]','poly1');
            h_rupture3(ii) = RuptureFit{ii}(1);
        end
    end

end

%%%% OUTPUT VARIABLES
a5_results.profile_thick1 = profile_thick1;
a5_results.profile_thick2 = profile_thick2;
a5_results.time_vect = time_vect;
a5_results.position_vect = position_vect;
a5_results.h_vect = h_vect;
a5_results.h_SurfFit = h_SurfFit;
a5_results.h_rupture = h_rupture;
a5_results.h_rupture2 = h_rupture2;
a5_results.h_rupture3 = h_rupture3;
a5_results.f_t = f_t;
a5_results.drainage_rate = drainage_rate;
```

```
a5_results.ratio_extrema = ratio_extrema;
a5_results.R0_b = R0_b;
a5_results.R0_r = R0_r;
a5_results.R0_ir = R0_ir;
a5_results.Nb_im = Nb_im;

        save(sprintf('..\\a5_THICKPROF\\%s_THICKPROF',filename),'a5_results');
```

Appendix B: Equipment Specifications

B1 Camera Spectral Response

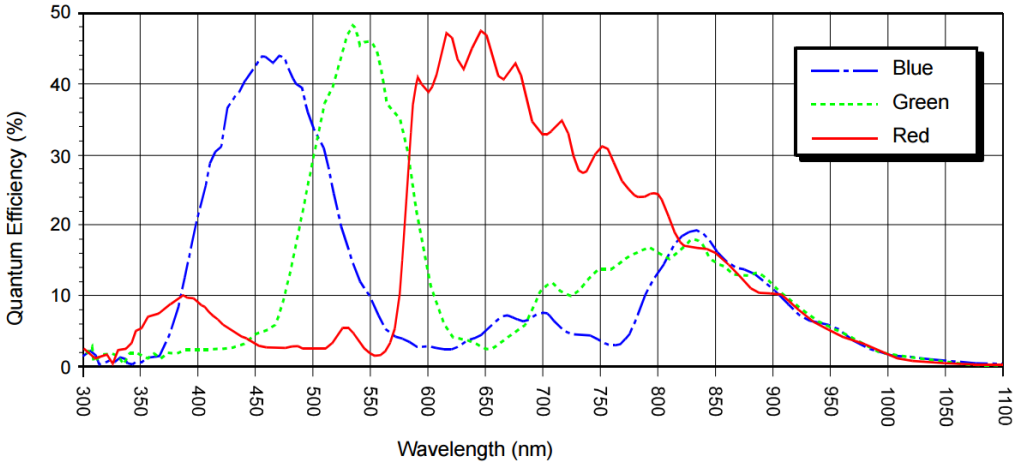

Fig. 19: acA2000-165uc, acA2040-90uc Spectral Response (From Sensor Data Sheet)

B2 Light Source Specifications

High-Power LED Collimator Sources

(Part Numbers: LCS-xxxx-xx-xx)

FEATURES

- Interchangeable aspherical collimating lens
- High numerical aperture(NA)
- High power
- Wide range of available wavelengths
- Adjustable focus
- Optional focusing module
- Optional lightguide adapter
- Multiple mounting features for lab and OEM applications
- Integrated heat sink
- Cooling fan for > 7W models

APPLICATIONS

- Microscope illuminator
- General purpose light sources
- Fiber coupling with optional focusing module

Type-H

PRODUCT DESCRIPTION

A LED collimator consists of a collimating lens and a LED emitter. The LED emitter is placed at the focal plane of the collimating lens which images the LED emitter into infinity. LED collimators can be used as the light source in an illumination system. For example LED collimators can replace the standard lamp assembly in a microscope to provide stable, intense, and fast-modulated illumination. Typically the rest of the illumination optics will image the LED emitter onto the pupil of the imaging optics whereas the lens aperture on the collimator where Intensity is uniform will be projected onto the object. The LED emitters are mounted directly onto the metal base of the collimator which also features an integrated heat sink.

The LED collimators include a 1.5-meter cable with two bare-wire terminals at the end. The light sources can be driven by Mightex LED controllers or other LED controllers and current sources. An optional focusing module can be mounted on the front of the LED collimator to focus light into a tight spot which is an image of the LED emitter. One of the applications with the focusing module is coupling LED light into a fiber or a light guide.

Multi-chip LED emitters have been added to the product portfolio. Some of these 7W to 15W LEDs have total optical power exceeding 1W, quadrupling the power of a single-chip LED. Models with higher powers (7W and higher) feature a cooling fan, and have a different formfactor compared to other models. Please examine the Installation drawings carefully. Power supply for the cooling fan is included in the price of the LED sources.

PERFORMANCE SPECIFICATIONS

Type-A LCS (passively cooled with no cooling fan)
Type-B LCS (with a cooling fan)

Part Number	Type [2] (A or B)	Wavelength (nm)	Half Diverging Angle(deg.)				I_{op} (mA)	V_{op} (V)	Output Power (mW)
			ϕ11mm[1]	ϕ22mm[1]	ϕ38mm[1]	ϕ48mm[1]			
LCS-0365-02-xx	A	365	3.4	1.7	1.0	0.75	500	3.8	80
LCS-0365-07-xx	B	365	6.8	3.4	2.0	1.5	500	15	400
LCS-0365-11-xx	B	365	6.8	3.4	2.0	1.5	700	15.8	500
LCS-0380-03-xx	A	380	3.4	1.7	1.0	0.75	1,000	3.2	120
LCS-0385-02-xx	A	385	3.4	1.7	1.0	0.75	500	3.8	100
LCS-0385-07-xx	B	385	6.8	3.4	2.0	1.5	500	15	500
LCS-0385-11-xx	B	385	6.8	3.4	2.0	1.5	700	15.5	625
LCS-0390-03-xx	A	390	3.4	1.7	1.0	0.75	1,000	3.1	250
LCS-0395-03-xx	A	395	3.4	1.7	1.0	0.75	1,000	3.1	270
LCS-0400-01-xx	A	400	5.0	2.5	1.5	1.1	350	3.5	100
LCS-0400-03-xx	A	400	3.4	1.7	1.0	0.75	1,000	3.1	265
LCS-0400-05-xx	A	400	5.0	2.5	1.5	1.1	1,000	4.1	240
LCS-0400-17-xx	B	400	10	5.0	3.0	2.2	1,000	16.5	810
LCS-0405-03-xx	A	405	3.4	1.7	1.0	0.75	1,000	3.0	325
LCS-0410-03-xx	A	410	3.4	1.7	1.0	0.75	1,000	3.0	315
LCS-0415-03-xx	A	415	3.4	1.7	1.0	0.75	1,000	3.0	310
LCS-0420-02-xx	A	420	3.4	1.7	1.0	0.75	500	3.9	100
LCS-0420-03-xx	A	420	3.4	1.7	1.0	0.75	1,000	3.0	310
LCS-0425-03-xx	A	425	3.4	1.7	1.0	0.75	1,000	3.0	290
LCS-0455-03-xx	A	455	3.4	1.7	1.0	0.75	1,000	3.9	280
LCS-0455-05-xx	A	455	10	5.0	3.0	2.2	700	6.8	350
LCS-0470-03-xx	A	470	3.4	1.7	1.0	0.75	1,000	3.9	200
LCS-0470-15-xx	B	470	6.8	3.4	2.0	1.5	1,000	15	600
LCS-0470-14-xx	B	470	3.4	1.7	1.0	0.75	3,000	4.6	500
LCS-0490-03-xx	A	490	5.0	2.5	1.5	1.1	700	3.7	120
LCS-0505-03-xx	A	505	3.4	1.7	1.0	0.75	1,000	3.9	135
LCS-0530-03-xx	A	530	3.4	1.7	1.0	0.75	1,000	3.9	100
LCS-0530-15-xx	B	530	10	5.0	3.0	2.2	1,000	15	300
LCS-0540-14-xx	B	540 broadband	4.4	2.2	1.3	1.0	3,000	4.6	500
LCS-0560-02-xx	A	560 broadband	3.4	1.7	1.0	0.75	700	2.9	180
LCS-0560-03-xx	A	560 broadband	4.4	2.2	1.3	1.0	1,000	2.9	240
LCS-0585-03-xx	A	585 broadband	4.4	2.2	1.3	1.0	700	2.9	82
LCS-0590-03-xx	A	590	3.4	1.7	1.0	0.75	1,000	3.9	65
LCS-0590-10-xx	B	590	10	5.0	3.0	2.2	1,000	10	200
LCS-0617-03-xx	A	617	3.4	1.7	1.0	0.75	1,000	3.9	280
LCS-0617-10-xx	B	617	6.8	3.4	2.0	1.5	1,000	10.8	600
LCS-0625-03-xx	A	625	3.4	1.7	1.0	0.75	1,000	3.9	280
LCS-0656-03-xx	A	656	3.4	1.7	1.0	0.75	1,000	3.1	280
LCS-0657-03-xx	A	657	5.0	2.5	1.5	1.1	350	2.4	100
LCS-0680-02-xx	A	680	3.4	1.7	1.0	0.75	600	2.7	75

1. Clear aperture diameter. Use these two-digit numbers to replace xx in the part number; and 2. Type-A, Type-B and Type-H LED collimator sources have different installation drawings. Type-A does not include a cooling fan, whereas Type-B and Type-H do. When ordering an LED controller for a Type-B LED, please make sure to upgrade the AC/DC power adapter from the 'standard' 12V to 24V.

Mightex Systems, 2343 Brimley Road, Suite 868, Toronto, Ontario M1S 3L6, Canada
Tel: 1-416-840-4991 or 1-925-218-1885, Fax: 1-416-840-6541, Email: sales@mightex.com
www.mightex.com or www.mightexsystems.com

Version 6.0, December 2011

Mightex
Simply Brighter

PERFORMANCE SPECIFICATIONS (Cont'd)

Part Number	Type [2] (A or B)	Wavelength (nm)	Half Diverging Angle(deg.)				I_{op} (mA)	V_{op} (V)	Output Power (mW)
			ϕ11mm[1]	ϕ22mm[1]	ϕ38mm[1]	ϕ48mm[1]			
LCS-0700-01-xx	A	700	3.4	1.7	1.0	0.75	500	2.1	51
LCS-0720-01-xx	A	720	3.4	1.7	1.0	0.75	600	2.2	73
LCS-0740-03-xx	A	740	5.0	2.5	1.5	1.1	1,000	2.5	200
LCS-0740-10-xx	B	740	10	5.0	3.0	2.2	1,000	9.5	600
LCS-0780-02-xx	A	780	3.4	1.7	1.0	0.75	800	2.5	110
LCS-0810-02-xx	A	810	3.4	1.7	1.0	0.75	800	2.2	120
LCS-0850-02-xx	A	850	3.4	1.7	1.0	0.75	1,000	2.1	240
LCS-0850-03-xx	A	850	3.4	1.7	1.0	0.75	1,000	3.0	430
LCS-0940-02-xx	A	940	3.4	1.7	1.0	0.75	1,000	1.8	200
LCS-0980-01-xx	A	980	3.4	1.7	1.0	0.75	500	1.4	30
LCS-6500-03-xx	A	glacier white 6,500K	3.4	1.7	1.0	0.75	1,000	3.6	180
LCS-6500-15-xx	B	glacier white 6,500K	6.8	3.4	2.0	1.5	1,000	15	540
LCS-5500-03-xx	A	cool white 5,500K	3.4	1.7	1.0	0.75	1,000	3.9	170
LCS-4000-03-xx	A	warm white 4,000K	3.4	1.7	1.0	0.75	1,000	3.9	180

1. Clear aperture diameter. Use these two-digit numbers to replace xx in the part number; and 2. Type-A, Type-B and Type-H LED collimator sources have different installation drawings. Type-A does not include a cooling fan, whereas Type-B and Type-H do. When ordering an LED controller for a Type-B LED, please make sure to upgrade the AC/DC power adapter from the 'standard' 12V to 24V.

Type-H LCS (high current, with a cooling fan)

Part Number	Type [2]	Wavelength (nm)	Half Diverging Angle(deg.)				I_{op} (A)	V_{op} (V)	Output Power (mW)
			ϕ11mm[1]	ϕ22mm[1]	ϕ38mm[1]	ϕ48mm[1]			
LCS-0405-50-xx	H	405	10	5.0	3.0	2.2	13	3.8	2,500
LCS-0470-50-xx	H	470	10	5.0	3.0	2.2	13	3.8	3,300
LCS-0525-60-xx	H	525	10	5.0	3.0	2.2	13	4.6	1,300
LCS-0625-38-xx	H	625	10	5.0	3.0	2.2	13	2.9	1,100
LCS-6500-33-xx	H	Glacier White 6,500	10	5.0	3.0	2.2	9	3.7	2,000

1. Clear aperture diameter. Use these two-digit numbers to replace xx in the part number; and 2. Type-A, Type-B and Type-H LED collimator sources have different installation drawings. Type-A does not include a cooling fan, whereas Type-B and Type-H do. When ordering an LED controller for a Type-B LED, please make sure to upgrade the AC/DC power adapter from the 'standard' 12V to 24V.

LED SPECTRA

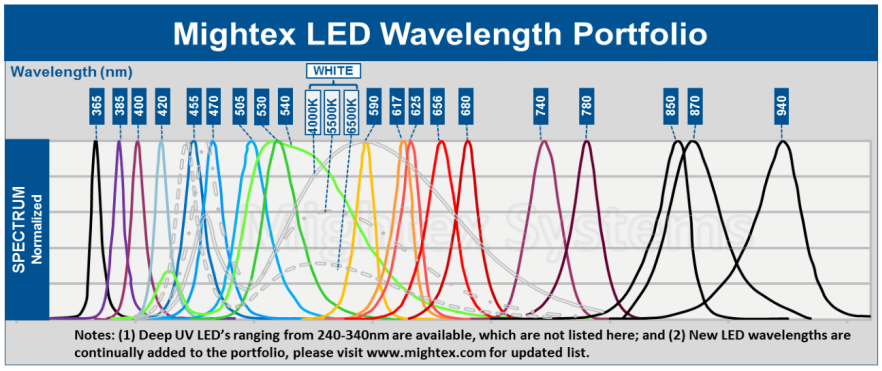

Mightex Systems, 2343 Brimley Road, Suite 868, Toronto, Ontario M1S 3L6, Canada
Tel: 1-416-840-4991 or 1-925-218-1885, Fax: 1-416-840-6541, Email: sales@mightex.com
www.mightex.com or www.mightexsystems.com

Version 6.0, December 2011

Mightex
Simply Brighter

LED SPECTRA (Cont'd)

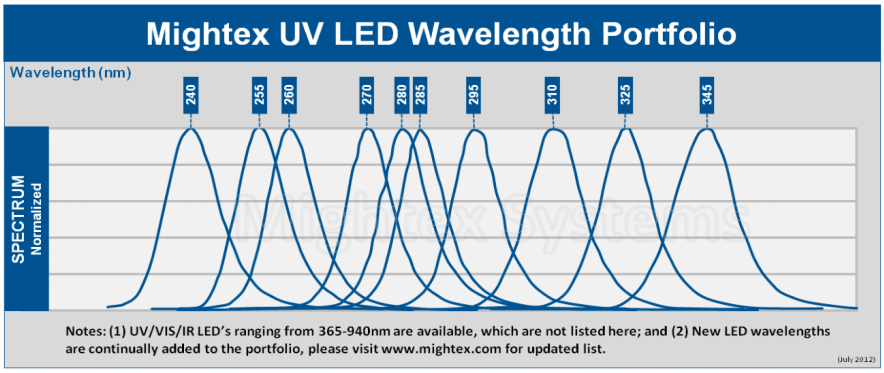

INSTALATION DRAWINGS

1. Installation Drawing for 11-mm LED Collimator, Type-A

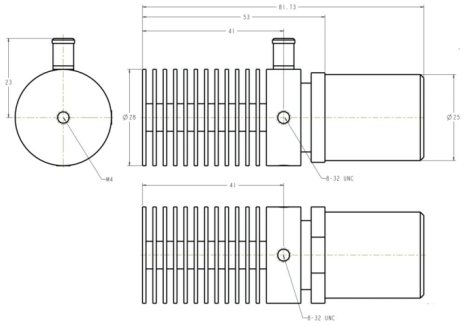

2. Installation Drawing for 22-mm LED Collimator, Type-A

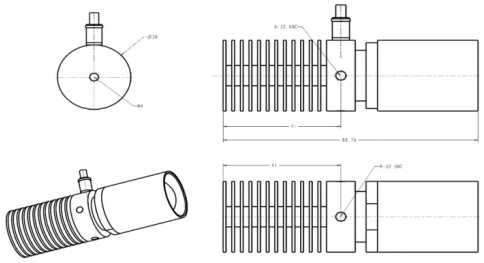

Mightex Systems, 2343 Brimley Road, Suite 868, Toronto, Ontario M1S 3L6, Canada
Tel: 1-416-840-4991 or 1-925-218-1885, Fax: 1-416-840-6541, Email: sales@mightex.com
www.mightex.com or www.mightexsystems.com

Version 6.0, December 2011

Mightex
Simply Brighter

INSTALATION DRAWINGS (Cont'd)

3. Installation Drawing for 38-mm LED Collimator, Type-A

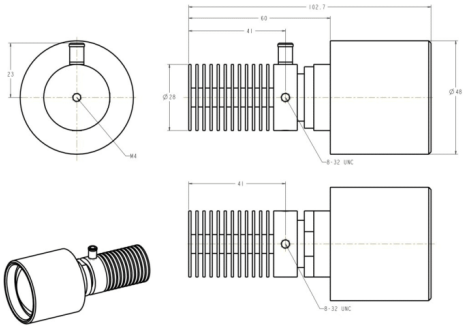

4. Installation Drawing for 48-mm LED Collimator, Type-A

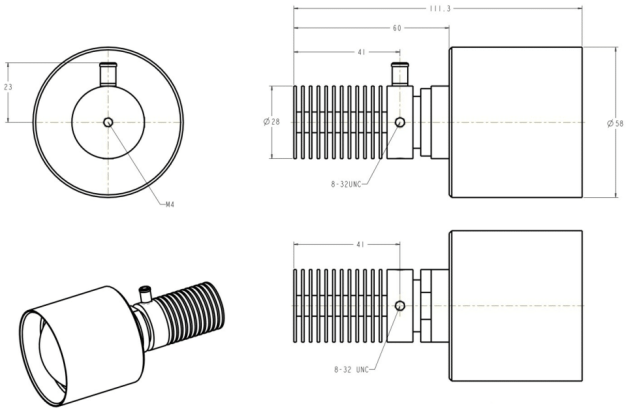

Mightex Systems, 2343 Brimley Road, Suite 868, Toronto, Ontario M1S 3L6, Canada
Tel: 1-416-840-4991 or 1-925-218-1885, Fax: 1-416-840-6541, Email: sales@mightex.com
www.mightex.com or www.mightexsystems.com

Version 6.0, December 2011

Mightex
Simply Brighter

INSTALATION DRAWINGS (Cont'd)

5. Installation Drawing for Type-B LED Collimator

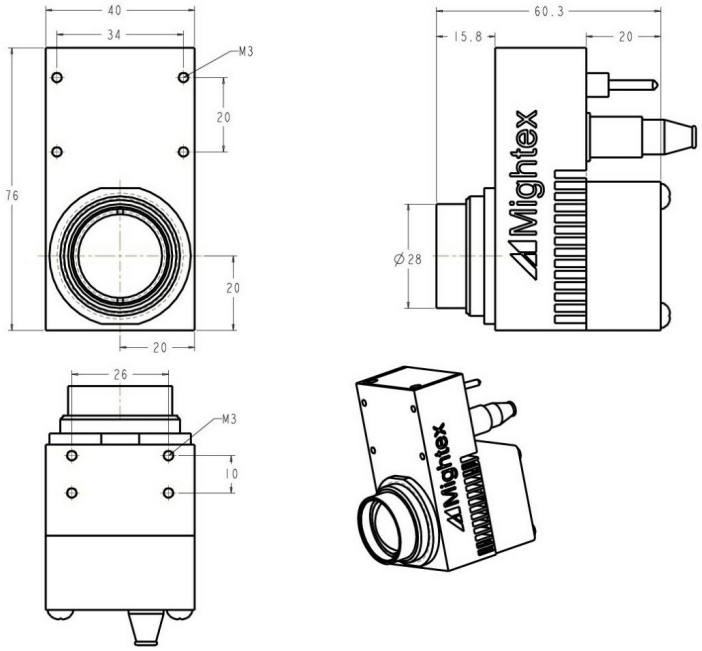

INSTALATION DRAWINGS (Cont'd)

6. Installation Drawing for Type-H LED Collimator

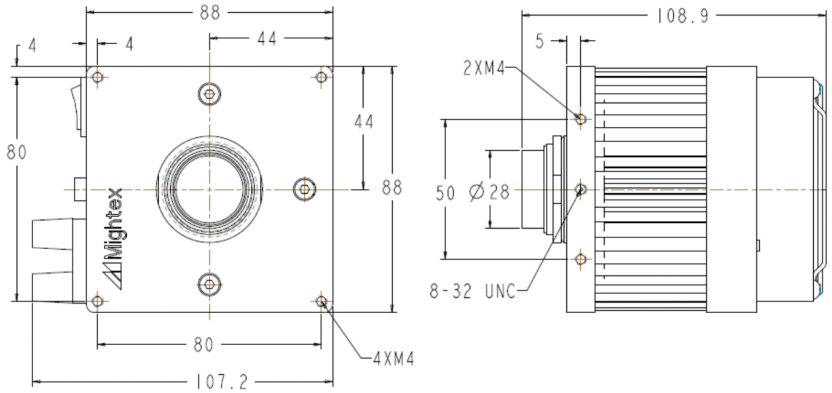

PART NUMBER AND ORDERING INFORMATION

LCS - □□□□ - □□ - □□

Wavelength **Electrical Power** **Clear Aperture**

For example, LCE-0455-03-22 has a wavelength of 455nm, electrical power consumption of 3W, and a clear aperture diameter of 22mm.

With a world-class OEM design team, Mightex offers a broad range of customized solutions in order to meet individual customer's unique requirements. Please call 1-925-218 1885 or email sales@mightex.com for details.